

Electronic Thesis and Dissertation Repository

---

8-19-2021 10:00 AM

## Time-and space-dependent earthquake rupture simulation for Nankai-Tonankai Trough in Japan incorporating multivariate Bernoulli method and stochastic slip models

Yusong Yang, *The University of Western Ontario*

Supervisor: Goda, Katsu, *The University of Western Ontario*

Co-Supervisor: Mora-Stock, Cindy, *The University of Western Ontario*

A thesis submitted in partial fulfillment of the requirements for the Master of Science degree in Geophysics

© Yusong Yang 2021

Follow this and additional works at: <https://ir.lib.uwo.ca/etd>

---

### Recommended Citation

Yang, Yusong, "Time-and space-dependent earthquake rupture simulation for Nankai-Tonankai Trough in Japan incorporating multivariate Bernoulli method and stochastic slip models" (2021). *Electronic Thesis and Dissertation Repository*. 8154.

<https://ir.lib.uwo.ca/etd/8154>

This Dissertation/Thesis is brought to you for free and open access by Scholarship@Western. It has been accepted for inclusion in Electronic Thesis and Dissertation Repository by an authorized administrator of Scholarship@Western. For more information, please contact [wlsadmin@uwo.ca](mailto:wlsadmin@uwo.ca).

## Abstract

In this thesis, a new segmented earthquake occurrence simulation method is developed and is applied to the Nankai-Tonankai megathrust earthquakes, which have historically caused significant damage to the southwestern Honshu, Japan and have a large potential to occur in the next 50 years. For targeting the segmented rupture pattern in Nankai-Tonankai Trough, the simulation method incorporates the multivariate Bernoulli method, which models the rupture pattern by considering both spatial and temporal correlations of individual segments, and the stochastic slip modelling method that produces heterogeneous slip models corresponding to different rupture patterns. Furthermore, possible predominant factors that could affect the earthquake simulation, including the earthquake occurrence catalogues, interarrival time distributions and segmentation pattern, are examined through varying simulation settings. According to its application in seismic hazard assessment, the multivariate-stochastic hybrid method successfully captures the historical seismicity of the Nankai-Tonankai Trough, while emphasizing additional seismic features depending on the predominant factors.

## Keywords

Nankai-Tonankai Trough, segments, earthquake catalogue, Multivariate-Bernoulli model, stochastic slip model, earthquake occurrence simulation, ground motion hazard.

## Summary for Lay Audience

The Nankai-Tonankai megathrust in Japan hosted many large earthquakes with magnitudes greater than 8. Historically, the Nankai-Tonankai megathrust earthquakes have a recurrence interval of 100-150 years. Considering the 75-year elapsed time since the last earthquakes in 1944 and 1946, the Nankai-Tonankai megathrust has an immense potential to host a giant earthquake in the next 50 years. Therefore, the development of credible earthquake occurrence simulation methods is essential for seismic hazard assessment and disaster preparedness.

The rupture pattern of the Nankai-Tonankai Trough varies from individual-segment ruptures to synchronized multiple-segment ruptures. In this thesis, a multivariate Bernoulli modelling method is adopted for earthquake occurrence simulation. The rupture conditions in individual segments are simulated by assuming that the interarrival time follows a probabilistic model, such as Brownian Time Passage distribution, and the multiple-segment rupture scenarios are characterized by the spatial correlation between adjacent segments. Compared with existing probabilistic models, the adopted method captures both spatial and temporal dependency of earthquake ruptures along the segmented fault. Moreover, to generate realistic earthquake slip distributions, the stochastic slip modelling method is combined with the multivariate Bernoulli method. The multivariate-stochastic hybrid method thus can simulate earthquake ruptures by considering their space- and time-interaction, and link the rupture patterns of each simulation with the heterogeneous slip model.

For the Nankai-Tonankai Trough, the integrated model simulates earthquake occurrence with interarrival times and rupture patterns that are consistent with the historical seismicity of the fault segments. Additionally, all simulated rupture histories have realistic earthquake magnitudes, asperity areas, hypocenter locations, and slip values similar to the historical megathrust earthquakes. By applying this new earthquake rupture model to seismic hazard assessment, the anticipated regions with intense ground motions can be identified. The high-risk regions correspond to coastal areas near the middle segments of the Nankai-Tonankai Trough, where the effects due to the synchronized ruptures are more likely. Overall, the hybrid earthquake simulation method provides a consistent framework for carrying out

earthquake occurrence simulation. Its application in seismic hazard assessment also allows carrying the ground motion estimation in a probabilistically time- and space-dependent way.

## Acknowledgments

I would like to express my gratitude for all supports I received from my surroundings. I would like to acknowledge and appreciate my supervisor Dr. Katsu Goda for his constant guidance during my Master's program. The suggestions and helps I received from him guided me from the selection of my research topic till the completion of the thesis. I also would like to thank Dr. Cindy Mora-Stock for being my co-supervisor and giving valuable advice during this program.

I would like to acknowledge Western University for offering the TA position and scholarship. I would also like to thank Dr. Katsu Goda for funding this project in the summer term during these two years.

I would like to thank my fellow graduate students in the research group, Elisa Dong and Karina Martinez, for their advice in complementing my thesis and their suggestions in daily life during this difficult time.

Also, I appreciate the encouragement and emotional support from my family, especially from my parents. Without them, this work would not have been done. I also would like to extend my gratitude to my best friends, Yuntao Zhang, Jingyun Hou, and Yutong Wu, for our long friendship during the last ten years. The fun time with them is always my mental stabilizer during the hard times.

# Table of Contents

Abstract .....	ii
Keywords .....	ii
Summary for Lay Audience .....	iii
Acknowledgments .....	v
Table of Contents .....	vi
List of Tables .....	ix
List of Figures .....	xi
List of Appendices .....	xv
Chapter 1 .....	1
1 Background and research aim .....	1
1.1 Nankai-Tonankai Trough megathrust earthquakes .....	2
1.2 Earthquake occurrence simulation .....	4
1.3 Stochastic slip source model .....	6
1.4 Statement of research aim and objectives .....	8
Chapter 2 .....	12
2 Literature review .....	12
2.1 Nankai-Tonankai Trough: geological setting and historical earthquake occurrence .....	12
2.1.1 Spatial and temporal dependency of the Nankai-Tonankai megathrust earthquake occurrence .....	13
2.1.2 Historical earthquake occurrence catalogues .....	18
2.2 Earthquake occurrence models .....	22
2.2.1 Evolution and classification of earthquake occurrence models .....	22
2.2.2 Multivariate Bernoulli distribution model .....	27
2.3 Stochastic slip source models .....	32

2.3.1	Existing fault source models for the Nankai-Tonankai earthquakes .....	32
2.3.2	Stochastic fault source modelling method .....	37
2.3.3	Stochastic fault source modelling for the Nankai-Tonankai Trough.....	40
Chapter 3	.....	45
3	Nankai-Tonankai Trough earthquake occurrence simulation .....	45
3.1	Earthquake occurrence simulation set-up .....	46
3.2	Bayesian parameter estimation using MCMC .....	50
3.2.1	Input parameter setting .....	50
3.2.2	Parameter estimation results .....	53
3.3	Earthquake occurrence simulation results for Nankai-Tonankai Trough.....	59
3.4	Conclusions of earthquake occurrence simulation results .....	67
Chapter 4	.....	69
4	Stochastic slip model generation.....	69
4.1	Rupture scenarios for 3-segment and 6-segment models .....	70
4.2	Stochastic slip model simulations for Nankai-Tonankai Trough .....	75
4.3	Conclusions of stochastic slip models .....	83
Chapter 5	.....	85
5	Ground motion estimation using multivariate-stochastic hybrid earthquake occurrence modelling method for Nankai-Tonankai Trough .....	85
5.1	Empirical ground motion model in Japan.....	86
5.2	The application of earthquake simulations and stochastic slip models to ground motion estimation.....	90
5.3	Nankai-Tonankai Trough ground motion estimation .....	94
5.4	Conclusions of Nankai-Tonankai Trough ground motion estimation .....	104
Chapter 6	.....	105
6	Conclusions .....	105

6.1 Summary of Nankai-Tonankai Trough earthquake simulation and ground motion estimation using the multivariate-stochastic hybrid method .....	106
6.2 Limitation of multivariate-stochastic earthquake occurrence modelling.....	108
6.3 Future works .....	108
References.....	110
Appendices.....	119
Curriculum Vitae .....	129



## List of Tables

Table 2.1: Summary of probability density functions for four common models for earthquake interarrival time.....	25
Table 2.2: Finite-fault model parameters for the 1944 Tonankai earthquake and 1946 Nankai earthquake. The geometry parameters (i.e. length, width, strike, dip and rake angles) support constraining the shape and orientation of the fault, while the other parameters (Mw or seismic moment) provide an estimation of the energy released during the event. ....	36
Table 2.3: Three commonly used autocorrelation functions in the spatial domain and Fourier domain.....	39
Table 2.4: Estimated total fault area, moment release, moment magnitude, stress drop and average slip for 11 scenarios of the CDMC2012 models .....	44
Table 3.1: Historical earthquake catalogues and corresponding rupture segments for the 3-segment model. ....	49
Table 3.2: Historical earthquake catalogues and corresponding rupture segments for the 6-segment model. ....	50
Table 3.3: Spatial correlations from all segments to the other segment for both 3-segment and 6-segment models. ....	52
Table 3.4: Bayesian estimated parameters for the 3-segment model.....	56
Table 3.5: Bayesian estimated parameters for the 6-segment model.....	57
Table 3.6: Earthquake occurrence simulation results for the 3-segment model and the 6-segment model with $\mu$ , number of simulated occurrences and 50-year rupture probability out of 20,000 simulations using the base catalogues. ....	65
Table 3.7: Earthquake occurrence simulation results for the 3-segment model and the 6-segment model with $\mu$ , number of sample occurrence and 50-year rupture probability out of 20,000 iterations using the 1605 catalogue.....	67

Table 4.1: Summary of estimated moment magnitude and asperity zone depth limit for rupture scenarios within the 3-segment and 6-segment models. .... 74

# List of Figures

Figure 1.1: Division of the Nankai-Tonankai Trough into six segments (Z: Hyuga-nada, A: Tosa-oki, B: Kii-oki, C: Kumano-nada, D: Enshu-nada, E: Tokai) according to the earthquake source zone distribution by Ishibashi (2004). ..... 3

Figure 1.2: Flow chart of earthquake occurrence simulation and ground motion estimation processes from obtaining the earthquake information to the development and validation of the simulation method in different chapters..... 11

Figure 2.1: Occurrence times of historical megathrust earthquakes and corresponding locations of ruptured segments A to E since A.D. 684..... 14

Figure 2.2: Four different fault plane models in the map view: FS71 refers to the geodetic model generated by Fitch and Scholz (1971) and AN75 refers to the seismological model generated by Ando (1975). The models RAN1 and RAN2 (Ando, 1982) are the revised versions of the initial model AN75 and are depicted by a solid blue rectangle and red dash rectangle, respectively..... 16

Figure 2.3: Evidence gathered and summarized by Ishibashi (2004) and Garrett et al. (2016). ..... 21

Figure 2.4: Summary of historical segment rupture patterns for the 13 Nankai-Tonankai megathrust earthquakes since A.D. 684..... 22

Figure 2.5: Hazard functions for four probability distributions of interarrival time between earthquakes with the same standard deviation of 0.5 and mean interarrival time of 1 year... 26

Figure 2.6: Illustration of the earthquake rupture segmentation model with parameters including interarrival time  $\mu$ , earthquake occurrence time  $t$ , distance between segments, and rupture condition indicator  $X$  for the 1096 Enaga earthquake, the 1099 Kowa earthquake, and the 1361 Shoei earthquake. .... 29

Figure 2.7: Flowchart of the Bayesian parameter estimation procedure using Metropolis-Hastings algorithm. .... 32

Figure 2.8: Nankai-Tonankai Trough fault source model geometry for the 1946 and 1944 earthquakes, and the 2012 Central Disaster Managing Center Council (tsunami) source model boundary characterized by yellow lines.....	35
Figure 2.9: Source fault models for the 1854 Nankai earthquake (Aida, 1981), the 1854 Tonankai earthquake in the left figure(Ishibashi, 1981), and the 1701 Hiei earthquake in the right figure (Furumura et al., 2010). .....	36
Figure 2.10: Flowchart of stochastic slip models generation process. ....	41
Figure 2.11: CDMC2012 heterogenous fault slip model of scenario 1 that corresponds to the single asperity region located off Suruga Bay to Kii Peninsula. ....	43
Figure 3.1: 3-segment model consisting of segments A+B, C+D, and E from west to east according to the historical occurrence pattern .....	47
Figure 3.2: 6-segment model consisting of segments Z to E from west to east. All segments from A to E are count as one individual segment unlike the 3-segment model, while the Hyuga-nada segment Z is incorporated as an additional source region in this model.....	47
Figure 3.3: Interarrival time and aperiodicity updating for segment 1 (Nankai segments A and B) of the 3-segment model.....	54
Figure 3.4: Updated spatial correlation between segment 1 and segment 2 (Nankai segments A and B, and segments C and D) of the 3-segment model. ....	55
Figure 3.5: Nankai-Tonankai earthquake occurrence simulation of the 6-segment model results for the first occurrence in the next 50 years using the base catalogue. ....	60
Figure 3.6: Nankai-Tonankai earthquake occurrence simulation of the 6-segment model results for the second occurrence in the next 50 years using the base catalogue.....	63
Figure 4.1: Acceptable area of slip model (shaded region) for the Nankai segment rupture case in the map view. ....	70
Figure 4.2: All six rupture scenarios corresponding to the 3-segment model. ....	72

Figure 4.3: Isodepth contours of 10km, 15km and 20km of the Nankai-Tonankai Trough fault plane from the CDMC2012 model.. .....	73
Figure 4.4: Example of a simulated slip model for the Nankai segment rupture case.. .....	78
Figure 5.1: Comparison between PGV estimated from GMMs of plate-boundary earthquakes before and after taking account of the 2011 Mw9.0 Tohoku earthquake (figure adopted from Morikawa and Fujiwara,2013).. .....	87
Figure 5.2: Flowchart of ground motion simulation using simulated earthquakes with stochastic slip models. ....	91
Figure 5.3: Magnitude-frequency relation of earthquake simulation derived from the 6-segment model using the base catalogue.. .....	93
Figure 5.4: Probability of exceeding different levels of PGVs for occurrence modelling results of the 6-segment model based on the base catalogue with the BPT inter-arrival time distribution. T.....	95
Figure 5.5: Probability of exceeding different level of PGVs with the same color scale for occurrence modelling results of the 6-segment model based on the base catalogue with the BPT interarrival time distribution.....	96
Figure 5.6: Difference in the probability of exceeding different levels of PGV for occurrence modelling results of the 6-segment model based on the base catalogue with the BPT interarrival time distribution to the Weibull distribution.....	98
Figure 5.7: Difference in the probability of exceeding different levels of PGV for occurrence modelling results of the 6-segment model based on the base catalogue with the BPT interarrival time distribution to the exponential distribution.....	99
Figure 5.8: Difference in the probability of exceeding different levels of PGV for occurrence modelling results of the 6-segment model based on the base catalogue with the BPT interarrival time distribution to the 3-segment model with the BPT distribution.....	100

Figure 5.9: Difference in the probability of exceeding different levels of PGV for occurrence modelling results of the 6-segment model based on the base catalogue with the BPT interarrival time distribution to the 3-segment model with the exponential distribution. .... 102

Figure 5.10: Difference in the probability of exceeding different levels of PGV for occurrence modelling results of the 6-segment model based on the base catalogue with the BPT interarrival time distribution to 6-segment model based on the 1605 catalogue with the same distribution..... 103

## List of Appendices

Appendix A: CDMC2012 heterogenous fault slip models.....	119
Appendix B: Average models of 500 stochastic slip models for the 6-segment model. ....	124

# Chapter 1

## 1 Background and research aim

Among natural disasters occurring worldwide, earthquakes cause intense ground shaking and can induce secondary hazards, including fire, tsunami, and landslide. The triggering of an earthquake is primarily caused by a high strain accumulation due to the sliding or colliding tectonic plates (Reid, 1910). Once the strain exceeds the critical limit of the strength of rocks, energy is released along the plate-boundary faults as part of a rupture process, generating seismic waves and possibly inducing secondary hazards. Numerous research has been conducted to estimate economic loss and make decisions for risk mitigation, focusing on the mechanism and periodicity of the earthquake occurrence as well as propagation and intensity of the ground motion. Noticeably, subduction earthquakes at active plate margins occur more frequently than those occurring in intraplate regions due to the relatively faster movement of tectonic plates. The tectonic plate convergence rates vary widely across subduction zones, and a higher occurrence rate of earthquakes is caused at more rapidly converging boundaries (Stein and Wysession, 2003). Megathrust earthquakes are the most significant earthquakes occurring in the convergent plate boundary regions, where a denser tectonic plate is subducting under a less dense continental plate. For instance, the offshore area in Chile has hosted twelve megathrust earthquakes with magnitudes greater than 8 since 1500 and has an average recurrence interval of ~60 years (Ruiz and Madariaga, 2017).

In recent years, megathrust earthquakes in subduction zones have been extensively investigated due to the frequent occurrence rate and the devastating damage in coastal regions (Ammon et al., 2011). This thesis focuses on western to central Japan, where the most recent megathrust earthquakes occurred in 1944 and 1946 at the Tonankai and the Nankai regions, respectively. As recorded by National Oceanic and Atmosphere Administration (NOAA), both earthquakes had a moment magnitude ( $M_w$ ) of 8.2 and caused more than 1000 deaths. Assuming the relatively constant rate of stress accumulation, the Nankai-Tonankai megathrust in Japan typically has a recurrence period of 100-150 years and is expected to rupture in the next 50 years. The next occurrence of



the mainshock of the Nankai-Tonankai megathrust earthquake can be statistically estimated based on historical megathrust earthquake occurrences and their corresponding rupture patterns. Moreover, empirical ground motion models (GMMs) can be employed to calculate expected ground motions throughout Japan. To visualize the potential future shaking hazard estimates, seismic hazard maps and shake maps are useful to detect notable characteristics, such as regions of high exceedance rate. The seismic hazard maps are constructed by setting up a certain threshold of probability or ground motion and mapping the estimated ground motion or probability to the site area, respectively. Comparing with the hazard map, shake maps focus on the intensity of ground shaking throughout the study region. In this thesis, conditional hazard maps are generated to demonstrate the 50-year probability of exceeding different levels of ground motion, which is the commonly used hazard map in Japan (e.g. Fujiwara et al., 2012).

## 1.1 Nankai-Tonankai Trough megathrust earthquakes

The 1707 Hōei earthquake, ruptured approximately the whole Nankai-Tonankai Trough and potentially had a  $M_w$  exceeding 9.0 based on the rupture area (Fujiwara et al., 2019). According to the recurrence time between megathrust earthquakes, Ando (1975) defined a long-interval group and a short-interval group of the Nankai-Tonankai Trough megathrust earthquakes by dividing the entire 600 km-long Nankai-Tonankai Trough region into four major segments A to D, as shown in Figure 1.1. The Tokai segment E, located west of the Suruga Trough, was later introduced by Ishibashi (1981) as an additional segment for explaining the seismic observations of the 1854 Ansei earthquakes. The earthquake recurrence has a longer interarrival time, the time between the last earthquake to the next one, after experiencing the whole-region rupture (i.e. regions from the Nankai segment A to the Tokai segment E). In contrast, the earthquake that ruptured either the western or eastern part of the entire fault has a shorter interarrival time for the next earthquake to occur in the unruptured segments. The seismic activity at segment Z (Hyuga-nada) is recently considered as part of the megathrust rupture region based on geological evidence, such as the sedimentary sand deposit in Kyushu Island (Okamura and Matsuoda, 2012). Thus, the source areas of all thirteen  $M_8$  or greater

interplate earthquakes can be expressed as combinations of different rupture segments, while taking the 1968 Hyuga earthquake as an additional megathrust earthquake with a smaller magnitude of Mw7.9 (Mochizuki and Obana, 2003; Niu et al., 2020).

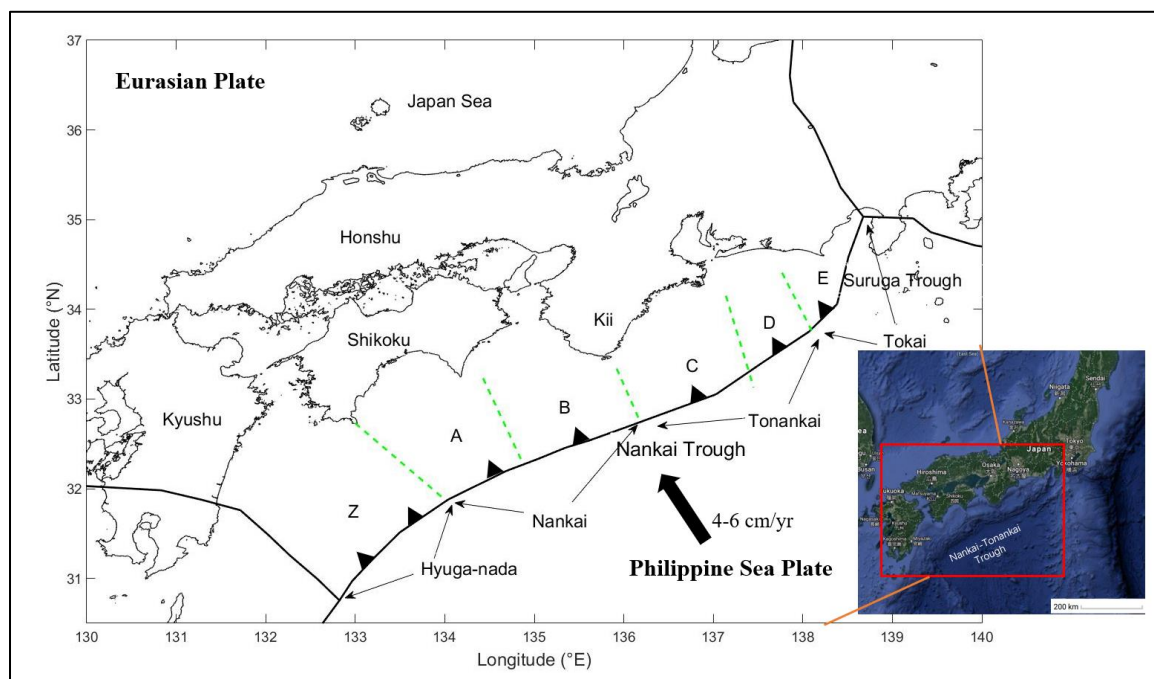


**Figure 1.1:** Division of the Nankai-Tonankai Trough into six segments (Z: Hyuga-nada, A: Tosa-oki, B: Kii-oki, C: Kumano-nada, D: Enshu-nada, E: Tokai) according to the earthquake source zone distribution by Ishibashi (2004). The Philippine Sea plate is subducting beneath the Eurasia plate at Nankai Trough at a rate of 4-6cm/year. The segments A to D are the four segments defined by Ando (1975). The Tokai segment E (Ishibashi, 2004) and the Hyuga segment Z (Furumura, 2014) are added as complementary segments with less seismic activity than the middle segments. The inset map on the right corner is the southwestern Japan, while the red rectangle corresponds to the study area.

Typical rupture patterns of the Nankai-Tonankai megathrust show the tendency that the Nankai segments rupture a short time after the Tonankai segments when the whole-region

rupture does not occur. Furthermore, the Tokai segment tends to rupture with the Tonankai segments, while the Hyuga segment can rupture together with the Nankai segments or individually. The shortest earthquake interarrival time was obtained between the two 1854 Ansei earthquakes, when the second event occurred only 34 hours after the first one. To understand the controlling factors of the rupture pattern, seismic surveys with varying resolution and processing approaches have been carried out in both onshore and offshore areas. For instance, Kodaira et al. (2006) found that small events near the segmentation boundary between the Nankai-Tonankai Trough and the Suruga Trough behave as the trigger of rupture nucleation based on seismic data. As suggested by the numerical simulation of rupture propagation (Kodaira et al., 2006), the strongly coupled patches near the segment boundaries reduce the degrees of coupling when they are affected by the accelerated slow slips. The main segment boundary between B and C is also weakened during the slow-slip events. Therefore, the ruptures can propagate through weakened patches near the borders more efficiently and grow into a giant earthquake across multiple segments. The Nankai-Tonankai Trough thus has the possibility of rupturing in two modes: synchronized rupture and individual segment ruptures. Furthermore, the difficulty in interpretation rises when studying the rupture pattern of individual historical megathrust earthquakes in comparison with the overall rupture tendency. Due to the obscure and potentially false information contained in the historical records of the megathrust earthquakes, the use of earthquake occurrence catalogues involves epistemic uncertainties in terms of occurrence time and ruptured segments, which only can be improved by incorporating new types of supporting evidence (e.g., sedimentary deposit due to induced tsunami, liquefaction effect due to ground shaking).

## 1.2 Earthquake occurrence simulation

Earthquake occurrence modelling has been adopted to improve our understanding of the strain accumulation and release processes in the Earth. There are two main branches of the earthquake occurrence models, i.e. physics-based and statistical models. The physics-based models focus on simulating the physical microscopic-level ruptures using numerical methods, while the statistical models describe the pseudo-periodicity of

earthquake occurrence using probabilistic formulations (Meyers, 2011). For physics-based models, the evolutionary processes from micro fractures to earthquake occurrence are mainly concerned. The idea to link the growth of micro-fractures with the strength of materials was first proposed by Griffith (1924) in his crack propagation experiments. Weibull (1934) then incorporated the heterogeneity in the strength of materials in explaining the underlying cause of variable earthquake rupture under the same condition, which is affected by the distribution of random weakness of the medium. Furthermore, branching models (Kagan and Knopoff, 1987), percolation models (Ben-Zion and Lyakhovskiy, 2002), and cellular automaton (Bak and Tang, 1989; Olami et al., 1992) have been proposed in simulating crack termination and continuation to describe the behaviour of micro-scale rupture propagation. In recent years, additional parameters and physical models related to rheology, rupture branching mechanism, and microphysics are incorporated to predict the time and location of a single earthquake under the rate and state friction law (e.g. Barbot et al., 2012).

Due to the lack of a credible solution for deterministic physics-based methods, statistical models are commonly utilized to provide a probabilistic estimation of earthquake occurrence in particular areas over a specific period. To describe the stochastic behavior of natural events, the statistical models employ the idealized random process to represent the occurrence of an event, while considering the interarrival time between events is probabilistically distributed. Meyers (2011) further categorized the statistical models into two main types; the first model type is only built for large historical earthquakes recorded before development of instrumental catalogues and ignores the clustering of smaller events (aftershocks), while the other model type treats the effect of smaller events as an important role and is developed for use with modern instrumental catalogues. Renewal models mainly focus on predicting the time interval between events in a major fault or seismic zone (Meyers, 2011). In general, the commonly used distribution functions of occurrence time include the exponential, Weibull, lognormal, gamma, and Brownian Passage Time (BTP) models (Matthews et al., 2002). The simplest renewal model assumes that earthquakes follow a Poisson process that considers the probability of rupture is independent of the elapsed time, which is the time since the last rupture occurrence. The hazard rate function of the Poisson process, which describes the

probability of failure of an event at a given time, is also characterized by a constant hazard rate through time. On the other hand, the hazard rate functions for other distributions tend to show an increasing trend through time, characterizing the gradual accumulation of stress due to tectonic force.

As a significant update to the existing models, Ceferino et al. (2020) extended the renewal models by incorporating the spatial dependency of multi-segment earthquake ruptures in the form of spatial correlograms. The primary new feature of the proposed model is that a multivariate Bernoulli model is used to consider both temporal and spatial correlations of individual segment ruptures by adopting renewal models for their temporal recurrence processes. The developed multivariate Bernoulli model was further applied to ground motion estimation for the offshore region of Lima, Peru (Ceferino et al., 2020). Compared with the ground motions calculated from the time-independent Poisson model, the multivariate Bernoulli model generated a hazard map with an additional feature that captures the seismic gap effect, which potentially affects the seismic hazard of a region significantly. Therefore, the multivariate Bernoulli method is considered as an appropriate model for the Nankai-Tonankai megathrust earthquake simulation, noting that the region is composed of at least four segments as inferred from local geological evidence (Garret et al., 2016). As the simulated ruptures are only expressed in terms of ruptured segments, the corresponding earthquake slip models are required to obtain the information regarding the rupture, especially when advanced ground motion and tsunami simulations need to be performed. Moreover, the implementation of multiple types of probabilistic distributions, in addition to the BPT distribution that was introduced in Ceferino et al. (2020), is considered as a potential factor that may improve the earthquake occurrence modelling and simulation when applied to Nankai-Tonankai Trough.

### 1.3 Stochastic slip source model

Fault parameters, such as fault width, length, strike, and dip directions, are essential to determine the location of asperities (the locked area on the fault due to high friction)

within a fault rupture plane. They also provide vital information for deriving annual moment release and moment magnitude through empirical scaling laws (Goda et al., 2016; Thingbaijam et al., 2017). Thus, fault parameters can be employed to check the consistency between the simulated and historical events by estimating and comparing the seismic moment release of simulated earthquakes and historical earthquakes. The dominant sources of fault parameters are the finite fault models derived from the inversion of different types of observational data, such as seismic and geodetic data, for the past major earthquakes. For the Nankai-Tonankai Trough, the earliest fault models were obtained by geodetic and seismic methods proposed by Fitch and Scholz (1971) and Kanamori (1972), respectively. However, Ando (1975) indicated that the parameters may not be accurate because the simulated crustal deformation area derived from the seismic model was much smaller than that occurred during the 1946 Nankai earthquake and the calculated tsunami and seismic waves from the geodetic model were too large when comparing with the observed data.

Early fault plane models tend to assume that the entire segment has homogeneous slip values. On the other hand, spatial heterogeneities of slip distribution within the subducted plate were found to be a more predominant factor than seismogenic segments that control the rupture behaviour (Yamamoto et al., 2013). Moreover, the complicated relationship between the spatial distribution and other fault parameters significantly makes it difficult to generate a unique heterogeneous slip model. In this regard, the inversion of geophysical data can provide independent constraints on the large-scale slips and their spatial variation. However, the rupture velocity was also found to be spatially varying through strong motion studies (Beroza and Spudich, 1988), which adds extra complexity when simulating the rupture process.

To characterize the realistic spatial statistics and asperities of earthquake slip, the stochastic source modelling method can be adopted. As first proposed by Andrews (1980), the slip spectral decay of  $k^{-2}$  in the wavenumber domain leads to the far-field displacement spectral decay of  $\omega^{-2}$ , where  $k$  is the wavenumber and  $\omega$  is the angular frequency. This finding further promoted the development of the K-square model (Herrero and Bernard, 1994), which assumes that the rupture propagates at a constant

velocity and rise time is related to the wavenumber. The K-square model links to the fault length through the corner wavenumber  $K_c$ , where the spectrum of slips decays with  $k^{-2}$  for  $k > K_c$ . Moreover, Mai and Beroza (2002) updated these models using a von Karman auto-correlation function (ACF) to represent the random field slip spatial distribution. The random field generation method can be employed for producing heterogeneous slip distributions in the wavenumber domain. Mai-Beroza model is found to be compatible with the concept of dynamic rupture propagation, which suggests that increasing earthquake magnitude leads to increasing correlation length. Furthermore, the Mai-Beroza model still follows the decaying relation of the power spectrum, while  $K_c$  decreases with the increasing magnitude.

By using the sub-fault division pattern from the future Nankai-Tonankai national tsunami source models developed by the Central Disaster Management Council (2012) and following the stochastic model simulation processes from Goda et al. (2020), the most representative heterogeneous slip models corresponding to possible magnitude scenarios can be generated after a large number of iterations by taking the average of all models. In previous studies, the stochastic slip models and segmented earthquake occurrence models were usually dealt with individually and have not been integrated. When combining the stochastically generated slip models with all possible rupture scenarios, the link between earthquake occurrences simulated from the multivariate Bernoulli method and the heterogeneous slip models corresponding to the earthquake occurrences needs to be established. For Nankai-Tonankai Trough, the evident segmentation allows setting up fundamental rupture scenarios of heterogeneous slip models for each rupture pattern. Thus, the hybrid earthquake occurrence simulation method is considered the most adequate method that accounts for both the segmented rupture pattern and the generation of seismic parameters under realistic constraints.

## 1.4 Statement of research aim and objectives

In this thesis, the main goal is to develop the rupture model that captures both temporal and spatial dependency of the earthquake occurrence for simulating the future Nankai-

Tonankai megathrust earthquakes. As discussed above, the link between different methods needs to be set for building up a statically consistent frame of the simulation. To achieve the desired hybrid rupture model, the individual modelling methods together with suitable input data need to be identified. The most fundamental historical megathrust earthquake information is primarily gathered from literature research. According to the historical occurrence information, the earthquakes are simulated using the multivariate Bernoulli method to characterize the spatial correlation and temporal dependency at the individual segment. Moreover, the rupture scenarios (magnitude range, asperity zone) corresponding to all possible rupture patterns can be set by employing the earthquake source models. Stochastic slip models are then developed under the basis of preassigned scenarios and the random field generation method. In the end, the effectiveness of the hybrid rupture model is tested in ground motion estimation by employing an empirical ground motion model (GMM).

To build a credible earthquake occurrence catalogue, geological, geophysical, and historical evidence of large subduction earthquakes and their corresponding rupture regions are therefore collected from multiple sources of information as earthquake occurrence catalogues, including the information of occurrence time, ruptured region, estimated magnitude and ruptured segments for all historical earthquakes. With the increasing concern in the near-future megathrust earthquake, the rupture scenario becomes an essential factor affecting the location and magnitude of the simulated megathrust earthquake. Besides the baseline segment model and earthquake occurrence catalogue, the hypothesis regarding seismicity of segment Z and the existence of certain earthquakes are accounted for to study the possible effect on earthquake simulation. More importantly, possible segmentation models and occurrence catalogues are combined to evaluate the impact of varying input information on simulating future earthquake occurrence, slip model generation, and ground motion estimation.

The earthquake occurrence simulation is carried out according to the multivariate Bernoulli method that focuses on the synchronized and segmented rupturing scenarios, which corresponds to the historical rupture patterns of the Nankai-Tonankai megathrust. The multivariate Bernoulli model simulates rupture conditions in individual segments by



assuming the interarrival rupture time follows a certain probabilistic distribution, which resembles strain accumulation through time. The stress accumulation process is then composed of stress growing at a constant rate, with additive random stress represented by Brownian motions (Matthews et al., 2002). Besides the commonly used BPT distribution, the Weibull, lognormal, and exponential distributions are employed to investigate the possible effects due to the model choice on the predictions. Furthermore, the multiple-segment rupture scenarios are specified by spatial correlation functions describing the stress interaction between adjacent segments. The developed model captures temporal and spatial interaction between rupture events and adapts to the segmented rupture scenario, thus becoming an advanced earthquake occurrence model for the Nankai-Tonankai Trough. When different earthquake occurrence catalogues are employed for earthquake simulation, the estimated values of parameters, including interarrival time, aperiodicity, and spatial correlation coefficients, vary, and the estimation method of the parameters becomes important due to the interdependence of the parameters. Ceferino et al. (2019) proposed a Bayesian method to update all parameters by using a Monte Carlo Markov Chain (MCMC) algorithm. Compared with the more intuitive maximum likelihood method, the Bayesian method is more effective in that the acceptance and rejection of parameter updates after each iteration are decided based on the acceptance ratio between the prior and proposal distributions of initial and updated parameters during each sampling step of MCMC.

With the simulated earthquake occurrences, the stochastic source models corresponding to assigned rupture areas can be generated using the random field method, while taking the sub-fault division pattern from the optimized source models as the benchmark. When combining the occurrence model with the stochastic source models, statistically consistent earthquake scenarios are captured using empirical scaling laws. Moreover, the stochastic source model provides information regarding the characteristics of earthquake occurrence in the specific region, including hypocenter location, maximum slip, mean slip, and the size of the asperity zone. To link the stochastic slip models with their induced ground motions in a specific study area, the GMMs developed using ground motion records from the 2011 Tohoku, Japan earthquake (Mw 9.0) are utilized to calculate the expected ground motions throughout Japan. Overall, the combination of

stochastic slip modelling and segmented earthquake occurrence modelling method provides a consistent framework for carrying out seismic hazard assessment in a statistically advanced manner.

A brief overall framework is presented in Figure 1.2, which follows the layout of the entire thesis. In Chapter 2, essential information regarding historical earthquakes, local geological setting, and hypothesis are collected and summarized from recent literature. Furthermore, primary information of earthquake occurrence modelling, algorithms of stochastic slip model, and empirical GMMs in the Japan region are explained. The following Chapters 3, 4, and 5, demonstrate the detailed methodology and results corresponding to simulation earthquake occurrence, stochastic slip model generation and ground motion estimation, respectively, as set out in the three objectives of the thesis. Finally, Chapter 6 draws conclusions from the simulation results and discusses the limitations of the current rupture modelling method and possible future improvements.

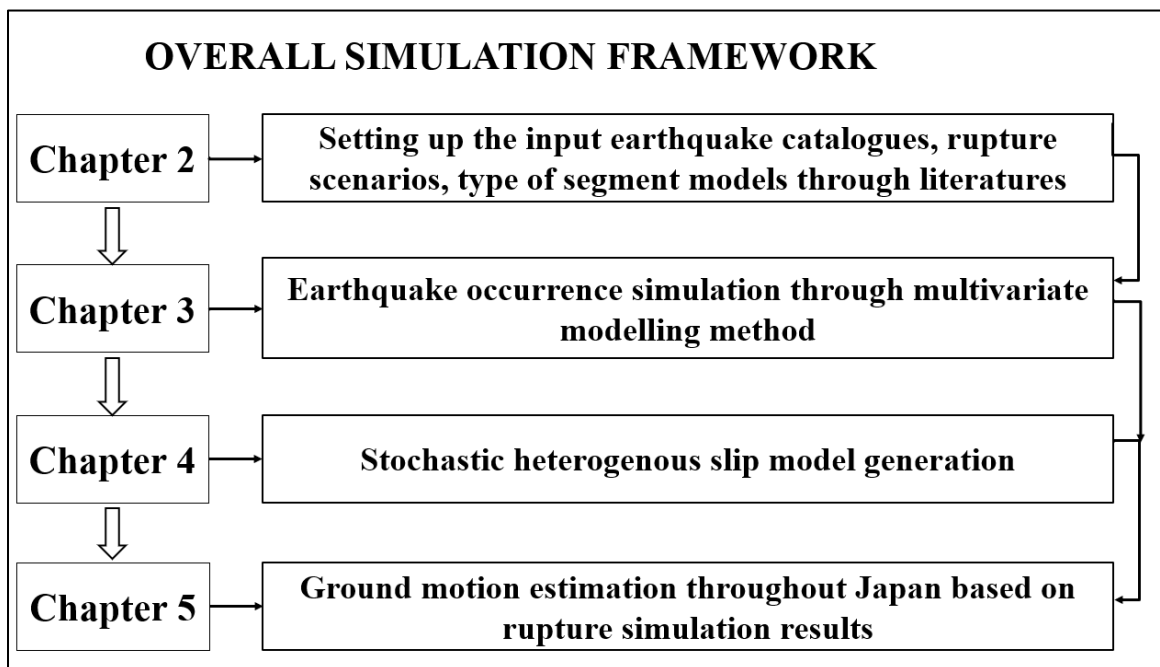


**Figure 1.2:** Flow chart of earthquake occurrence simulation and ground motion estimation processes from obtaining the earthquake information to the development and validation of the simulation method in different chapters.

## Chapter 2

### 2 Literature review

This chapter aims to summarize background information related to the main goal of this thesis, which is the development of the hybrid earthquake occurrence simulation method and its application to the Nankai-Tonankai Trough region of Japan. A detailed literature review is performed by focusing on: 1) historical and geological/geophysical evidence to characterize different earthquake histories of the Nankai-Tonankai megathrust occurrence and their corresponding rupture patterns; 2) earthquake occurrence simulation methods; and 3) stochastic modelling methods and seismological constraints to generate heterogeneous earthquake slip distributions.

#### 2.1 Nankai-Tonankai Trough: geological setting and historical earthquake occurrence

The spatial extent of the Nankai-Tonankai Trough and the temporal dependency between individual earthquake events play the most fundamental role in earthquake occurrence modelling. From the geological evidence of the historical Nankai-Tonankai megathrust earthquakes, both synchronized and segmented rupture patterns are exhibited along the strike direction. Furthermore, the recurrence rate of megathrust earthquakes provides the duration from the start of the stress accumulation stage to the co-seismic rupture stage for individual segments. This section presents evidence from geological, geophysical, and historical aspects and compiles two types of earthquake occurrence catalogues based on the division of rupture segments. By considering different earthquake catalogues, the variations in rupture information can be captured, and the impacts due to the obscure occurrence records in the early history of ruptures and the lack of seismic/tsunami data on the earthquake occurrence simulations can be evaluated.

### 2.1.1 Spatial and temporal dependency of the Nankai-Tonankai megathrust earthquake occurrence

The Nankai-Tonankai megathrust has been intensively investigated due to its high potential for hosting a catastrophic earthquake in the near future. To study the temporal relationship between events that occurred at the two major segments (Nankai and Tonankai segments), Ando (1975) hypothesized that the most recent five large earthquakes with magnitudes greater than 8 in the Nankai-Tonankai Trough were originated from the same source based on the model of crustal deformation, tsunami, and seismic damage in coastal areas. The recurrence rate was also estimated by considering earlier devastating earthquakes recorded in history, as listed in Figure 2.1. The historical catalogue included 12 events in total and traced back to A.D. 684. It was demonstrated that all events followed either a twin-shock or entire-region rupture pattern. The twin-shock pattern typically involves ruptures of the eastern segments C+D, followed by ruptures of the western segments A+B. On the other hand, the whole rupture pattern involves the simultaneous ruptures of all segments A to D. Based on these observations, Mitsui and Hirahara (2004) concluded that the average dislocation of tectonic motion and interval of the seismic cycle to be 6 m on the fault plane and 180 years, respectively, and also inferred that a potential future event with a magnitude greater than 8 could occur in the Tokai segment E. Based on the historical records, Ishibashi (2004) concluded a similar recurrence interval of 176 years, while summarizing the ruptured segments for all 12 Nankai-Tonankai megathrust earthquakes shown in Figure 2.1. However, it was also noticed that the existing documents contain some ambiguous records with possible errors and fictional earthquakes (Ishibashi, 2004). These unconfirmed rupture segments for the ancient events have been marked by red rectangles in Figure 2.1. To better constrain the occurrence time and the rupture patterns, more recently discovered historical and geological evidence is collected to define the segment boundaries and to estimate the historically ruptured segments for each megathrust earthquake. This is presented later in this section.

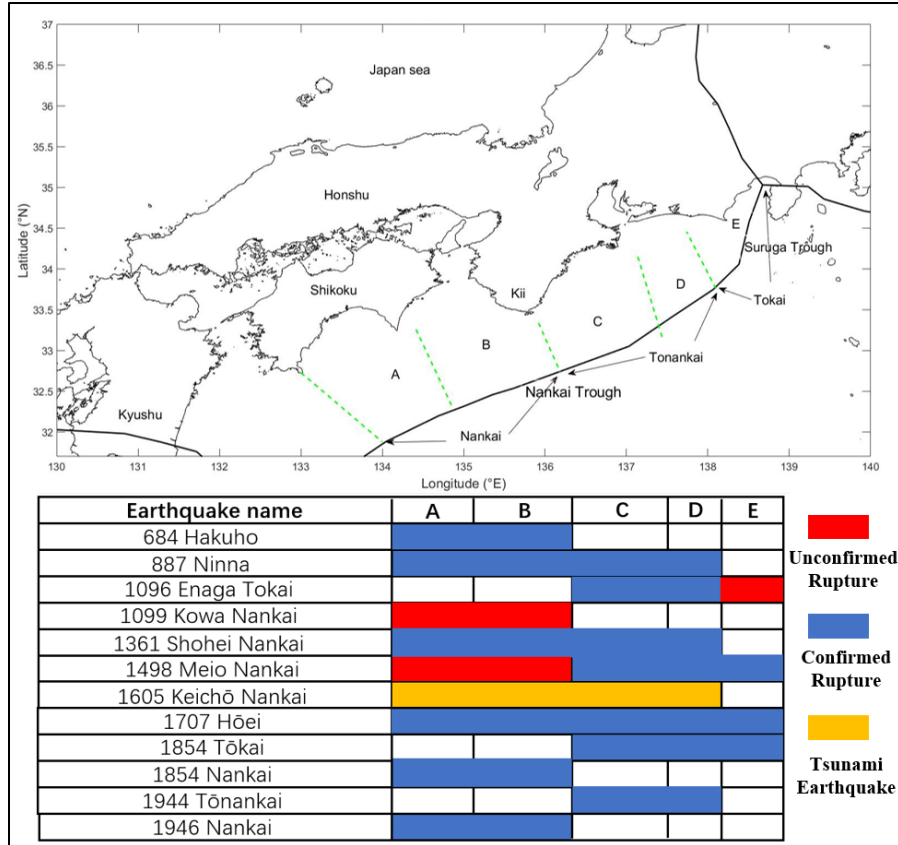


**Figure 2.1:** Occurrence times of historical megathrust earthquakes and corresponding locations of ruptured segments A to E since A.D. 684. The blue colour represents the ruptured segments has clear supporting historical evidence, while the red colour indicates that segments may have experienced rupture during the megathrust earthquakes. The 1605 Keicho earthquake, marked by yellow, is a special tsunamigenic earthquake that produced much larger tsunamis than that expected from its magnitude.

The generation of the Nankai-Tonankai Trough fault models started in the 1970s. Fitch and Scholz (1971) and Karamori (1972) estimated the fault geometry parameters for the 1944 and 1946 twin events based on geodetic and seismological data, respectively. To understand the mechanism of the Nankai-Tonankai megathrust rupture, Ando (1975) compared the theoretical crustal deformation and tsunami waves along the coast based on both fault models with the observed data. For Kanamori's seismological fault model, the simulated crustal deformation only occurred in areas near the southern Kii Peninsula.

However, the observed crustal deformation was found to extend to Shikoku Island and Kii Peninsula. Thus, the actual seismic moment release was much larger than that estimated from the seismological model. In contrast, Scholz's geodetic model generated much larger seismic and tsunami waves, which were not in agreement with the observations. Both pioneer models were relatively simplistic and showed less agreement with the observations.

In addition to the 1944 and 1946 earthquakes, Ando (1975) carried out further analyses on the 1854 Ansei I and II earthquakes, where the second rupture occurred one day after the first. Both earthquakes had an estimated magnitude of 8.4 based on the records on the Historical Encyclopedia of Great Edo. The geodetic similarity between the 1854 Ansei I earthquake and the 1944 earthquake, such as the upheaval and subsidence of specific areas, indicated that both earthquakes were originated from the same source, i.e. segment C. However, segment D was added to explain the subsidence and upheaval observed east to segment C during the 1854 Ansei I earthquake. For the Nankai earthquakes, the seismic intensity was much higher in the 1854 Ansei II earthquake by comparing its tsunami wave and seismic intensity with the 1946 Nankai earthquake, although both earthquakes had a similar extent of deformation. The much higher number of aftershocks following the 1854 Ansei II earthquake further confirmed this finding. Based on this observation, the Nankai segment was hypothesized to experience a more sudden rupture during the 1854 Ansei II earthquake than the rupture generated in segment A during the 1946 earthquake. Moreover, the eastern Nankai segment B was considered more brittle compared with the western Nankai segment A. The earliest 1707 Hoi earthquake was one of the most significant earthquake events in Japanese history and was well explained by the simultaneous whole rupture of the Nankai-Tonankai Trough. Considering the mismatches caused by using the seismological and geodetic fault models with the observations, Ando (1982) eventually proposed a new fault model by matching the simulated tsunami waves with historical tide-gauge records in Uwajima, Shimotsu, and Hososhima for the 1946 Nankai earthquake. As indicated in Figure 2.2, all four source models of the 1946 Nankai earthquake assume that the fault plane has homogeneous slip values. Although the fault geometry and detailed fault parameters proposed in recent studies are more accurate (e.g. Baba et al., 2002; Kikuchi et al., 2003), the area of the

fault plane and the supporting evidence of segmentation are informative for constraining the fault geometry of the Nankai segments. These models reveal the primary geological setting of the fault plane in the early research.

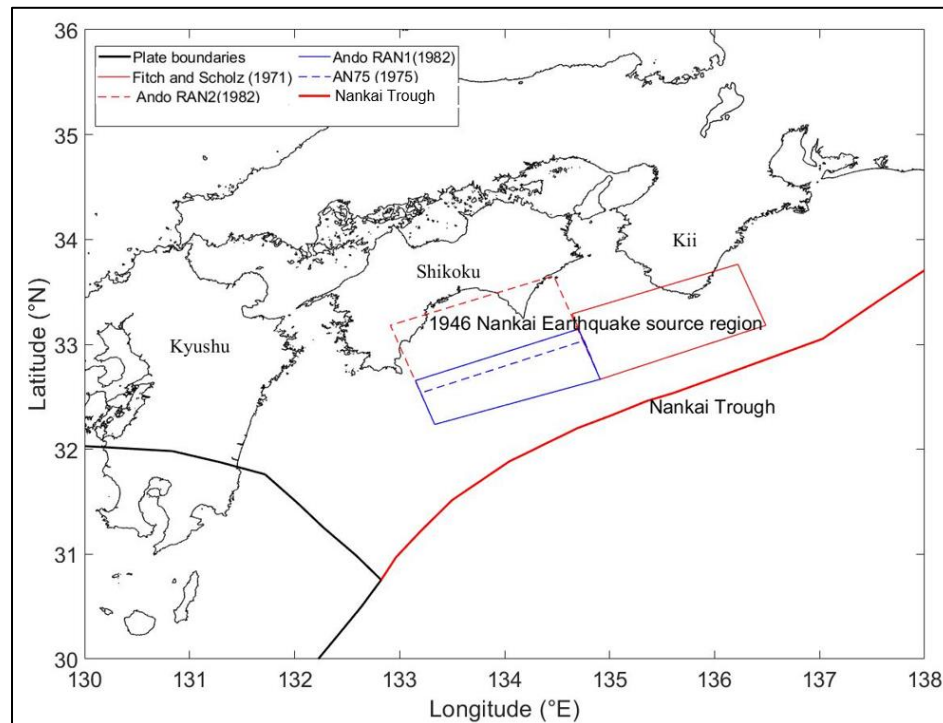


**Figure 2.2:** Four different fault plane models in the map view: FS71 refers to the geodetic model generated by Fitch and Scholz (1971) and AN75 refers to the seismological model generated by Ando (1975). The models RAN1 and RAN2 (Ando, 1982) are the revised versions of the initial model AN75 and are depicted by a solid blue rectangle and red dash rectangle, respectively.

To gain further understanding of the physical properties related to the Nankai-Tonankai Trough, the geological and geophysical properties in both onshore and offshore areas were surveyed. An important finding was that the accretionary prism consisted of marine sediments formed during the subduction of the underlying oceanic plate. The full-waveform tomography carried out by Operto et al. (2006) provided a high-resolution

image of the crustal structure for the eastern Nankai-Tonankai Trough. The upper accretionary prism and lower backstop layer were both under high compressional stress, which points to an active frontal thrust in shallow regions even during interseismic intervals. Hirshorn and Weinstein (2009) noted that the rupture speed slows down when the rupture front passes through the accretionary prism due to the weaker material strength and smaller shear rigidity. In the Nankai-Tonankai Trough, the less rigid crust also produces more devastating tsunamis because slip values in the accretionary prism tend to be greater for earthquakes with the same magnitude when the shear rigidity is lower than other locations. Furthermore, Davis et al. (2006) obtained oceanic borehole hydrologic drilling data at two sites located on the Philippine Sea Plate and seaward part of the Nankai-Tonankai accretionary prism off southwestern Japan. An aseismic slip dislocation event was discovered close to the up-dip limit of the locked portion of the subduction zone for releasing the local stress through slow seaward slip propagation to the toe of the accretionary prism. This phenomenon was considered as a process for subduction thrust to release stress and load neighbouring areas during the interseismic period and possibly affecting the length of the stress build period before reaching the critical limit.

Nanjo and Yoshida (2018) presented a  $b$ -value map, representing the relative frequency between small earthquakes and large ones along the whole Nankai-Tonankai Trough. The  $b$ -value was found to be inversely correlated with the slip-deficit rate, which characterizes the strongly locked patches at the interface between plates, and inversely dependent on differential stresses. With this observation, the Tonankai segment with a higher slip-deficit rate leads to a lower  $b$ -value representing fewer small events in comparison with the Nankai segment. This may explain why the Tonankai segment tends to rupture first in historical records due to its higher differential stresses. A similar phenomenon was demonstrated by Kimura et al. (2019), who investigated interplate coupling distribution using onshore Global Navigation Satellite Systems (GNSS) and offshore GNSS/A observation data. Besides, a strong coupling ratio was found in a shallow region of sea floor less than 20 km in depth, which coincides with the depth of the accretionary prism. This result suggests that the shallow plate interfaces have the potential for inducing tsunamigenic earthquakes, which occurred in 1605 with a surface



wave magnitude of 7.9 as suggested by the National Center for Environmental Information (NOAA). With the understanding of the factors controlling the seismicity of the Nankai-Tonankai Trough, the variation in historical rupture pattern and fault geometry, such as the asperity zone depth limit, can provide primary constraints and thus have been intensively studied as the important components of earthquake simulation.

### 2.1.2 Historical earthquake occurrence catalogues

The Nankai-Tonankai Trough fault plane geometry is well constrained by seismic surveys, such as wide-angle seismic surveys (Kodaira, 2000), seismic tomography surveys (Liu et al., 2014), and seismic reflection surveys (Park et al., 2010). Moreover, the fault plane geometry can be explained by other types of geophysical observations. For instance, Mochizuki and Obana (2003) conducted measurements using ocean-bottom seismometers in both western and eastern fault segments of the Nankai-Tonankai Trough. Their observations confirmed that the western up-dip limit of the seismogenic zone coincides well with the up-dip limit of the 1946 Nankai earthquake fault plane and is at the estimated 150°C isotherm of the interplate interface. However, the rupture condition of prehistoric megathrust earthquakes is still poorly understood compared with the fault geometry. Unlike the five most recent megathrust earthquakes, earlier megathrust earthquakes that occurred between A.D. 684 and A.D. 1605 cannot be associated with direct geophysical data as presented above for the five recent earthquakes. Therefore, records in historical documents and geological evidence play an important role in defining the area of rupture as well as the approximate magnitude for individual events. In this regard, Ishibashi (2004) conducted a systematic review of the historical documents, for instance, *Nihon Shoki* and *Meigetsuki*, which cover the occurrence and induced damage of historical Japanese earthquakes since A.D. 684. For these prehistoric earthquakes, the rupture area and seismic intensity were inferred from descriptions of physical damage and accounts, co-seismic uplift/subsidence, and other effects on human settlements.

Recently, Garrett et al. (2016) conducted a comprehensive review of seismic and tsunami events that occurred in the Nankai-Tonankai Trough by collecting geological evidence, including 1) erosion and deposition at coastal sites by tsunamis, 2) liquefaction and turbidite deposits by ground shaking, and 3) biotic, facies, and geomorphic changes in coastal or onshore fault areas by deformation. Subsequently, 72 sites exhibiting different types of evidence were investigated within the whole Nankai-Tonankai Trough region. By employing the radiocarbon dating technique on tsunami deposits within positions of wash-over through the beach ridge, the layers were correlated with the paleoseismic earthquakes (Garrett et al., 2016). As pointed out by Okamura and Matsuoka (2012), more recent evidence can be removed by anthropogenic activities, leading to missing records for rupture evidence in certain areas. Other types of geological evidence were therefore gathered to complement the existing evidence. Besides tsunami deposits, liquefaction traces and turbidites deposits were interpreted as the characterization of intense shaking, which can be related to devastating megathrust earthquakes (Sangawa, 2001). On the contrary, the ground motion evidence also distinguished the tsunamigenic earthquake (for instance, the 1605 Keicho Nankai earthquake) from the earthquakes with strong shaking (Ishibashi, 2004). The biotic activity and change of facies, such as clusters of encrusting organisms, can be affected by the crustal uplift and subsidence, therefore, being used as deformation indicators. As an efficient method of defining segment boundary, biotic evidence is extensively examined at sites where the exact boundary locations between segments are determined (Shishikura et al., 2008; Iryu et al., 2009).

Different types of evidence are summarized in Figure 2.3 for the rupture history of each segment, as presented by Garrett et al. (2016), although detailed reviews of different evidence at each site are out of the scope of this thesis. In light of all kinds of gathered evidence, the historical rupture pattern of megathrust earthquakes can be identified. Furthermore, Figure 2.4 illustrates the segment rupture patterns for all 13 megathrust earthquakes (including the 1968 Hyuga-nada earthquake) based on the evidence presented in Figure 2.3 and will be used later as the input when simulating the earthquake occurrence using the multivariate Bernoulli method in Chapter 3.

The rupture pattern of historical megathrust earthquakes cannot be uniquely constrained by accommodating the current evidence since the rupture patterns and interpretations of the events are still arguable. For instance, the rupture possibility of the segment Z during the occurrence of historical earthquakes has been proposed by Furumura et al. (2011), but sufficient geological evidence to support the correlation to tsunami traces and seismic deformation generated from historical megathrust earthquakes is still lacking (Garrett et al., 2016). Besides, the actual occurrence of the 1099 Kowa earthquake has also been debated by Ishibashi (2016), and the 1096 Enaga earthquake potentially involved a whole-region rupture. Moreover, the 1605 tsunami earthquake is commonly accepted as a whole-region rupture event but only ruptured in a region shallower than the depth of 15 km. This particular event has a surface wave magnitude of around 7.9 and the largest slippage took place in the Nankai segment. Therefore, another catalogue by considering the 1605 earthquake as a Nankai rupture event may be considered to investigate the effect of variation in input rupture patterns on earthquake occurrence simulation.

To incorporate different possibilities in the earthquake occurrence, six historical earthquake catalogues with different scenarios are prepared when carrying out the earthquake occurrence simulation in Chapter 3. The earthquake magnitudes are obtained from different seismic recording agencies, such as Global Historical Earthquake Catalogue (GHEC) and Japan Meteorological Agency (JMA), while the rupture lengths of prehistorical earthquakes are primarily estimated from the rupture segments and the ruptured lengths from finite-fault models of more recent earthquakes. The magnitude, ruptured segments, and rupture length are summarized in Figure 2.4 for each megathrust earthquake to set the earthquake occurrence catalogue following a 6-segment scenario based on the evidence illustrated in Figure 2.3. More earthquake catalogues, based on different considerations of uncertainties associated with historical records and division of segments, are presented and discussed in Chapter 3.

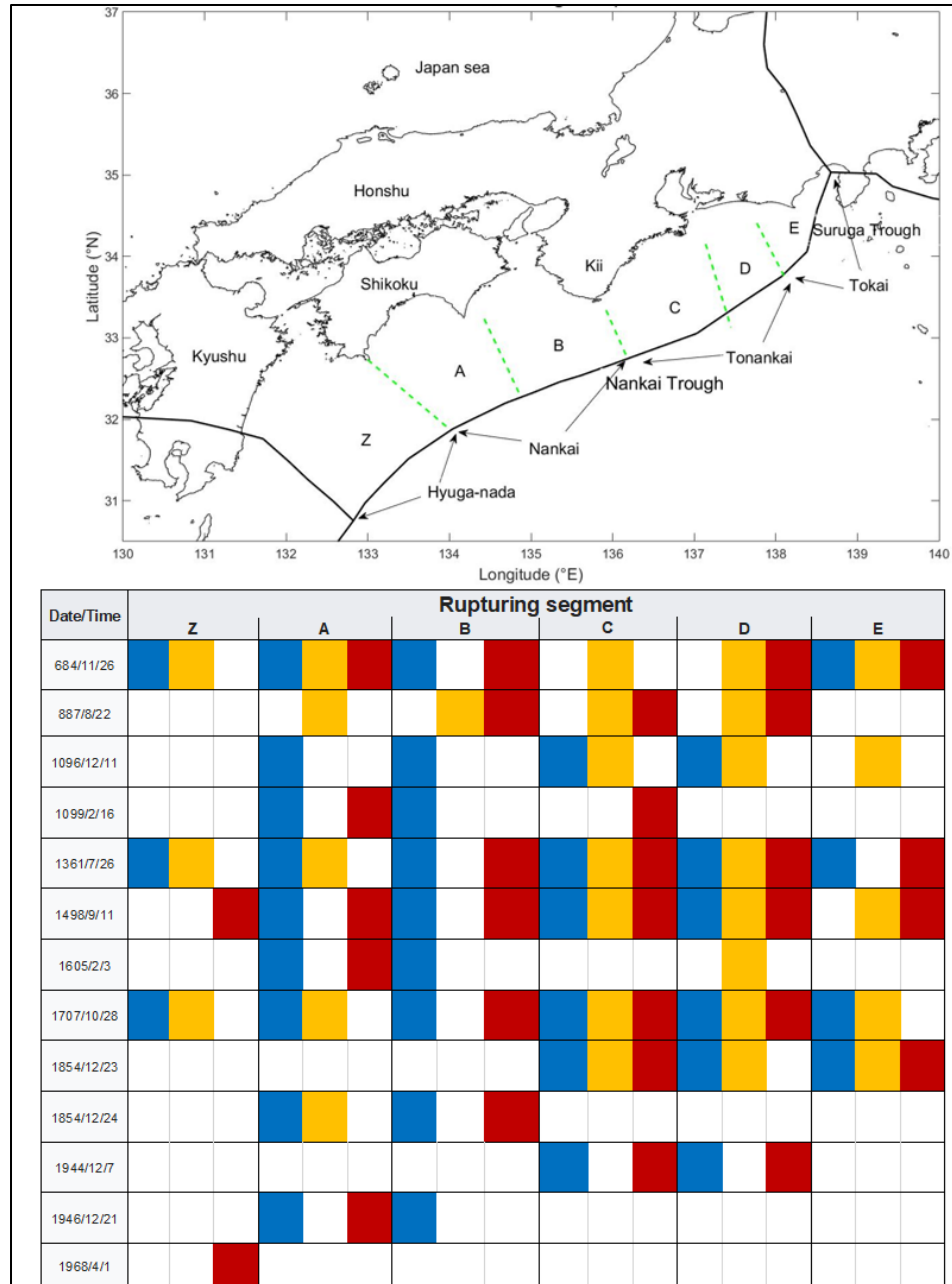


**Figure 2.3:** Evidence gathered and summarized by Ishibashi (2004) and Garrett et al. (2016). The blue colour represents the historical evidence (e.g. Nihonshoki), while the red and yellow colours indicate the seismic/geodetic and tsunami evidence of ruptured segments, respectively.

Date/Time	Rupturing segment						Magnitude	Corresponding rupture length
	Z	A	B	C	D	E		
684-11/26							Ms 8.4/ Mw 8-9	630 km
887-8/22							Ms 8.6/ Mw 8-9	490 km
1096-12/11							Ms 8.4	210 km
1099-2/16							Ms 8.4	280 km
1361-7/26							Ms 8.4/ Mw 8-9	630 km
1498-9/11							Ms 8.3-8.6	630 km
1605-2/3							Ms 7.9	490 km
1707-10/28							Ms 8.4/ ML 8.6/ Mw 8.7-9.3	630 km
1854-12/23							Ms 8.3/ ML 8.4	350 km
1854-12/24							Ms 8.4/ ML 8.4	280 km
1944-12/7							Mw 8.0-8.2	140 km
1946-12/11							Mw 8.2-8.4	260-320 km
1968-4/1							Mw 7.5	110 km

**Figure 2.4:** Summary of historical segment rupture patterns for the 13 Nankai-Tonankai megathrust earthquakes since A.D. 684. Earthquake information composed of magnitude (NOAA; Tsunami digital library; JMA) and estimated ruptured length for prehistorical earthquakes and obtained rupture length from fault source models for recent earthquakes. (Ms: surface-wave magnitude; ML: local magnitude; Mw: moment magnitude)

## 2.2 Earthquake occurrence models

### 2.2.1 Evolution and classification of earthquake occurrence models

Since the early elastic rebound model of Reid (1910), earthquake occurrence modelling methods have evolved with the advent of a more reliable earthquake database and an improved understanding of earthquake rupture processes. In recent years, both physics-based and statistical earthquake occurrence modelling methods have been progressively developed to provide better estimates of the possibility of a future earthquake. As

described by Meyers (2011), the main difference between deterministic (physics-based) modelling and stochastic (statistical) modelling is that the former method tries to fully describe and predict the underlying process, while the latter approach treats some unpredictable processes as random variables and focuses on the pseudo-periodicity of earthquake occurrence. Currently, the deterministic method has not been fully developed to generate credible predictions, thus the statistical approach is more commonly used in assessing the probability of earthquake occurrence at certain locations and times (Console et al., 2017).

The type of statistical occurrence models varies depending on their formulated approaches and input parameters. Among statistical renewal models, a time-independent Poisson model assumes that earthquake occurrence can be represented by a stochastic process with a constant occurrence rate (Console et al., 2017), and the interarrival time between events is exponentially distributed. Under this assumption, the empirical laws of seismology, such as the Gutenberg-Richter law (Gutenberg and Richter, 1956), link the occurrence frequency of events with the size of events or earthquake magnitude, and can be used to describe the observed distribution of earthquakes. However, the constant occurrence rate of the Poisson process is inconsistent with the elastic rebound theory (Reid, 1910), as it ignores the accumulation of stress during cyclic periods. More realistic renewal models are usually employed by considering different probabilistic distributions for earthquake interarrival times and capturing the sudden drop of rupture probability after an earthquake. The commonly used statistical distributions of probabilities include the Gaussian distribution (Rikitake, 1974), lognormal distribution (Nishenko and Buland, 1987), Weibull distribution (Hagiwara, 1974), and Brownian Passage Time (BPT) distribution (Kagan and Knopoff, 1987).

The renewal models mainly focus on estimating the long-term average hazards and the interval time to the next event (Console et al., 2017). In this thesis, the occurrence of main megathrust earthquakes is focused upon by neglecting the occurrence of aftershocks. For a duration of an observation period  $(0, T)$ , the time from the start of the period to the first event is considered as  $X_0$ . As the occurrence before A.D. 684 is not available, the simulation is defined to start from A.D. 650, when a stable

political/governing system started and allows the record to be maintained. Therefore, 34 years is the value of  $X_0$  and  $P(X_0)$  is the rupture probability. Subsequently, the interarrival time between the occurrences of the following  $n$  events are recorded as  $X_1$  to  $X_n$ . The final time period is recorded as  $X_{n+1}$ , which represents the time from the occurrence of last event to the end of the period, year 2020. The overall likelihood can be expressed as (Meyers, 2011):

$$P(X_0, X_1, X_2 \dots X_n, X_{n+1}) = A(X_0) [\prod_{i=1}^n P(X_i)] B(X_{n+1}) \quad (2.1),$$

where  $A(X) = \frac{[1-F(X)]}{\mu}$  and  $B(X) = [1 - F(X)]$ ,  $F(X)$  is the cumulative probability distribution function of the interarrival time,  $\mu$  denotes the expected value of the randomly distributed interarrival time, and  $B(X)$  is the exceedance function. For any statistical earthquake occurrence model, the hazard function representing the conditional failure rate of an event in the near future ( $t_e, t_e+\tau$ ) can be expressed as:

$$f(\tau|t_e) = p(t_e + \tau) / [1 - F(t_e)] \quad (2.2),$$

where  $t_e$  is the elapsed time from the present to the previous rupture, and  $\tau$  represents the time from the present to the next event.  $p(x)$  is the probability density function of the interarrival time. As time progresses, the probability of earthquake occurrence increases as strain accumulates, except for the Poisson process. Once the accumulated strain is released in an earthquake, the probability drops dramatically, and the recurrence process returns to the starting point.

In probability theory, the exponential distribution models the occurrence of an event as a continuous and independent process with a constant average rate. Unlike the independent distribution, the Weibull distribution is flexible and models the probability density function according to two parameters:  $k$  and  $\lambda$ , where  $k$  is the shape parameter, which indicates the condition of failure rate to be decreasing, constant or increasing through time.  $\lambda$  is the scale parameter and always greater than 0 and so as to  $k$ . Likewise, the other time-dependent distributions, such as BPT distribution and lognormal distribution, are estimated according to the mean  $\mu$  and standard deviation  $\sigma$  or the coefficient of variation  $\alpha$  of the random variables.

Furthermore, by employing the BPT distribution function (Matthews et al., 2002), the ruptures of the individual segment can be viewed as the Brownian Relaxation Oscillator (BRO) occurring on every section of the fault. The stress accumulation process is then composed of stress growing at a constant rate, with additive random stress induced by Brownian motions. Once the accumulated stress reaches the critical limit, the BRO returns to the initial stress condition. As a result, the BPT distribution is considered a statistical representation of the physical rupture process (Ceferino et al., 2020). For comparison, Table 2.1 summarizes probability density functions for the four commonly used interarrival time distribution functions.

**Table 2.1:** Summary of probability density functions for four common models for earthquake interarrival time

Distribution	Probability density functions
Brownian Passage Time	$f(x, \mu, \alpha) = \left(\frac{\mu}{2\pi\alpha^2 x^3}\right)^{1/2} e^{-\frac{(x-\mu)^2}{2\alpha^2 \mu x}}$
Weibull	$f(x, k, \lambda) = \left(\frac{k}{\lambda}\right) \left(\frac{x}{\lambda}\right)^{k-1} \left(e^{-\left(\frac{x}{\lambda}\right)^k}\right)$
Exponential	$f(x, \lambda) = \lambda e^{-\lambda x}$
Lognormal	$f(x, \mu, \sigma) = \frac{1}{x\sigma\sqrt{2\pi}} e^{-\frac{1}{2} \frac{(\ln x - \mu)^2}{\sigma^2}}$

For visualizing the behaviour of hazard rate of different occurrence models through time, hazard functions of the four distributions mentioned above are plotted in Figure 2.5. All distributions are assumed to have a mean interarrival time of 1 year, except for the exponential distribution, which only has one adjustable parameter. The standard deviation of 0.3 is usually used in Japan, while global studies tend to estimate a value between 0.3



and 0.7. In this illustration, the standard deviation of 0.5 (as a middle value of global studies) is used for demonstration. From the plot, both BPT and lognormal hazard functions have a much lower rate of failure at the start compared with the other two. The Weibull hazard function shows the rapid increase of the hazard rate from time 0, which is unusual in the realistic situation (Matthews et al., 2002). Unlike the time-dependent distributions, the exponential hazard function is constant through time, representing the memory-less property of the Poisson process. Thus, the temporal dependency between historical earthquakes, as described by the hazard functions, is expected to vary between different distributions and affect the earthquake occurrence simulation.

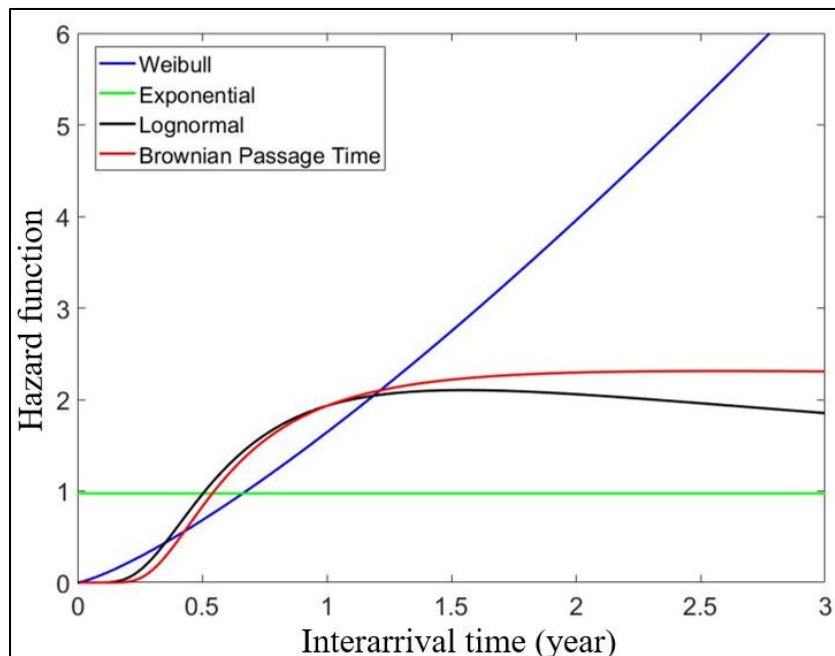


**Figure 2.5:** Hazard functions for four probability distributions of interarrival time between earthquakes with the same standard deviation of 0.5 and mean interarrival time of 1 year. Time-dependent probabilistic distributions, including BPT, lognormal and Weibull distribution, are showing an overall increasing hazard rate as time advances. The exponential distribution, which neglects the effect of elapsed time, indicates a constant hazard rate through time.

## 2.2.2 Multivariate Bernoulli distribution model

As an advanced model considering both spatial and temporal dependency of earthquakes, Ceferino et al. (2020) proposed a multivariate Bernoulli model for characterizing the elastic-rebound behaviour in the segmented tectonic fault. In this model, the interarrival time of each segment is evaluated based on a specific probabilistic distribution as in renewal models, while the spatial correlation of the ruptures is characterized by a correlogram function, which is specified by the spatial-decay parameter  $\gamma$ . As mathematically proved by Ceferino et al. (2020), the simulated interarrival time is capable of preserving the initially assumed distribution after incorporating the spatial correlation. For demonstrating the validity and the consistency of this model, Ceferino et al. (2020) applied the multivariate Bernoulli model to simulate the earthquake occurrence in the central subduction zone in Peru, where the offshore fault region was segmented along the strike direction. The spatial decaying parameter  $\gamma$  was successfully obtained by fitting the simulated annual moment release with the historical values by trial and error, and the consistency of the rupture interarrival time distributions was demonstrated. Importantly, the multivariate Bernoulli model for the multi-segmented rupture region significantly improved the characteristic seismic features in earthquake occurrence simulation of the historical events. The result captured all essential features predicted by the time-independent model, which is a standard model in carrying out probabilistic seismic hazard analysis. Furthermore, the seismic-gap effects were also captured in the multivariate Bernoulli model. The seismic gap hypothesis suggests that an earthquake hazard increases with time since the last large earthquake on certain faults or plate boundaries.

To start the multivariate Bernoulli earthquake occurrence modelling, a tectonic fault region is first discretized into  $N$  segments: for each segment  $X_i(j)$ , the rupture condition indicator, takes a value of 1 or 0 depending on whether an earthquake rupture occurs at the time of year  $t$  in the segment  $j$ . Discretization of the fault should reflect the geological setting of the region. In this thesis, the method focuses on the segmentation in the strike direction. The model assumes that the occurrence of ruptures depends on the elapsed time  $T_t$ , which contains the time for each segment since the last time of rupture. For the

segmented model, each segment  $j$  has its interarrival time distribution defined by two parameters: the mean interarrival time  $\mu_j$  and the coefficient of variation  $\alpha_j$  (or aperiodicity) of the corresponding segment. For demonstration, Figure 2.6 shows earthquake rupture conditions from the 1096 Enaga earthquake, the 1099 Kowa earthquake, and the 1361 Shoei earthquake, as reported in Figure 2.4. This figure illustrates the concept and basic parameters of the segmented earthquake occurrence modelling method.

The hazard function, marginal probabilities  $p_t$ , of annual rupture occurrence at each segment in year  $t$  is expressed as a function of  $T_j$ :

$$p_t = \frac{F(T_j(t)+1) - F(T_j(t))}{1 - F(T_j(t))} \quad (2.3),$$

where  $T_j(t)$  is the elapsed time since the last rupture in the  $j$ th segment, and  $F(T_j(t))$  is the cumulative distribution function of the elapsed time in segment  $j$  at year  $t$ . For the case of the BPT model as interarrival time distribution,  $F(T_j(t))$  can be specified by implementing parameters  $\mu_j$ ,  $\alpha_j$  and  $T_i$  (Matthews et al., 2002):

$$F(T_j(t)) = \Phi(u_1(t)) + e^{\frac{2}{\alpha_j^2}} (\Phi(-u_2(t))) \quad (2.4),$$

$$u_1(t) = \alpha_j^{-1} [t^{\frac{1}{2}} \mu_j^{-\frac{1}{2}} - t^{-\frac{1}{2}} \mu_j^{\frac{1}{2}}] \quad (2.5),$$

$$u_2(t) = \alpha_j^{-1} [t^{\frac{1}{2}} \mu_j^{-\frac{1}{2}} + t^{-\frac{1}{2}} \mu_j^{\frac{1}{2}}] \quad (2.6),$$

where  $\Phi()$  represents the standard normal cumulative distribution function. The spatial correlation function that captures interaction between adjacent segments is defined as:

$$\rho(i, j) = \exp\left(\left(-\frac{\text{Dist}(i, j)}{\gamma}\right)^2\right) \quad (2.7),$$

where  $\text{Dist}(i, j)$  represents the absolute distance between fault segment  $i$  and  $j$  along the strike direction.  $\gamma$  is the parameter that controls the decay of the correlation of rupture occurrence with distance.

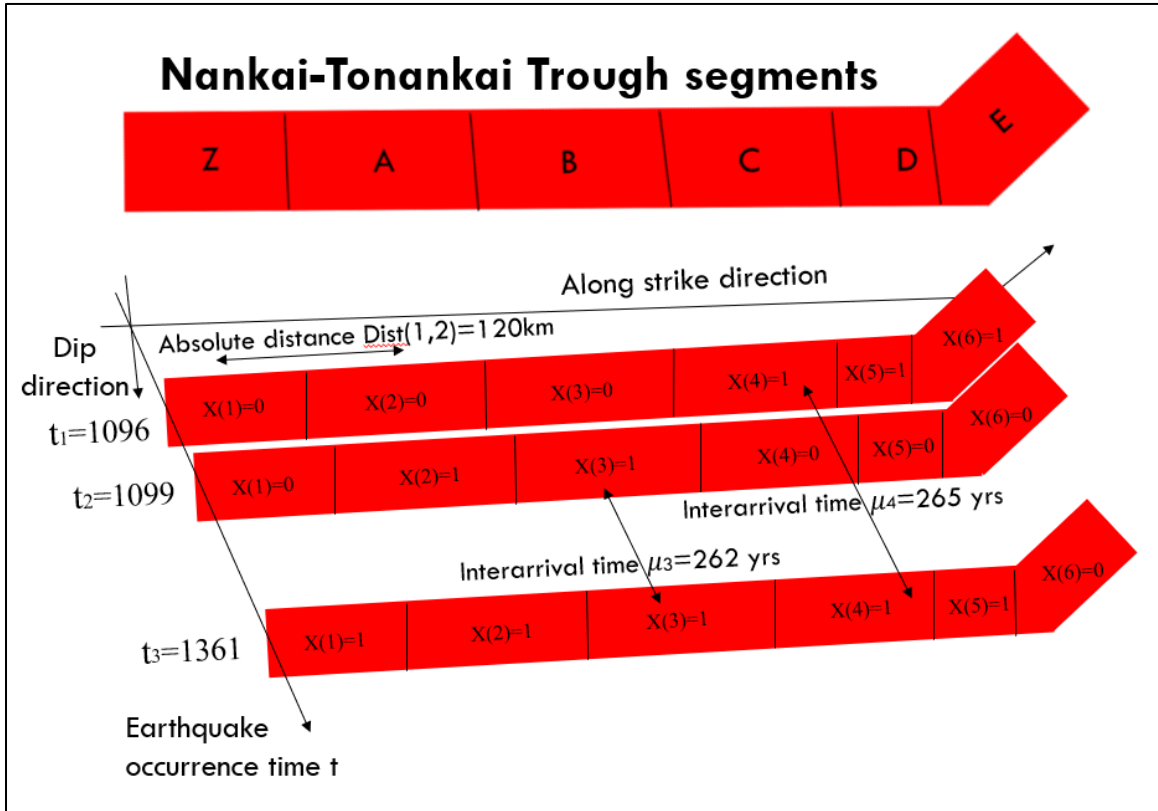


**Figure 2.6:** Illustration of the earthquake rupture segmentation model with parameters including interarrival time  $\mu$ , earthquake occurrence time  $t$ , distance between segments, and rupture condition indicator  $X$  for the 1096 Enaga earthquake, the 1099 Kowa earthquake, and the 1361 Shoei earthquake.

For sampling from the multivariate Bernoulli distribution, the copula method developed for spatially correlated data (Jin et al., 2015) is employed as the approach of approximation employed in Ceferino et al. (2020). The rupture condition of each segment is determined in each year during the simulation by making the comparison between the

standard normal cumulative distribution function  $\Phi(Z_t)$  and annual rupture probability  $p_t(j)$ :

$$X_t(j) = 1\{\Phi(Z_t(j)) < p_t(j)\} \quad (2.8),$$

where  $Z_t(j)$  is a zero-valued mean vector of normally distributed random variables. The standard cumulative distribution function of  $Z_t(j)$  is therefore uniformly distributed in  $[0,1]$  with the covariance equals to the value from the correlogram  $\rho_{i,j}$ . The binomial random process, which characterizes by the rupture condition matrix  $X_t(j)$ , is controlled by both interarrival time distribution and spatial correlogram. By replacing the type of renewal probability distributions, this multivariate Bernoulli model can also be used to simulate earthquake occurrence and to make the comparison between simulated earthquake occurrences.

Before carrying out the earthquake occurrence simulation, the spatial and temporal correlation parameters for individual segments need to be estimated from the occurrence catalogue. Ceferino et al. (2019) demonstrated two approaches for parameter estimation. A simpler approach uses the Maximum Likelihood Estimation (MLE) method, and then spatial correlation parameter  $\gamma$  is calibrated by trial and error to match the historical exceedance rates in the tectonic region and the annual seismic moment release with the simulated events. The second approach adopts the Bayesian estimation to update all parameters sequentially. Comparing with the MLE method, the Bayesian method evaluates the estimation within the model parameters by considering the joint distribution of all parameters by iterative update. For the N-segmented region, the posterior probability  $P(\alpha, \mu, \gamma|X)$  is expressed as a function of rupture history likelihood  $P(X|\alpha, \mu, \gamma)$  and prior information  $P(\alpha, \mu, \gamma)$  :

$$P(\alpha, \mu, \gamma|X) = \frac{P(X|\alpha, \mu, \gamma)P(\alpha, \mu, \gamma)}{\int \int \int P(X|\alpha, \mu, \gamma)P(\alpha, \mu, \gamma) d\alpha d\mu d\gamma} \quad (2.9),$$

The prior information  $P(\alpha, \mu, \gamma)$  is evaluated by:

$$P(\alpha, \mu, \gamma) = P(\gamma)\prod_{j=1}^N P(\mu_j)P(\alpha_j) \quad (2.10),$$

Finally, the likelihood  $P(X|\alpha, \mu, \gamma)$  of observing the rupture history is evaluated as the product of all probability of rupture occurrence  $P(X_t|T_t)$  in each of  $H$  years.

$$P(X|\alpha, \mu, \gamma) = \prod_{t=1}^H P(X_t|T_t) \quad (2.11),$$

and the rupture probability  $P(X_t|T_t)$  in year  $t$  is estimated as the probability of vector  $Z_t$  within a region defined by  $A$ . In equation 2.8,  $Z_t$  is defined as a matrix of normally distributed random variables. Therefore, region  $A$  can be interpreted as the intersection of regions  $A_j$  in individual segment  $j$

$$P(X_t|T_t) = P(\cap_{j=1}^N A_j) \quad (2.12),$$

where  $A_j = \{Z_t(j) < \Phi^{-1}[p_t(j)]\}$  if a rupture occurred or  $A_j = \{Z_t(j) > \Phi^{-1}[p_t(j)]\}$  otherwise. If the rupture occurs, the region  $A_j$  spans the region where  $Z_t(j) < \Phi^{-1}[p_t(j)]$ , while the region  $A_j$  can extend to the region where  $Z_t(j) > \Phi^{-1}[p_t(j)]$  if rupture does not occur. The Markov Chain Monte Carlo (MCMC) method is used to sample from the posterior by following the steps in Figure 2.7. As the determination of sub-segment length can be subjective, geological evidence for their corresponding earthquakes is essential for making such decisions and generating the stochastic slip models corresponding to different magnitude scenarios. Comparing with the Lima region in Peru that has a lesser number of earthquakes in the historical catalogue, the Nankai-Tonankai Trough has hosted 13 devastating megathrust earthquakes and is composed of more segments. Therefore, the Bayesian parameter update method is more suitable to evaluate individual temporal parameters between segments and the spatial correlation parameter  $\gamma$  in an automatically updating way.

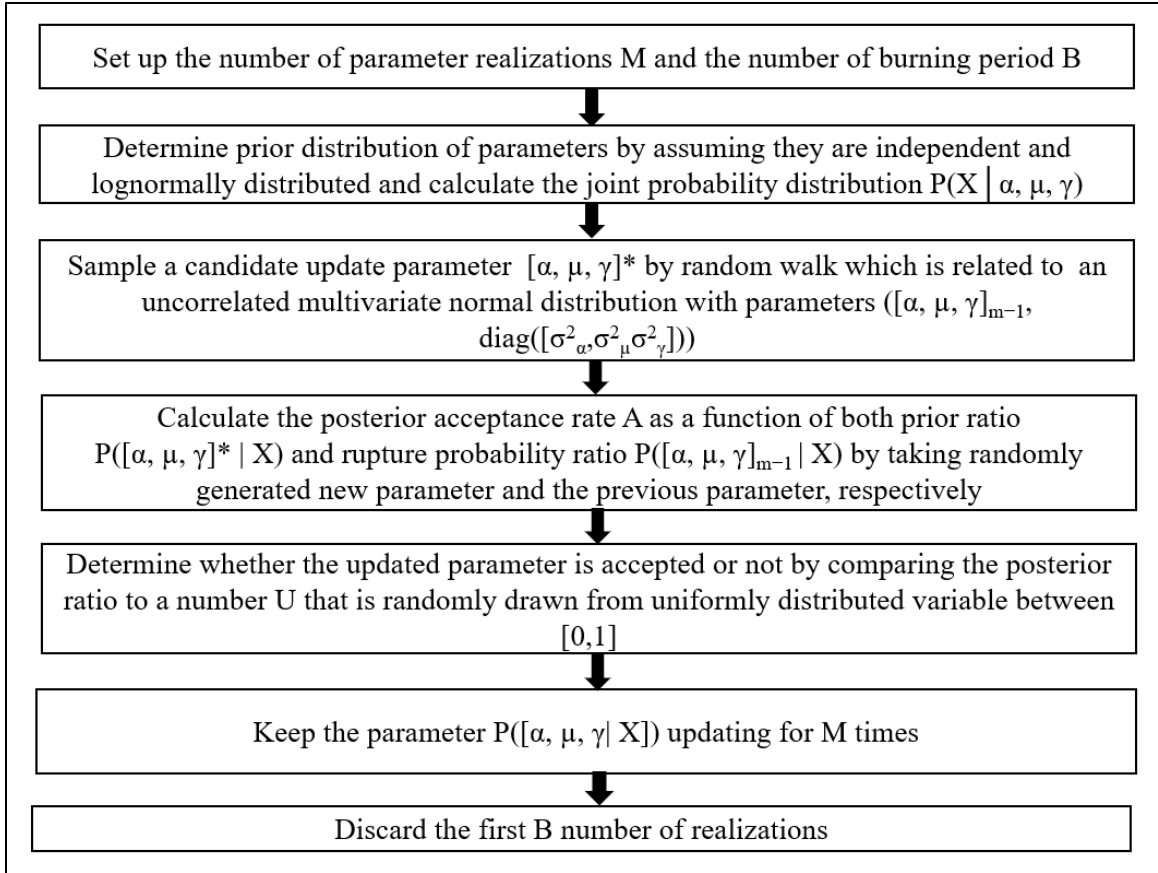


**Figure 2.7:** Flowchart of the Bayesian parameter estimation procedure using Metropolis-Hastings algorithm. The sampling process starts from the initial parameters and randomly updates to new parameters following the proposal distribution. According to the comparison between the posterior ratio and the acceptance rate, the new parameter is accepted or rejected through several iterations and reaches the desired posterior distribution.

## 2.3 Stochastic slip source models

### 2.3.1 Existing fault source models for the Nankai-Tonankai earthquakes

Faults in subduction regions show significant diversity in geometry, structure and path of rupture propagation (Lotto et al., 2019). In estimating the strong motion and tsunami hazard, the fault slip model is the key feature due to its characterization of rupture

propagation and the direct link to the seismic behaviour of earthquakes. The heterogeneous slip models are preferable, compared with homogenous slip models, which assume the whole fault plane has the uniform slip. In Ceferino et al. (2020), the ruptures are simulated with an assumption of homogeneously distributed slip on the fault. Therefore, the incorporation of heterogeneous slip models would improve the authenticity in comparison with the real ruptures. However, the choice of approaches for modelling heterogeneous slip distributions is not unique. Lotto et al. (2019) compared two types of models by setting up a simplified subduction zone geometry and removing the complex path and site effects in simulating tsunamis from earthquakes with magnitudes ranging from 7 to 9. It was shown that the homogenous slip models tend to result in lower potential energy of horizontally propagating tsunami waves and tend to underestimate the peak tsunami amplitude in comparison with the heterogeneous slip models. The underestimation of tsunami hazards caused by a homogeneous slip model, would affect applications, such as tsunami warning systems and risk assessment. Therefore, the utilization of stochastic heterogeneous slip models is desirable in probabilistic tsunami hazard assessment, which is more sensitive to the localized deformation on the whole fault plane. As both tsunami and long-period ground motion belong to the long-period processes, the same setting is also applicable to the ground motion estimation at moderate-to-long frequencies.

Furthermore, the slip distribution of source models varies depending on inversion approaches and data types. The complexity of obtaining slip distribution of the fault source plane by inverting near-source data has been investigated since the early observations of the complexity of earthquake behaviour (Beroza and Spudich, 1988). Rivera and Kanamori (2001) also supported the heterogeneous slip models of earthquake rupture by demonstrating the uniform stress field and concluded that the constant friction assumed when generating homogeneous slip models is not valid in realistic cases. Therefore, heterogeneous slip distributions are considered more suitable than homogenous slip models. In this thesis, the stochastic slip modelling method is employed to capture the representative characteristics of spatial slip distribution corresponding to each rupture scenario.



An increasing number of fault source models have been developed for the 1944 Tonankai and 1946 Nankai earthquakes during the past few decades. Figure 2.8 shows different slip models, which correspond to the Nankai earthquake and Tonankai earthquake. Sakate (1993) developed his model by using seven tsunami wave profiles by including four more sets of tsunami profile data compared to Ando (1975). The result showed the trench-side slip is well resolved by this model. The model significantly improved the previous model by reducing the variance by 45% with respect to its original value. Furthermore, Tanioka and Sakate (2001) updated the predecessor by improving three aspects: 1) division of the fault plane into 29 sub-faults; 2) variation of dip angles and locations to better fit the subducting slab; and 3) utilization of bathymetry data with a finer resolution for simulating tsunami propagation. Their result showed that the slip distribution of the 1946 Nankai earthquake has a maximum of 6 m in the locked zone off Shikoku Island, and has a local maximum of 3 m off the Kii Peninsula. Besides many slip models developed for the 1946 Nankai earthquake, the observations and data collected for the 1944 Tonankai earthquake also allow the reconstruction of the slip distribution. Kato and Ando (1997) proposed a model according to a tsunami inversion model by Satake (1993), which divided the fault into small sub-faults and calculated the vertical crustal displacement for simulating tsunami wave profiles. Baba et al. (2002) proposed a model of the two sub-faults in the subducting Philippine Sea Plate and derived their model based on tsunami wavefront data inversion as well. Furthermore, Ichinose et al. (2003), Kikuchi et al. (2003), Tanioka and Satake (2001), and Kato and Ando (1997) developed source models for the 1944 Tonankai earthquake. Unlike the 1946 Nankai earthquake, the 1944 Tonankai earthquake source models tend to have greater variations in terms of their geometry and slip distributions

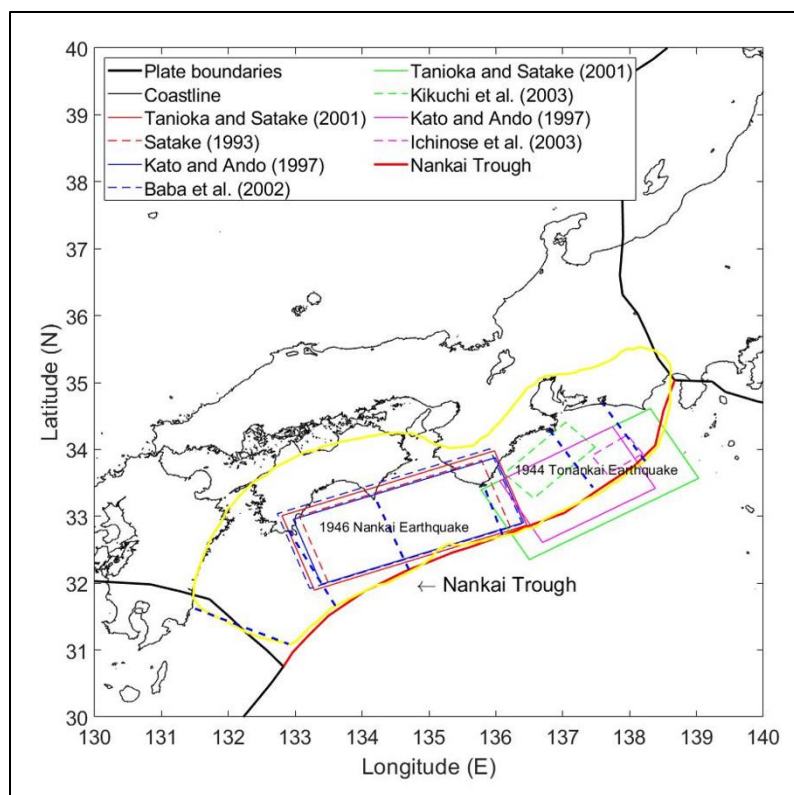


**Figure 2.8:** Nankai-Tonankai Trough fault source model geometry for the 1946 and 1944 earthquakes, and the 2012 Central Disaster Managing Center Council (tsunami) source model boundary characterized by yellow lines. From the inversion models, the source region of the 1946 earthquake is relatively better constrained in the A+B segment comparing with the source region of the 1944 earthquake, which has significantly varying fault-plane geometries from different works of literature.

For the earlier megathrust earthquakes, the number of derived fault source models drastically decreased due to both the difficulties of rupture-area estimation as well as lack of recorded data. Figure 2.9 shows source models for the 1854 Ansei earthquakes and the 1707 Hoei earthquake, which are still in good agreement with the rupture pattern shown in Figure 2.8. Table 2.2 summarizes all important parameters of the aforementioned source models, including magnitude, fault length, fault width for the 1946 and 1944 earthquakes as gathered from SRCMOD (<http://equake-rc.info/srcmod/>). For source models of even earlier earthquakes, only the fault length and magnitude are available to

constrain the possible magnitude scenarios of different rupture patterns. The rupture lengths as well as the magnitudes of all earthquakes, can only be inferred from historical records and are summarized in Figure 2.4 in the previous section. The information is used as referential values of input parameters when examining the rupture information of historical earthquakes before simulating earthquake occurrences in Chapter 3.

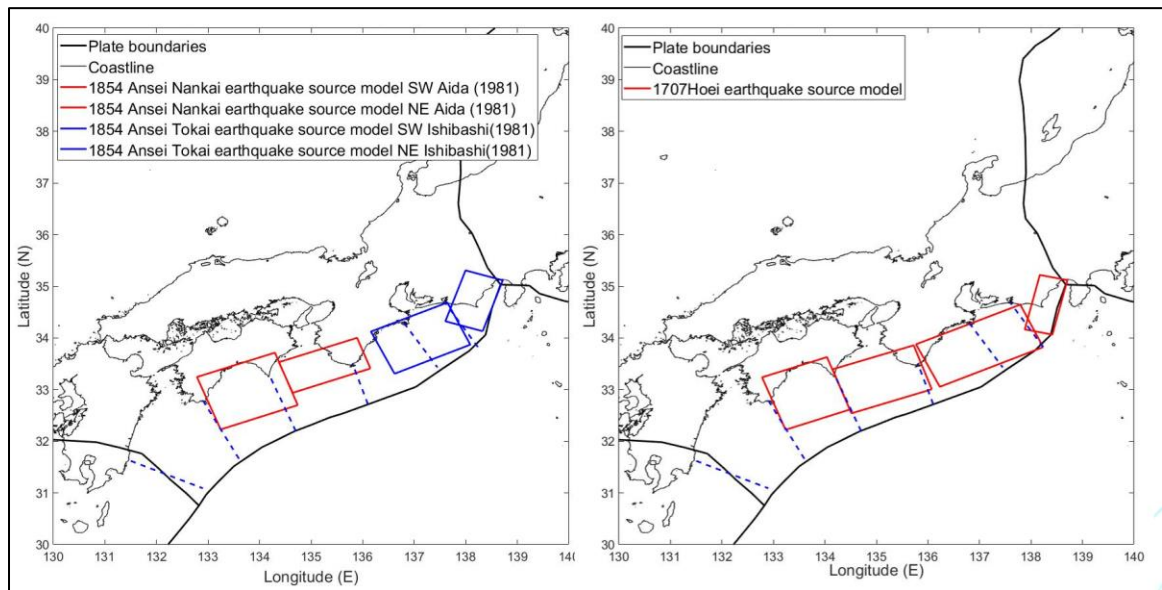


**Figure 2.9:** Source fault models for the 1854 Nankai earthquake (Aida, 1981), the 1854 Tonankai earthquake in the left figure (Ishibashi, 1981), and the 1701 Hiei earthquake in the right figure (Furumura et al., 2010).

**Table 2.2:** Finite-fault model parameters for the 1944 Tonankai earthquake and 1946 Nankai earthquake. The geometry parameters (i.e. length, width, strike, dip and rake angles) support constraining the shape and orientation of the fault, while the other parameters ( $M_w$  or seismic moment) provide an estimation of the energy released during the event.

References	Location	Magnitude ( $M_w$ )	Seismic moment (Nm)	Strike ( $^\circ$ )	Dip ( $^\circ$ )	Rake ( $^\circ$ )	Length (km)	Width (km)
------------	----------	---------------------	---------------------	---------------------	------------------	-------------------	-------------	------------

Tanioka and Satake (2001)	Nankai	8.4	4.51E+21	250	13	120	360	180
Satake (1993)	Nankai	8.3	3.31E+21	250	10	120	360	180
Kato and Ando (1997)	Nankai	8.3	4.00E+21	250	17.1	119.2	360	180
Baba et al. (2002)	Nankai	8.4	4.90E+21	250	12	120	360	180
Tanioka and Satake (2001a)	Tonankai	8.1	2.00E+21	240	8	110	315	180
Satake (1993)	Tonankai	8.1	2.00E+21	240	15	110	270	180
Kikuchi et al. (2003)	Tonankai	8.0	1.08E+21	225	15	79	140	80
Kato and Ando (1997)	Tonankai	8.2	2.80E+21	240	9.6	108.4	240	180
Ichinose et al. (2003)	Tonankai	8.0	1.31E+21	235	20	82	220	140

### 2.3.2 Stochastic fault source modelling method

The inverted kinetic source models of earthquakes can have multiple feasible solutions, which is the result of applying different data and inversion methods. Typically, the underlying data can be geodetic measurements, teleseismic data, and strong motion data. The variation of physical properties can be captured after applying Fourier analysis to transform the physical signals to the spectrum in the frequency domain. As pointed out by Andrews (1980), the slip spectrum after the 2-D Fourier transformation of the spatial slip distribution over the fault plane can be described as a function of spatial parameter  $k$  and temporal frequency parameter  $\omega$ . The source spectrum follows a  $k^{-2}$  decay in the wavenumber domain and is associated with a  $\omega^{-2}$  decay of far-field displacement in the time domain at high frequencies. Furthermore, Power et al. (1987) showed that the power spectrum density of fault slip geometry follows the power law, and the asperities and its zonation can be determined through the whole fault region.

Herrero and Bernard (1994) proposed the  $k^{-2}$  finite-source model that the slip spectrum decays proportionally to the square of wavenumber  $k$  beyond the corner wavenumber  $K_c$ , while the far-field displacement spectra decay as  $\omega^{-2}$ . The slip distribution is assumed to be fractal in the  $k^{-2}$  model, and the length scale is the characteristic source dimension  $L_c$  which is inversely proportional to  $K_c$ . Based on the  $k^{-2}$  model, Mai and Beroza (2002) developed a source model using different autocorrelation functions (ACF) in space to describe the slip distribution. After Fourier transform, the power spectral density (PSD)

in the wavenumber domain was characterized by the correlation lengths along the strike and dip directions,  $a_x$  and  $a_z$ , respectively. To obtain the best fitting ACF, Mai and Beroza (2002) tested a Gaussian, an exponential, and a von Karman ACF on 44 published finite-source models. The equations of these ACFs, as shown in Table 2.3, were used to generate the spatial random field models, which are commonly used to describe heterogeneous spatial distributions. Among the three ACFs, the random field produced using von Karman ACF showed the best agreement with the data, while the correlation lengths were positively proportional to the fault dimension. The scaling relations of correlation length with source dimension were also developed by Mai and Beroza (2002) to link the correlation lengths with fault width, fault length, and moment magnitude. Furthermore, Guatteri et al. (2003) proposed an improved method of simulating ground motions by accounting for variability in all relevant parameters, such as heterogeneous slip values and rupture speed. In that study, kinematic, dynamic, and hybrid simulated strong-motion seismograms showed good agreement with empirical response spectra after accounting for the temporal and spatial variations of slip, slip rise time, and rupture speed. As pointed out by Lavallee et al. (2006), these findings suggest that heterogeneities within earthquake source models require systematic estimation using statistical approaches instead of individual estimates.

**Table 2.3:** Three commonly used autocorrelation functions in the spatial domain and Fourier domain.

ACF/PSD type	Space domain (C(r))	Wavenumber domain (P(k))
Gaussian	$e^{-r^2}$	$\frac{a_x a_z}{2} e^{-\frac{1}{4}k^2}$
Exponential	$e^{-r}$	$\frac{a_x a_z}{(1 + k^2)^{\frac{3}{2}}}$
von Karman*	$\frac{G_H(r)}{G_H(0)}$	$\frac{a_x a_z}{(1 + k^2)^{H_n+1}}$

\*  $G_H(r) = r^{H_n} K_H(r)$  where  $K_H(r)$  is the modified Bessel function of the first kind,  $H_n$  is the Hurst number that determines the spectral decay at high wavenumbers,  $k$  is the wavenumber, and  $a_x$  and  $a_z$  are the correlation lengths along strike and dip directions, respectively.  $r$  is the distance and can be calculated as  $r = \sqrt{\frac{x^2}{a_x^2} + \frac{z^2}{a_z^2}}$ , and  $k$  can be

calculated through horizontal and vertical wavenumbers as  $k = \sqrt{a_x^2 k_x^2 + a_z^2 k_z^2}$ .

To generate a fault source model that characterizes the heterogeneous slip distribution, a probabilistic approach is applicable by accounting for the marginal distributions as well as their correlation between fault parameters (Gusev, 1992). According to the Mai-Beroza method, three main steps are involved when producing 2-D stochastic slip models: 1) interpolation of an original slip distribution; 2) spectral analysis of the slip distribution after Fourier transform; and 3) synthesis of heterogeneous slip distribution. The last step involves inverse Fourier transform of complex Fourier coefficients after incorporating a random phase matrix between 0 to  $2\pi$ . To preserve the observed stochastic nature in the simulated source model, the random field can be iteratively generated until all pre-set constraints are met. The constraints typically include the threshold of maximum slip value, location of asperities, and slip concentration ratio.

### 2.3.3 Stochastic fault source modelling for the Nankai-Tonankai Trough

For modelling stochastic slip distribution in the Nankai-Tonankai case, Goda et al. (2020) proposed an earthquake slip simulation procedure for the generation of fault parameters to be used in kinematic rupture propagation modelling. For slip distribution synthesis, the stochastic synthesis parameters and target slip parameters are the two types of parameters that need to be calculated. Using the statistical scaling relationships developed by Goda et al. (2016), the stochastic synthesis parameters and target parameters, including fault width  $W$ , fault length  $L$ , fault area  $A$ , mean slip  $D_a$ , maximum slip  $D_m$ , and correlation lengths  $a_x$  and  $a_z$  can be expressed in terms of moment magnitude  $M_w$  and their corresponding linear correlation coefficients of regression residuals. Besides, two slip synthesis parameters, the Box-Cox parameter and the Hurst number  $H_n$ , are determined via previous research. The Box-Cox power parameter, which controls the non-linear transformation of slip distribution, is determined as a variable with a mean equal to 0.312 and a standard deviation equal to 0.278. Moreover, the Hurst number controls the decay behaviour of the power spectrum at the high wavenumber range. The value of the Hurst number can be specified probabilistically by modelling it as a random variable that takes a value of 0.99 (43% chance) or is a normal random variable with a mean equal to 0.714 and a standard deviation of 0.172 (57% chance).

The parameters setting defines the desired characteristics of synthesized spatial distribution. The generation of the random field in the wavenumber domain, after applying Fourier transform on the von Karman ACF, is controlled by the Hurst number and the correlation lengths. After incorporating a random phase matrix, the inverse Fourier transform allows the heterogeneous slip distribution to be modified in the original domain. To ensure the desired features are captured, the asperity pattern is matched with the pre-set constraints of credible models or estimated depth limits. The taper functions are also applied to deep segments to ensure the decay of the slip is gradual to the nearby grids around the asperity zone. In the end, the mean and maximum slip are iteratively adjusted to agree with the targeted values. Furthermore, the preliminary probability density function is estimated based on the mean to maximum slip ratio and fault

dimensions, and is used for determining the hypocenter locations of slip models are under the realistic constraint for locations. The overall simulation processes are summarized in Figure 2.10. To obtain the most representative slip model, the spatial distribution can be repeatedly generated by using the parameters mentioned above to obtain the random field under the constraint of pre-set sub-faults and asperity zones.

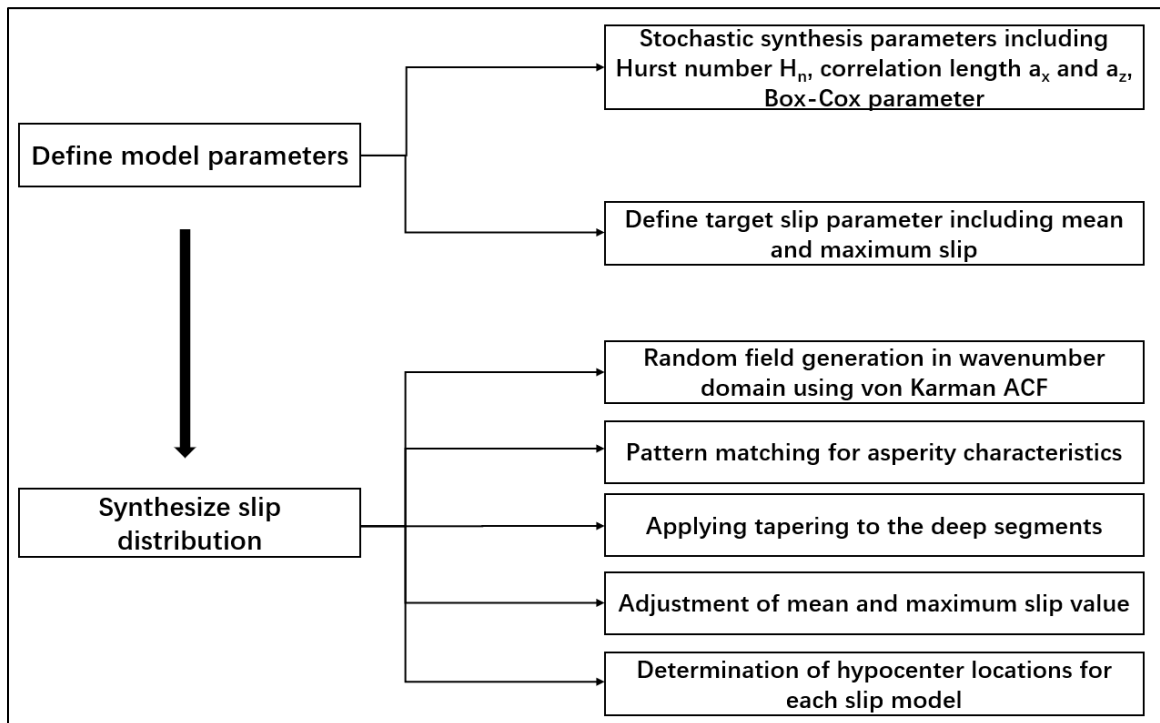


**Figure 2.10:** Flowchart of stochastic slip models generation process. The synthesis and slip parameters are defined according to scaling laws and empirical research, while the detailed slip synthesizing procedures follow Goda et al. (2020).

To apply adequate constraints to the slip model, the Nankai-Tonankai tsunami source model developed by the Central Disaster Management Council (CDMC) in 2012 of the Japanese Cabinet Office is considered. The CDMC2012 models are heterogeneous slip models developed for the extreme scenario corresponding to the Mw 9-class event of synchronized rupture scenario on the current Nankai-Tonankai Trough seismotectonic



setting. By assigning variations of the large-slip and very-large-slip areas, the CDMC2012 model adopted 11 scenarios with asperity regions varying from the Nankai segments to the Tokai segment, and includes the Kumano splay fault in the Kumano-nada area. The first five cases consider only one location of large or very large slips in each segment from A to E, while cases 6 and 7 consider the splay fault is located off the Kumano sea in segment C. The other four cases take into account two asperities located in segments C to E, B to D, A to C, and Z to B, respectively. In Figure 2.11, the first scenario is demonstrated with the single asperity located off Suruga Bay to the Kii Peninsula, while the illustration of the other 10 cases is included in Appendix A. As a summary of the characteristics of all 11 scenarios, Table 2.5 lists information regarding each of the criteria and can be used for making the comparison with the energy release estimated from simulated slip distribution models in this thesis (see Chapter 4). The collected data for specifying the earthquake slips over the fault plane mainly come from large magnitude subduction events, including the 2011 Tohoku earthquake, 2010 Chile earthquake, and 2004 Sumatra earthquake. Therefore, the sub-fault division pattern of the CDMC2012 source models is considered most realistic for reflecting the 3-D geological setting of the Nankai-Tonankai trough fault plane, although the estimated slip values in each sub-fault grid are not directly employed.

The main fault plane of the CDMC2012 models is composed of 5669 sub-faults, each having a grid size of 5 km by 5 km. Besides, extra 104 sub-faults are present in the models for representing the Kumano splay faults. The models span a total area of  $1.4 \times 10^5$  km<sup>2</sup> with a magnitude of Mw9.1, while having an average slip value of approximately 10 m. These models consider the large-slip areas (about 20 m) and very-large-slip areas (about 40 m), while restricting the large-slip areas only to consist of less than 20% of the fault area and are located in the shallow (depths less than 20 km) side of the source region. The very-large-slip areas are located within the large-slip areas and only consist of 5% of the fault area. Meanwhile, three of the key parameters for the stochastic source models, i.e. depth limit, moment magnitude corresponding to different rupture scenarios, and asperity/slip ratio, are empirically determined according to scaling relations in the literature (Thingbaijam et al., 2017; Goda et al., 2020). When producing stochastic models, all the above-mentioned fault plane information from the CDMC2012 model is

incorporated to constrain the slip distribution. In the stochastic slip simulation, the 3D non-planar information of the CDMC2012 sub-faults is mapped onto a 2D matrix with a size of 153 (strike direction) by 54 (dip direction). The starting point is set at the southwest corner location of the fault plane, and the slip value within each grid can be generated according to the assigned rupture scenario. After processing, the generated heterogeneous slip values are then mapped back to the CDMC fault plane in 3D and tested through the applied constraints.

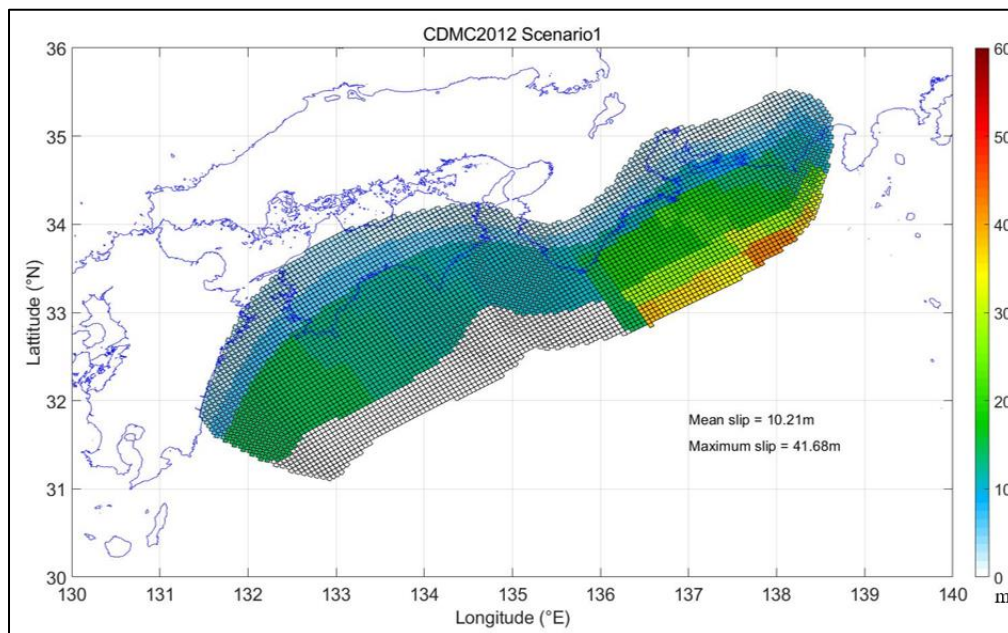


**Figure 2.11:** CDMC2012 heterogeneous fault slip model of scenario 1 that corresponds to the single asperity region located off Suruga Bay to Kii Peninsula. The entire fault plane was divided into 6557 grids with 5km width and 5km length. The large and very large asperities, with a maximum slip up to 41.68m, are dominantly located at the very shallow region (near top-edge depth) of the fault plane.

**Table 2.4:** Estimated total fault area, moment release, moment magnitude, stress drop and average slip for 11 scenarios of the CDMC2012 models

Scenario	Area (m <sup>2</sup> )	Moment release (Nm)	Moment magnitude (Mw)	Average slip (m)
1	1.4×10 <sup>11</sup>	6.1×10 <sup>22</sup>	9.1	10.3
2	1.4×10 <sup>11</sup>	6.3×10 <sup>22</sup>	9.1	10.7
3	1.4×10 <sup>11</sup>	6.4×10 <sup>22</sup>	9.1	10.9
4	1.4×10 <sup>11</sup>	6.4×10 <sup>22</sup>	9.1	10.8
5	1.4×10 <sup>11</sup>	6.3×10 <sup>22</sup>	9.1	10.7
6	1.4×10 <sup>11</sup>	5.4×10 <sup>22</sup>	9.1	9.0
7	1.4×10 <sup>11</sup>	5.3×10 <sup>22</sup>	9.1	8.8
8	1.4×10 <sup>11</sup>	6.2×10 <sup>22</sup>	9.1	10.4
9	1.4×10 <sup>11</sup>	6.7×10 <sup>22</sup>	9.1	11.3
10	1.4×10 <sup>11</sup>	6.1×10 <sup>22</sup>	9.1	10.8
11	1.4×10 <sup>11</sup>	6.1×10 <sup>22</sup>	9.1	11.2

## Chapter 3

### 3 Nankai-Tonankai Trough earthquake occurrence simulation

This chapter focuses on the methodology and simulation of earthquake occurrence of the Nankai-Tonankai megathrust earthquakes. As introduced in Chapter 1, multiple settings are implemented to examine the validity of the method and test the sensitivity of the model to the parameters. The rupture region is first divided into a 3-segment model and a 6-segment model, with segment Z being included in the 6-segment model. For each model, the historical rupture conditions are assigned based on the evidence gathered in Chapter 2. In light of these geological, geophysical and historical evidence (Section 2.1), six historical earthquake catalogues are set to capture the potential uncertainty related to earthquake occurrence and rupture pattern, respectively. Two base catalogues are set by using the historical rupture information to define the rupture condition during past megathrust earthquakes for 3-segment and 6-segment models, respectively. Furthermore, two more catalogues are developed on the basis of the base catalogue for each model by incorporating the additional hypothesis regarding the historical rupture condition of one specific earthquake. The variation in the historical earthquake catalogues aims to allow testing the sensitivity of the earthquake occurrence modelling method to the input parameters (i.e. interarrival time and aperiodicity of historical earthquakes).

Before carrying out earthquake occurrence simulation, the earthquake occurrence simulation parameters are individually estimated for all six historical earthquake catalogues using the Bayesian update method (Section 2.2.2) and then employed in carrying out simulations. The spatial correlation of rupture occurrence between segments is directly estimated using the Markov Chain Monte Carlo method, instead of estimating the decaying constant  $\gamma$  first and then calculating the spatial correlation. Furthermore, four types of probabilistic functions, including BPT, exponential, Weibull, and lognormal distributions (Section 2.2.1), are employed in the earthquake occurrence simulation for each catalogue of both 3-segment and 6-segment models. The difference between time-independent and time-dependent earthquake occurrence simulation results can therefore be examined. As the initial step of the hybrid earthquake simulation method, the

earthquake occurrence simulation results are further combined with the stochastic source models (Chapter 4) and the regional ground motion simulations (Chapter 5).

### 3.1 Earthquake occurrence simulation set-up

The segmentation pattern of the rupture region plays a dominant role in estimating seismic moment release for earthquakes. However, the rupture histories of the past major earthquakes can be interpreted differently because of uncertain geological and historical evidence. The rupture model of the Nankai-Tonankai Trough is divided into two types, i.e. 3-segment and 6-segment rupture models, as shown in Figure 3.1 and Figure 3.2, respectively. The two models account for different views on fault segmentation when carrying out earthquake simulation and spatial slip synthesis. The 3-segment model only incorporates the rupture segments from A to E, and the Nankai segments A and B and the Tonankai segments C and D are combined as one larger segment, respectively, due to the spatial correlations between the high intrinsic coupling areas and rupture areas. The model consisting of three macro segments (Nankai A+B, Tonankai C+D, Tokai E) is widely used to describe the rupture pattern in the Nankai-Tonankai megathrust. Meanwhile, the Hyuga-nada segment Z has been increasingly concerned as a potential segment that can rupture both individually and synchronously with other segments (Furumura et al., 2011; Garrett et al., 2016). Due to the lack of supporting geological and geophysical evidence, the Hyuga-nada segment is less certain to be included as a part of the Nankai-Tonankai megathrust. By incorporating the Hyuga-nada segment into the commonly accepted five-segment model, the total rupture length fits better to the estimated total moment release of extremely high magnitude of megathrust earthquakes (i.e. Mw9.1 for the whole region rupture). This additional segment also behaved as one of the rupture segments and is supported by a limited number of geological/geophysical evidence obtained along with coastal areas for certain events (1707 Hoei earthquake and 684 Hakuho earthquake). Compared with the 3-segment model having fewer parameters, the 6-segment model is more complicated in that the whole region is divided into six individual segments from Z to E. Therefore, the total number of spatial and temporal parameters increases, and parameter estimation requires more computational resources.

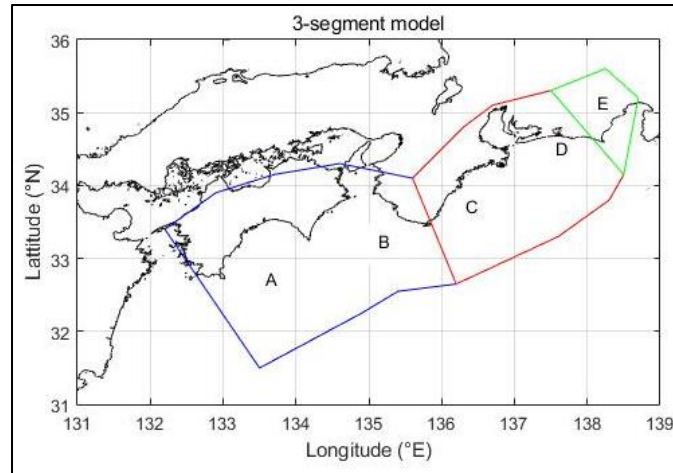


**Figure 3.1:** 3-segment model consisting of segments A+B, C+D, and E from west to east according to the historical occurrence pattern. The first segment comprises segments A and B, while the second segment is composed of segments C and D due to their high spatial correlation to experience a simultaneous rupture. The Tokai segment, which ruptures less frequently and only ruptured together with the second segment, is counted as the third segment.

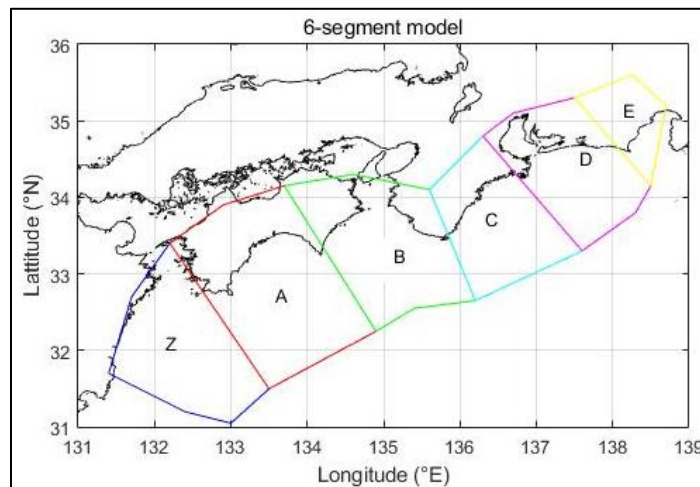


**Figure 3.2:** 6-segment model consisting of segments Z to E from west to east. All segments from A to E are count as one individual segment, unlike the 3-segment model, while the Hyuga-nada segment Z is incorporated as an additional source region in this model.

To evaluate the impact on earthquake simulation caused by varying input earthquake catalogues, the base earthquake catalogue is set primarily based on the earthquake evidence summarized by Ishibashi (2004) and Garrett et al. (2016). In addition to the base catalogue, two additional catalogues are implemented by considering: 1) the 1099 event was not a Nankai earthquake, and the 1096 event ruptured the entire Nankai-Tonankai Trough following Ishibashi (2015)'s hypothesis; and 2) the 1605 earthquake ruptured Nankai segments only. By combining the two types of segment models with the three sets of historical earthquake catalogues, six sets of input earthquake catalogues are developed and are summarized in Table 3.1 and Table 3.2, respectively. All catalogues seem very similar in that only one earthquake has a different rupture condition, as highlighted by the red color. However, due to the limited number of data (13 historical earthquakes), the variation in rupture pattern of a single historical event would lead to a significant change in spatial and temporal correlation described by the earthquake catalogue in specific segments. Thus, the estimated parameters (mean interarrival time, aperiodicity and spatial correlation) are expected to vary between different catalogues. After parameter estimation for each catalogue, spatial and temporal parameters regarding historical earthquake occurrences in each segment are set before simulations. For each segment model, the segment length, rupture history, and elapsed time are obtained from literature, while the rupture areas and seismic moment release are calculated based on moment magnitudes through earthquake source scaling relationships (Thingbaijam et al., 2017).

**Table 3.1:** Historical earthquake catalogues and corresponding rupture segments for the 3-segment model.

Base catalogue 1		Earthquake catalogue 2		Earthquake catalogue 3	
Event (Year)	Segments	Event (Year)	Segments	Event (Year)	Segments
684	A+B C+D E	684	A+B C+D E	684	A+B C+D E
887	A+B C+D	887	A+B C+D	887	A+B C+D
1096	C+D E	1096	A+B C+D E	1096	C+D E
1099	A+B			1099	A+B
1361	A+B C+D E	1361	A+B C+D E	1361	A+B C+D E
1498	A+B C+D E	1498	A+B C+D E	1498	A+B C+D E
1605	A+B C+D E	1605	A+B C+D E	1605	A+B
1707	A+B C+D E	1707	A+B C+D E	1707	A+B C+D E
1854	C+D E	1854	C+D E	1854	C+D E
1854	A+B	1854	A+B	1854	A+B
1944	C+D	1944	C+D	1944	C+D
1946	A+B	1946	A+B	1946	A+B



**Table 3.2:** Historical earthquake catalogues and corresponding rupture segments for the 6-segment model.

Base catalogue 1		Earthquake catalogue 2		Earthquake catalogue 3	
Event (Year)	Segments	Event (Year)	Segments	Event (Year)	Segments
684	Z A B C D E	684	Z A B C D E	684	Z A B C D E
887	A B C D	887	A B C D	887	A B C D
1096	C D E	1096	Z A B C D E	1096	C D E
1099	A B			1099	A B
1361	Z A B C D E	1361	Z A B C D E	1361	Z A B C D E
1498	A B C D E	1498	A B C D E	1498	A B C D E
1605	A B C D E	1605	A B C D E	1605	A B
1707	Z A B C D E	1707	Z A B C D E	1707	Z A B C D E
1854	C D E	1854	C D E	1854	C D E
1854	A B	1854	A B	1854	A B
1944	C D	1944	C D	1944	C D
1946	A B	1946	A B	1946	A B
1968	Z	1968	Z	1968	Z

## 3.2 Bayesian parameter estimation using MCMC

### 3.2.1 Input parameter setting

According to the methodology described in Section 2.2.2, Bayesian parameter estimation is performed to simultaneously obtain all parameters, i.e. mean interarrival time ( $\mu$ ), aperiodicity ( $\alpha$ ), and spatial correlation ( $\rho$ ), via a random walk approach. The computational cost increases with the dimensionality of the model for the segment model with more numbers of parameters and requires more computational time. The temporal parameters, i.e. interarrival times and aperiodicities, are evaluated for every segment in the model, and the spatial correlations are primarily defined over the separation distances between segments.

The 3-segment model has fewer spatial correlation parameters. The spatial correlation  $\rho$  between each pair of segments is indicated as  $\rho_{ij}$ , where  $i$  and  $j$  are the segment numbers.

To save the computational time for the 6-segment model, the spatial correlation parameters are assumed to be the same for certain cases. For the spatial correlation between the segment and its adjacent segment, the Nankai (A and B) and Tonankai (C and D) segments have the highest spatial correlation to rupture together based on their historical rupture patterns. Therefore, the same  $\rho$  is assumed for the Nankai and Tonankai segments and is different from other adjacent segment ruptures (e.g., Z and A; B and C). The constant  $\rho_1$  and  $\rho_2$  are assigned for adjacent-segment spatial correlation corresponding to the Nankai and Tonankai segments, and other cases, respectively. The constant  $\rho_3$  is set for spatial correlation between segments that are separated by one segment. For even greater separation greater than or equal to two segments, the correlation decaying trend is considered relatively smooth when separation continues increasing. Thus, the constant  $\rho_4$  is assigned for the spatial correlation of segments with larger separations. In Table 3.3, the parameters within each correlation matrix of the two types of segment models are demonstrated.

**Table 3.3:** Spatial correlations from all segments to the other segment for both 3-segment and 6-segment models.

<b>3-segment model correlation matrix</b>						
segment #	<b>1</b>	<b>2</b>	<b>3</b>			
<b>1 (Nankai segments A+B)</b>	1	$\rho_{12}$	$\rho_{13}$			
<b>2 (Tonankai segments C+D)</b>	$\rho_{12}$	1	$\rho_{23}$			
<b>3 (Tokai segment E)</b>	$\rho_{13}$	$\rho_{23}$	1			
<b>6-segment model correlation matrix</b>						
segment #	<b>1</b>	<b>2</b>	<b>3</b>	<b>4</b>	<b>5</b>	<b>6</b>
<b>1 (Hyuga segment Z)</b>	1	$\rho_2$	$\rho_3$	$\rho_4$	$\rho_4$	$\rho_4$
<b>2 (Nankai Tosa-oki segment A)</b>	$\rho_2$	1	$\rho_1$	$\rho_3$	$\rho_4$	$\rho_4$
<b>3 (Nankai Kii-oki segment B)</b>	$\rho_3$	$\rho_1$	1	$\rho_2$	$\rho_3$	$\rho_4$
<b>4 (Tonankai Kumano-nada segments C)</b>	$\rho_4$	$\rho_3$	$\rho_2$	1	$\rho_1$	$\rho_3$
<b>5 (Tonankai Enshu-nadasegments D)</b>	$\rho_4$	$\rho_4$	$\rho_3$	$\rho_1$	1	$\rho_2$
<b>6 (Tokai segment E)</b>	$\rho_4$	$\rho_4$	$\rho_4$	$\rho_3$	$\rho_2$	1

The sampling process of parameters is conducted using the MCMC Metropolis-Hastings algorithm, which generates random samples proportional to the desired probability distribution. The process starts from initial inputs sampled from the prior lognormal distribution. For each iteration, parameters are constrained to be within specified ranges when performing updates. The mean interarrival time is limited between 10 and 500 years, while the range of aperiodicity and spatial correlation constant are set as from 0.05 to 1 and from 0 to 1, respectively. To examine the effect of choice of initial values on

parameter estimation, different values of initial parameters are tested by taking the minimum, maximum, and MLE results, respectively. The random walk is then performed to generate the next set of parameters based on the initial parameters and the proposal distribution, which is set as the normal distribution. Both prior and proposal distributions are assigned following Ceferino et al.'s (2019) suggestions. As the acceptance ratio after the random walk can be calculated by dividing the probability of observing the new parameter by that of the last updated parameter, the success or failure of the random walk is determined by making a comparison between the acceptance rate and a uniform random number between 0 and 1. The process of acceptance or rejection is repeated many times. In the end, the posterior distribution of the updated parameters converges, staying near the high probability density region and occasionally falling into the lower probability density region. By building up the histogram of all sampled parameters, the value with the highest probability for each parameter is picked after disregarding those generated during the burning period. All starting values achieve equilibrium, where the updated parameters show the convergence to the most likely values of the parameters, after a similar burning period and reach about the same value.

### 3.2.2 Parameter estimation results

For each catalogue of the 3-segment and 6-segment models, the parameters are updated 20,000 times, and the first 1500 results are discarded because the parameters are not yet reached the desired distributions. Figure 3.3 demonstrates the estimated mean interarrival time and aperiodicity for segment 1 (i.e. Nankai segments A and B) in the 3-segment model. It can be observed from the upper panels that updated aperiodicity fluctuates more widely than the mean interarrival time, making it hard to interpret the exact value of aperiodicity visually. To capture the most probable value during the update, the probabilistic distribution of different values of parameters is calculated and illustrated as the red curve to highlight the maximum posterior probability. As shown in the lower panels, the combined Nankai segment of the 3-segment model has a mean interarrival

time of 159 years with an aperiodicity of 0.3961, as highlighted by the red stars. The spatial correlation constant between segments is determined by the same method as shown in Figure 3.4. To compare the prior distribution with the posterior distribution, both distributions are plotted on the same figure after MCMC parameters are updated. The prior distribution is plotted using the MLE results, while the posterior distribution is determined by the normalized distribution of interarrival times. Large differences between the shape of the two curves are observed and indicate the prior distribution is not controlling the posterior distribution of the parameters and the main effect comes from the data.

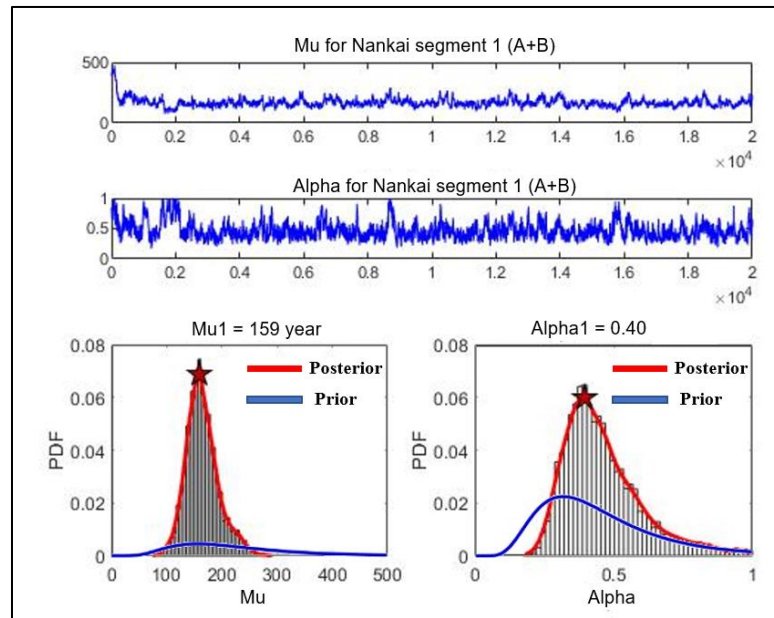


**Figure 3.3:** Interarrival time and aperiodicity updating for segment 1 (Nankai segments A and B) of the 3-segment model. The upper panel shows the updated values of interarrival time  $\mu$  and aperiodicity  $\alpha$  during the 20000 iterations, while the lower panels show the prior distribution and posterior distribution of the parameters. As indicated by the red star, the  $\mu$  and  $\alpha$  are most probably having the values of  $\sim 159$  years and 0.396, respectively.

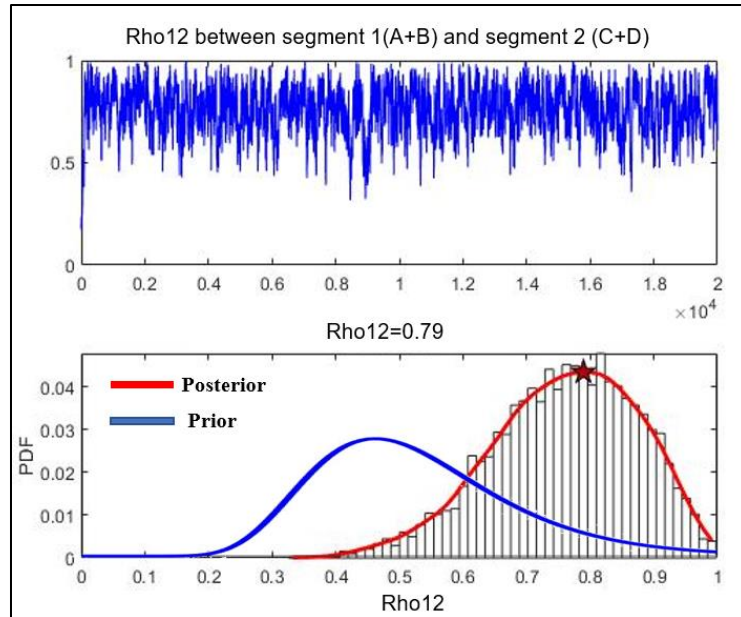


**Figure 3.4:** Updated spatial correlation between segment 1 and segment 2 (Nankai segments A and B, and segments C and D) of the 3-segment model. The upper panel shows the updated values of spatial correlation  $\gamma$  during the 20000 iterations, while the lower panels show the prior distribution and posterior distribution of the parameter. As indicated by the red star,  $\gamma$  is most probably having a value of  $\sim 0.789$  for spatial correlation between the Nankai and Tonankai segment.

The estimated parameters for all catalogues are summarized in Table 3.4 and Table 3.5 for the 3-segment and 6-segment models, respectively. For both models, the Nankai and Tonankai ruptures tend to have shorter interarrival times than the Tokai segment, while the 6-segment model shows the additional Hyuga-nada segment having a mean interarrival time twice longer than the other segments. The estimated interarrival times fit well with the seismicity of each segment observed from the historical records. Both Tonankai and Nankai segments have estimated mean interarrival time of around 150 years. The Tokai segment, which ruptures less frequently with the Tonankai segment, has an estimated mean interarrival time of around 190 years. In the 6-segment model, the least active Hyuga-nada segment has an estimated mean interarrival time of around 380 years. Moreover, the aperiodicity with values around 0.5 indicates the relative periodic

occurrence of megathrust earthquakes and falls under the range from global statistics of this parameter (Sykes and Menke, 2006).

The spatial correlation parameters of the 3-segment model indicate a high probability of synchronized rupture for the Tonankai-Tokai segments with a correlation value of around 0.9. At the same time, the Nankai segment has a correlation value of around 0.8 with the Tonankai segment, indicating their less probability to rupture together. An even lower chance of simultaneous rupture of the Nankai segment with the Tokai segment is indicated by a correlation value of around 0.7, which agrees with the Nankai-Tonankai trough historical rupture pattern. For the 6-segment model, the correlations between the Nankai segments A and B and between the Tonankai segments C and D are very high, with a value around 0.95. The correlation between other segments to their adjacent segment decreases to 0.8-0.85, which agrees with the realistic situation that Tokai and Hyuga-nada segments rupture less synchronously with their adjacent segments. Noticeably, the standard deviations of parameters of individual segments are correlated to the number of available data. For instance, the most seismically inactive Hyuga-nada segment in the 6-segment model has the largest standard deviation when estimating its mean interarrival time and aperiodicity. As the separation between segments increases, the spatial correlation is decreased, resembling the decreasing potential of synchronized segments at a larger separation distance. The estimated parameters follow intuition and agree with the historical seismic characteristics.

**Table 3.4:** Bayesian estimated parameters for the 3-segment model.

MCMC parameter	Historical earthquake catalogues		
	Base	1096 case	1605 case
$\mu 1$ (year)	159 ( $\pm 37$ )	155 ( $\pm 36$ )	153( $\pm 40$ )
$\mu 2$ (year)	154 ( $\pm 33$ )	150 ( $\pm 34$ )	173( $\pm 38$ )
$\mu 3$ (year)	191 ( $\pm 46$ )	183 ( $\pm 46$ )	219 ( $\pm 51$ )

$\alpha_1$	0.40 ( $\pm 0.14$ )	0.40 ( $\pm 0.15$ )	0.38 ( $\pm 0.14$ )
$\alpha_2$	0.40 ( $\pm 0.13$ )	0.43 ( $\pm 0.13$ )	0.42 ( $\pm 0.16$ )
$\alpha_3$	0.47 ( $\pm 0.15$ )	0.51 ( $\pm 0.14$ )	0.40 ( $\pm 0.14$ )
$\rho_{12}$	0.79 ( $\pm 0.12$ )	0.87 ( $\pm 0.11$ )	0.75 ( $\pm 0.12$ )
$\rho_{13}$	0.72 ( $\pm 0.12$ )	0.79 ( $\pm 0.12$ )	0.63 ( $\pm 0.12$ )
$\rho_{23}$	0.90 ( $\pm 0.09$ )	0.91 ( $\pm 0.10$ )	0.86 ( $\pm 0.10$ )

\* $\rho_{12}$ : Spatial correlation between Nankai segment 1 and Tonankai segment 2

$\rho_{13}$ : Spatial correlation between Nankai segment 1 and Tokai segment 3

$\rho_{23}$ : Spatial correlation between Tonankai segment 2 and Tokai segment 3

**Table 3.5:** Bayesian estimated parameters for the 6-segment model.

MCMC parameter	Historical earthquake catalogues		
	Base	1096 case	1605 case
$\mu_1$ (year)	389 ( $\pm 75$ )	387 ( $\pm 62$ )	342 ( $\pm 80$ )
$\mu_2$ (year)	155 ( $\pm 33$ )	164 ( $\pm 36$ )	145 ( $\pm 60$ )
$\mu_3$ (year)	171 ( $\pm 62$ )	161 ( $\pm 36$ )	149 ( $\pm 58$ )
$\mu_4$ (year)	150 ( $\pm 67$ )	157 ( $\pm 42$ )	169 ( $\pm 56$ )
$\mu_5$ (year)	156 ( $\pm 46$ )	151 ( $\pm 39$ )	178 ( $\pm 41$ )
$\mu_6$ (year)	184 ( $\pm 50$ )	199 ( $\pm 50$ )	209 ( $\pm 46$ )
$\alpha_1$	0.38 ( $\pm 0.16$ )	0.35 ( $\pm 0.17$ )	0.36 ( $\pm 0.18$ )
$\alpha_2$	0.41 ( $\pm 0.14$ )	0.39 ( $\pm 0.15$ )	0.44 ( $\pm 0.16$ )
$\alpha_3$	0.42 ( $\pm 0.15$ )	0.41 ( $\pm 0.13$ )	0.40 ( $\pm 0.16$ )



$\alpha 4$	0.42 ( $\pm 0.14$ )	0.43 ( $\pm 0.14$ )	0.39 ( $\pm 0.16$ )
$\alpha 5$	0.44 ( $\pm 0.15$ )	0.43 ( $\pm 0.14$ )	0.41 ( $\pm 0.15$ )
$\alpha 6$	0.45 ( $\pm 0.16$ )	0.48 ( $\pm 0.14$ )	0.42 ( $\pm 0.13$ )
$\rho 1$	0.97 ( $\pm 0.04$ )	0.95 ( $\pm 0.05$ )	0.97 ( $\pm 0.04$ )
$\rho 2$	0.84 ( $\pm 0.08$ )	0.86 ( $\pm 0.08$ )	0.80 ( $\pm 0.08$ )
$\rho 3$	0.80 ( $\pm 0.08$ )	0.83 ( $\pm 0.07$ )	0.75 ( $\pm 0.08$ )
$\rho 4$	0.76 ( $\pm 0.09$ )	0.82 ( $\pm 0.08$ )	0.72 ( $\pm 0.09$ )

\* $\rho 1$ : Spatial correlation between Nankai (A and B) or Tonankai (C and D) segments

$\rho 2$ : Spatial correlation between any two adjacent segments except Nankai (A and B) or Tonankai (C and D) segments.

$\rho 3$ : Spatial correlation between any two segments with separation of 1 segment

$\rho 4$ : Spatial correlation between any two segments with separation greater than one segment

By employing the same type of input catalogue, both 3-segment and 6-segment models generate similar values of temporal and spatial parameters. However, the estimated values vary when different input catalogues (Table 3.1 and Table 3.2) are used. For example, when using the 1096 catalogue (the catalogue incorporating the whole-region rupture hypothesis for the 1096 earthquake), the mean interarrival time is decreased, while the aperiodicity and spatial correlation are increased for all segments compared with the base model. Besides, the 1605 catalogue (the catalogue incorporating the Nankai-region rupture hypothesis for the 1605 earthquake) predominantly affects the estimated parameter values. The mean interarrival times of the Tonankai and Tokai segments are increased by about 20 years, while those of the Nankai and Hyuga-nada segments are decreased by 20 to 40 years. Comparing with the mean interarrival time, the influence on the values of aperiodicity is moderate for both 3-segment and 6-segment models, and the spatial correlations between all segments are decreased due to the

absence of ruptures in the Tonankai and Tokai segments, except for the correlation between Tonankai (A+B) and Nankai (C+D) segments, after incorporating the 1605 hypothesis. From the parameter estimates caused by different input catalogues, it is evident that the obscure records will affect the parameter estimations and, therefore, the earthquake occurrence simulation. The extent of influence is dominated by the lacking or excess of certain catalogue information.

### 3.3 Earthquake occurrence simulation results for Nankai-Tonankai Trough

The starting time of simulation in each segment is set to be the occurrence time of the last earthquake. Thus, the Hyuga-nada, Nankai and Tonankai segments have similar simulation starting times, while the Tokai segment has a much earlier starting time. The simulation process starts by setting the elapsed time of each segment for the 3-segment model and 6-segment model individually, and the simulation follows the procedure described in Section 2.2. To avoid the uncertainties associated with lacking simulation, 20000 earthquake occurrence simulations are then implemented for a duration of 50 years using the same set of parameters for each catalogue. After accounting for the elapsed time of each segment, the simulation no longer starts from the initial condition due to the stress has started accumulation during the unruptured stage. This temporal dependency is captured by the hazard function in each segment, that the failure rate is starting from certain values instead of 0 due to the elapsed-time effect. Meanwhile, four types of distribution functions, including exponential, BPT, lognormal, and Weibull distributions, are employed to study the importance of the assumed interarrival time distribution in the multivariate Bernoulli method. Historically, the immediate occurrence of an earthquake in an unruptured segment after another, like the 1854 Ansei twin earthquakes, is possible and also appears in the simulation. For the second rupture, the elapsed-time effect no longer exists, and the simulation starts from the initial condition (year 0). Thus, the simulation results are separated into two sets of plots to distinguish the first occurrence from the second occurrence. For demonstration, Figure 3.5 and Figure 3.6 illustrate the first and second earthquake occurrences simulated using the base catalogue within the 6-

segment model. During the 20000 simulations, the number of ruptures in each segment is counted and plotted against the interarrival times in normalized histograms. Moreover, the probability density functions of each assumed distribution are calculated using the simulation parameters and plotted as red curves with the histograms of the simulation results. Figure 3.5 indicates that all assigned probability distributions agree well with the histograms for the first earthquake occurrence of all simulated results. Therefore, the consistency between the assumed probabilistic distribution and the simulation results is achieved at each segment after incorporating the multi-segment spatial correlation.

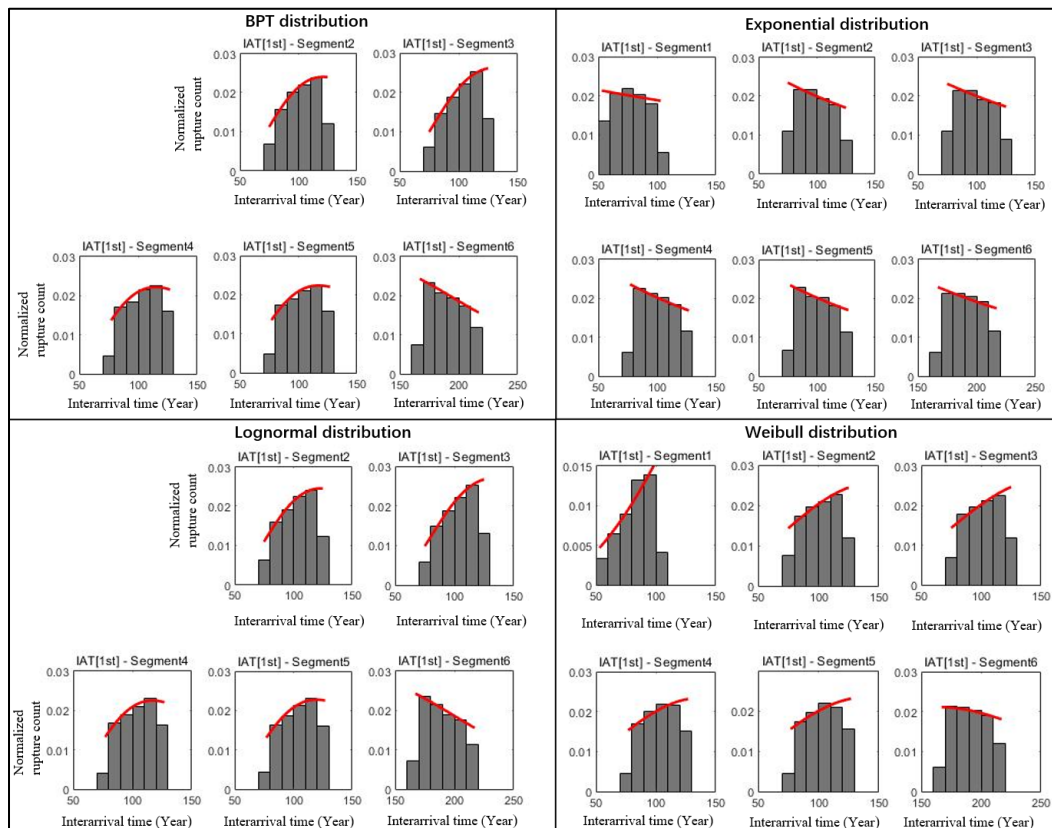


Figure 3.5: Nankai-Tonankai earthquake occurrence simulation of the 6-segment model results for the first occurrence in the next 50 years using the base catalogue. For each segment, the assumed probabilistic distribution is plotted as the red curve using the simulation parameters, while the simulated earthquakes during 20000 simulations in each segment are plotted as histograms. As illustrated in all figures, the x-axis indicates the

mean interarrival time (IAT) of the simulated earthquakes, and the y-axis represents the normalized number of earthquakes in each 10-year bin. By observing the agreement from the assumed distribution to the simulated occurrences, the consistency of the model is examined for all simulated results.

After adding the elapsed time of each segment to the simulated earthquake that occurs during the next 50 years, the Nankai and Tonankai segments have a mean occurrence time of about 100 years, and the Tokai segment has a mean occurrence time of about 200 years since their last ruptures. Importantly, the simulation results of the Hyuga-nada segment significantly differ, depending on the chosen interarrival time distribution. For the BPT and lognormal distributions, the simulation indicates that the Hyuga-nada segment is unlikely to rupture in the next 50 years. However, the results by implementing the exponential and Weibull distributions suggest the Hyuga-nada segment can rupture 80 years after its last occurrence. Noteworthy, when the sample numbers and the mean occurrence time are summarized in Table 3.6, the earthquake simulation result shows that only 264 samples of Weibull distribution are generated corresponding to the rupture of the Hyuga-nada segment with a relatively short period if an earthquake occurs. Therefore, all three time-dependent models mainly suggest a very low probability of rupture of the Hyuga-nada segment in the next 50 years. For the Tokai segment, which last ruptured during the 1854 Ansei I earthquake, the likelihood of rupture estimated from time-dependent models is extremely high, with the sample numbers from 8000 to 9000. The main reason is that the hazard rate of time-dependent distributions increases over time, as illustrated in Figure 2.5. Unlike the other distributions, the exponential distribution assumes the rupture probability is independent of the previous earthquake occurrence. Therefore, the time-independent model only has 4773 samples of rupture in the Tokai segment due to its longer interarrival time than the Tonankai and Nankai segments.

For the second occurrence of an earthquake during the same sequence of simulation, the probability distribution functions (red curves) show disagreement with the histogram of simulation results by using the exponential and Weibull distributions, as plotted in Figure

3.6. This is because the total simulation duration is only 50 years, and simulation does not span over a sufficient duration to experience the second occurrence of each segment. It is noticeable that the BPT and lognormal distributions tend to generate zero simulation results for the second earthquake occurring during the next 50 years. The simulation result agrees with the hazard rate functions shown in Figure 2.5; both BPT and lognormal distributions show extremely low rates of failure at the beginning. On the other hand, the number of simulated ruptures using the Weibull distribution also agrees with the impossibility of the second earthquake occurring in the Hyuga-nada segment. Moreover, the simulated rupture of the second rupture in other segments rarely occurs. All three time-dependent distribution tends to agree with the very low potential of hosting a second rupture. Nonetheless, the exponential distribution remains to generate the second earthquake with a relatively large sample number because it ignores the dependency on the previous rupture. Thus, all segments are considered to have the possibility to rupture when employing the exponential distribution, while the Nankai and Tonankai segments have a much higher potential to rupture than the other segments.

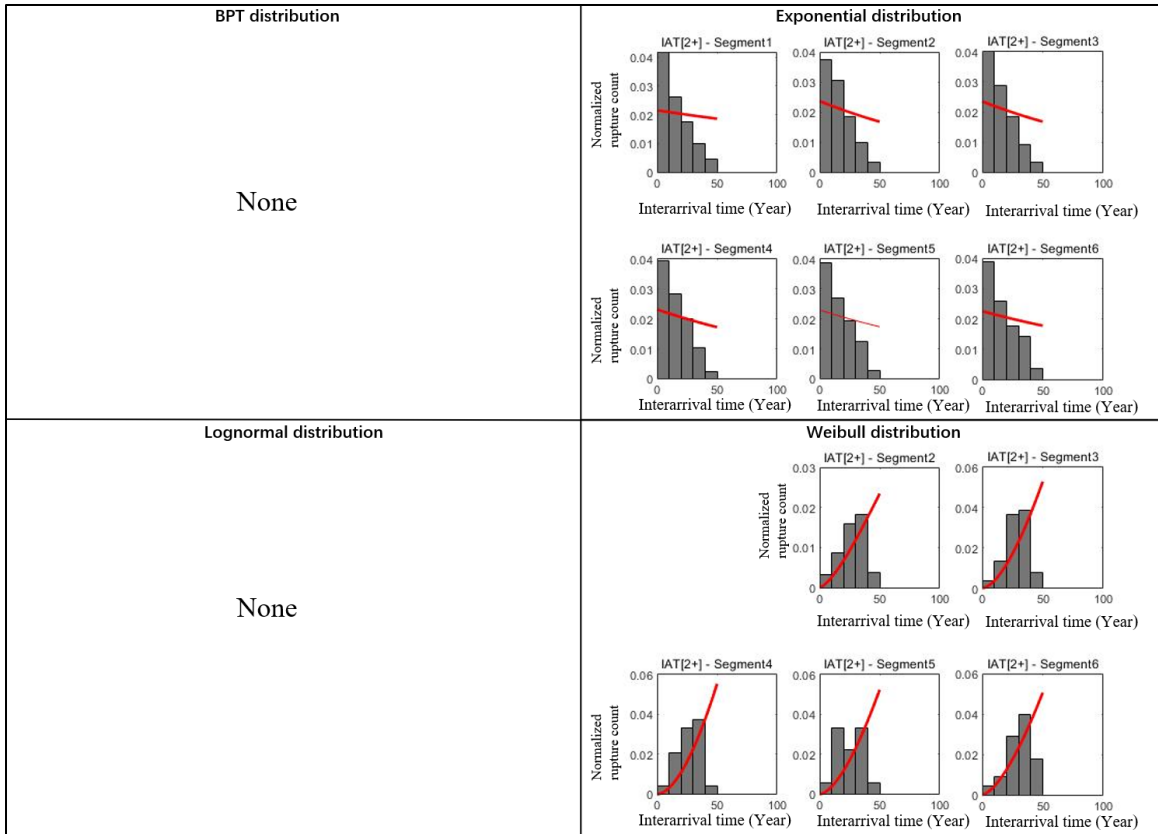


**Figure 3.6:** Nankai-Tonankai earthquake occurrence simulation of the 6-segment model results for the second occurrence in the next 50 years using the base catalogue. The elapsed time is reset to 0 after the first simulated occurrence, and the simulation only spans a duration of 50 years, which is much shorter than the averaged interarrival time for all segments. Therefore, the assumed distributions, as shown in red curves, are showing disagreement with the normalized histograms.

All models suggest that the probability of an earthquake occurring in the next 50 years is beyond 50%, which is calculated by dividing the total number of simulated earthquakes by the number of simulation iterations. Due to the constant hazard rate of the exponential distribution, this model generates the lowest 50-year rupture probability of 55% among all four distributions. The three time-dependent models account for the increasing hazard rate through time, thus generating 50-year rupture probabilities higher than 60%. Furthermore, the 50-year rupture probability simulated using the Weibull distribution is

lower than those simulated using the BPT and lognormal distributions. The discrepancy between rupture probabilities is mainly caused by the variation of hazard rate function at the middle-to-upper tail side of the time-dependent functions. In other words, the selection of interarrival time distribution function and segment model does affect the earthquake simulation results on the rupture probabilities of each segment. To determine the best representation of interarrival time distribution function to the temporal dependency between the segments, comparisons of regional seismicities, such as Gutenberg-Richter relation, are required; this will be discussed in Chapter 5.

Besides the discrepancy due to the variation of interarrival time distribution, the effect of segmentation pattern on earthquake simulation results is examined. In Table 3.6, the results simulated using the 3-segment model are summarized; to facilitate the comparison, the 6-segment model results are placed side by side. By looking at the mean of interarrival times of the simulated events, the 3-segment simulation results for the Nankai, Tonankai, and Tokai segments are similar to those of the 6-segment model. Moreover, variations in the rupture probability of each segment caused by different distributions are also conserved in the results of the 3-segment model. Noticeably, 50-year rupture probabilities decrease by about 8% compared with those estimated using the 6-segment model. The primary factor for the decreased probability is the exclusion of seismicity in the Hyuga-nada segment. Thus, the incorporation of the Hyuga-nada segment and the decision on segmentation patterns would significantly impact the seismicity estimation in the Kyushu region.

**Table 3.6:** Earthquake occurrence simulation results for the 3-segment model and the 6-segment model with  $\mu$ , number of simulated occurrences and 50-year rupture probability out of 20,000 simulations using the base catalogues.

Earthquake occurrence simulation results of base catalogues											
Probabilistic Distribution type	Segment number	3-segment				Probability of occurrence	6-segment				Probability of occurrence
		1st arrival		2nd arrival			1st arrival		2nd arrival		
		$\mu$	# of simulated earthquakes	$\mu$	# of simulated earthquakes		$\mu$	# of simulated earthquakes	$\mu$	# of simulated earthquakes	
<b>Weibull</b>	1	103	4945	27	36	0.52	85	264	0	0	0.60
	2	105	5511	27	44		103	5240	32	41	
	3	192	7260	27	101		103	4262	28	29	
	4						104	6046	27	67	
	5						104	5479	27	3	
	6						192	8006	27	84	
<b>BPT</b>	1	104	6265	44	1	0.61	103	1	0	0	0.68
	2	105	7068	47	1		103	6757	0	0	
	3	191	8444	45	2		104	5295	0	0	
	4						104	7514	43	2	
	5						104	6799	44	2	
	6						191	8854	47	2	
<b>Lognormal</b>	1	104	6004	30	1	0.60	0	0	0	0	0.68
	2	105	6868	38	1		103	6502	0	0	
	3	191	8544	45	1		104	5056	0	0	
	4						104	7464	39	3	
	5						104	6874	36	3	
	6						191	9021	0	0	
<b>Exponential</b>	1	99	5370	15	875	0.47	78	2408	18	129	0.56
	2	101	5587	16	937		99	5564	16	858	
	3	191	4631	16	590		99	5141	16	766	
	4						101	5797	17	917	
	5						101	5553	17	871	
	6						191	4773	16	42	

As aforementioned, three types of input catalogues are employed to examine the possible effect in earthquake simulation caused by the uncertainty within the historical records.



Based on the parameter estimation results, the 1096 catalogue generates a sequence of spatial and temporal correlation parameters similar to the base catalogue. For the 1605 catalogue, the model parameters have more than 10% fluctuation compared with those from the base catalogue. Therefore, the parameters with more significant variations are employed to simulate the earthquake occurrence for emphasizing any possible variations in earthquake simulation results. After processing, the mean interarrival times, the number of simulated ruptures and 50-year rupture probabilities for each segment are summarized in Table 3.7. It is observed that the mean interarrival time and rupture probability in the next 50 years of the simulated events only slightly vary, compared with the base catalogue. However, the most noticeable difference occurs in the number of simulated ruptures of the Nankai segment rupture. From the 3-segment model, the number of ruptures in segment 1, the Nankai segment (i.e. segments 2 and 3 in the 6-segment model) is increased by 400-800, while that of other segments is decreased by 1000-2000 out of the total 20000 simulations. Similarly, the same increasing and decreasing trends occur in the simulation results for the corresponding segments for the 6-segment model with even greater changes.

**Table 3.7:** Earthquake occurrence simulation results for the 3-segment model and the 6-segment model with  $\mu$ , number of sample occurrence and 50-year rupture probability out of 20,000 iterations using the 1605 catalogue.

Earthquake occurrence simulation results of 1605 catalogue											
Probabilistic Distribution type	Segment number	3-segment					6-segment				
		1st arrival		2nd arrival		Probability of occurrence	1st arrival		2nd arrival		Probability of occurrence
		$\mu$	# of simulated earthquakes	$\mu$	# of simulated earthquakes		$\mu$	# of simulated earthquakes	$\mu$	# of simulated earthquakes	
Weibull	1	103	5361	29	33	0.51	84	333	0	0	0.58
	2	105	4439	28	37		102	6084	28	93	
	3	193	6214	30	22		103	5640	32	44	
	4						105	4479	28	24	
	5						105	3975	27	18	
	6						193	6505	26	29	
BPT	1	104	6635	0	0	0.59	98	8	0	0	0.67
	2	106	5308	41	1		101	7875	40	3	
	3	192	7436	0	0		103	7340	0	0	
	4						106	5390	43	2	
	5						107	4806	0	0	
	6						191	8005	46	1	
Lognormal	1	104	6745	0	0	0.58	96	7	0	0	0.67
	2	106	5329	41	2		102	7745	36	5	
	3	192	7576	0	0		103	7166	0	0	
	4						107	5338	0	0	
	5						107	4712	0	0	
	6						191	8143	0	0	
Exponential	1	99	5588	16	951	0.47	78	2669	16	214	0.56
	2	101	5061	16	734		99	5768	16	1052	
	3	192	4016	16	460		99	5625	16	983	
	4						101	5086	17	752	
	5						101	4877	16	682	
	6						191	4248	16	516	

### 3.4 Conclusions of earthquake occurrence simulation results

The multivariate Bernoulli method is capable of generating simulation results with reliable mean interarrival times after considering both spatial and temporal correlations. However, the estimated probability of rupturing in the next 50 years is immensely

dependent on the division of segment pattern and assumed interarrival time distribution. More specifically, the simulated results using time-dependent and time-independent distribution tend to show larger discrepancies as the elapsed time becomes longer for the region. The employment of time-dependent distribution in seismic hazard modelling thus becomes essential. Input earthquake catalogues, which play a less dominant role in controlling the rupture probability and interarrival time of the simulated event, affect the rupture behaviour of certain segments but not the overall rupture behaviour. The difference within the occurrence catalogue has no significant effect on the overall rupture probability, but the rupture probability in the corresponding segments is changed drastically, depending on the variation within the catalogue. The selection of interarrival time distribution, segmentation pattern, and input catalogues thus become important in controlling the earthquake occurrence simulation results.

It is difficult to conclude which option best represents the realistic situation under the current stage. However, the ground motion estimates can be calculated by combining all types of output with the stochastic slip models. By combining every simulation result with stochastic slip models for ground motion estimation, 20,000 iterations were considered sufficient for calculating the representative average of the exceedance rate. The comparison of the predicted seismicity of the Nankai-Tonankai region with the historical seismicity would reveal the characteristics of earthquake occurrence simulation by utilizing different sets of input information. Therefore, the effect of selection of the type of segment models and interarrival time distributions on ground motion simulation is investigated in Chapter 5.

## Chapter 4

### 4 Stochastic slip model generation

The earthquake occurrence simulation results, as introduced in Chapter 3, are expressed as a combination of different rupture segments and automatically assume that the slip ruptures the entire segment and is homogeneously distributed over the fault plane.

However, the homogeneously distributed slip is not realistic in actual earthquakes due to heterogeneities of rocks and frictions within the fault plane. To complement the rupture information for the simulated earthquakes from the multivariate Bernoulli models, the heterogeneous slip models are developed for all potential rupture patterns. In this chapter, the stochastic slip modelling method is performed under realistic constraints. The main procedure is provided by focusing upon the Nankai-Tonankai Trough (Goda et al., 2020) in Section 2.3.3. Depending on the locations of individual segments, rupture scenarios with the estimated moment magnitudes and asperity zones are assigned accordingly to all rupture patterns within both 3-segment and 6-segment models. The stochastic slip models can then be repeatedly generated for each rupture scenario with different geometry and earthquake slip distribution.

To constrain the characteristics of generated slip distributions, the mean slip  $D_a$  is adopted as a targeted value for the average slip value, while the maximum slip  $D_m$  is set as the upper bound for very large slips. Besides, the Box-Cox parameter, correlation lengths in dip and strike directions, and the Hurst number are also source parameters that need to be computed according to the pre-assigned magnitude and asperity region. With the obtained spatial slip distribution parameters, the random field distribution is produced using the von Karman autocorrelation function (ACF) in the wavenumber domain, and the inverse Fourier transformed slip distribution in the spatial domain is adjusted and examined under realistic constraints (Goda et al., 2020). Ultimately, the averaged model for each scenario illustrates the most representative slip model of the rupture pattern, while detailed rupture information of individual slip models is employed to combine with the simulated ruptures and is then used for ground motion estimation.

## 4.1 Rupture scenarios for 3-segment and 6-segment models

The initial step of the setting rupture scenarios involves mapping the grid cells over the entire fault plane defined by the Central Disaster Management Council (CDMC2012) model. As discussed in Section 2.3.3, 5669 grids are considered with  $5 \text{ km} \times 5 \text{ km}$  grid size on a 2-D view over the whole rupture region. For each rupture scenario, the area of the acceptable slip model is first identified. Figure 4.1 illustrates the rupture pattern 1, the Nankai-segment rupture, of the 3-segment model with grid numbers along with strike and dip directions.

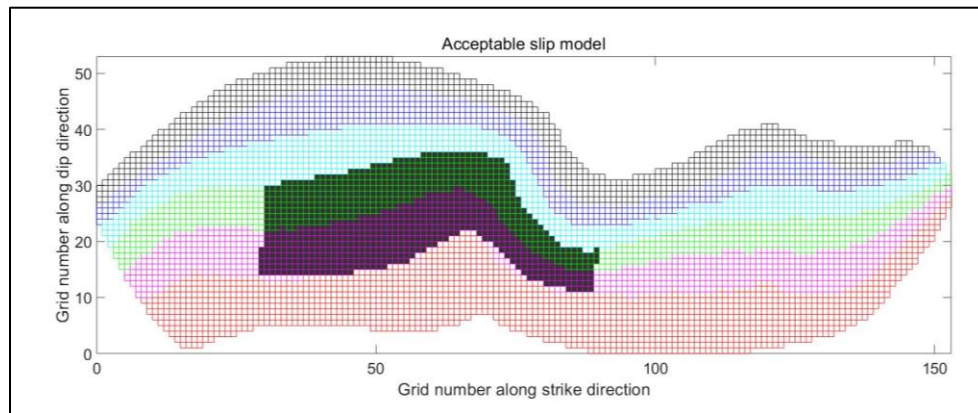


**Figure 4.1:** Acceptable area of slip model (shaded region) for the Nankai segment rupture case in the map view. The whole fault region is separated into multiple parts from the shallowest depth to the deepest, according to the CDMC2012 model. The red colour represents the area located between the top edge of the fault (5 km) and 10 km depth, while the purple, green, cyan and blue colours represent the areas with a gradual deepening interval of 5 km. The black region indicates the deepest part that lies between depths from 30 km to 55 km.

The moment magnitude range and the asperity zone area need to be defined first for each rupture scenario in two types of segment models. Due to the variation in segment division

pattern within each segment model (3 or 6), the segment length changes significantly, thus leading to the variation in the estimated moment magnitude. For each rupture scenario, the moment magnitude is estimated by using an empirical scaling relationship by Thingbaijam et al. (2017) according to the rupture area. The representative moment magnitude of the rupture scenario is taken as the mean value derived from the empirical equation:

$$M_w = (\log_{10}(A) + 3.292)/0.949 \quad (4.1),$$

where  $M_w$  is the moment magnitude, and  $A$  is the rupture area ( $\text{Km}^2$ ). The maximum and minimum of the approximated magnitude range are taken as the mean plus and minus one standard deviation. Furthermore, the historical moment magnitudes of rupture events are incorporated into the consideration of the potential magnitude range of the corresponding rupture scenario. The 1605 Nankai earthquake and the 1968 Hyuga-nada earthquake are the two earthquakes that have a moment magnitude lower than the approximated minimum magnitude from the corresponding rupture scenario. The former earthquake is considered as a tsunami earthquake that only ruptured the shallow region of the Nankai-Tonankai Trough. Therefore, only the 1968 Hyuga-nada with a moment magnitude of 7.5 is employed as the minimum of magnitude for the Hyuga-nada segment rupture.

Moreover, the probabilistic scaling relationship developed by Goda et al. (2016) is implemented for evaluating the seismic moment ( $M_0$ ) and moment magnitude calculation of the simulation results. According to the predefined fault segment length, rupture width ( $W$ ), fault length ( $L$ ), and mean slip ( $D_a$ ), the calculations are performed according to the following relationships:

$$M_0 = \mu WLD_a \quad (4.2),$$

$$M_w = \frac{2}{3}(\log_{10}(M_0) - 9.1) \quad (4.3),$$

where  $\mu$  is the rock rigidity and is typically assumed to be 40 GPa for the Nankai-Tonankai Trough (Goda et al., 2017; Kano et al., 2020).  $M_0$  is the seismic moment in Pascal.

As shown in Figure 4.2, for the 3-segment model, the rupture patterns 1 to 3 correspond to individual segment rupturing patterns, and patterns 4 and 5 are the two-segment rupture, pattern 6 is the whole-region rupture case. On the other hand, for the 6-segment model, rupture patterns 1 to 6 correspond to single-segment rupture, patterns 7-11 represent the two-segment rupture. Thus, there are  $\frac{(1+6) \times 6}{2} = 21$  combinations of rupture patterns obtained from the 6-segment model. The same classification procedure is applied to other combinations involving more than three segments until the whole-region rupture pattern is assigned as pattern 21. Due to the more detailed classification of segmentation in the 6-segment model, all rupture patterns in the 3-segment model can find an identical representation in the 6-segment model.

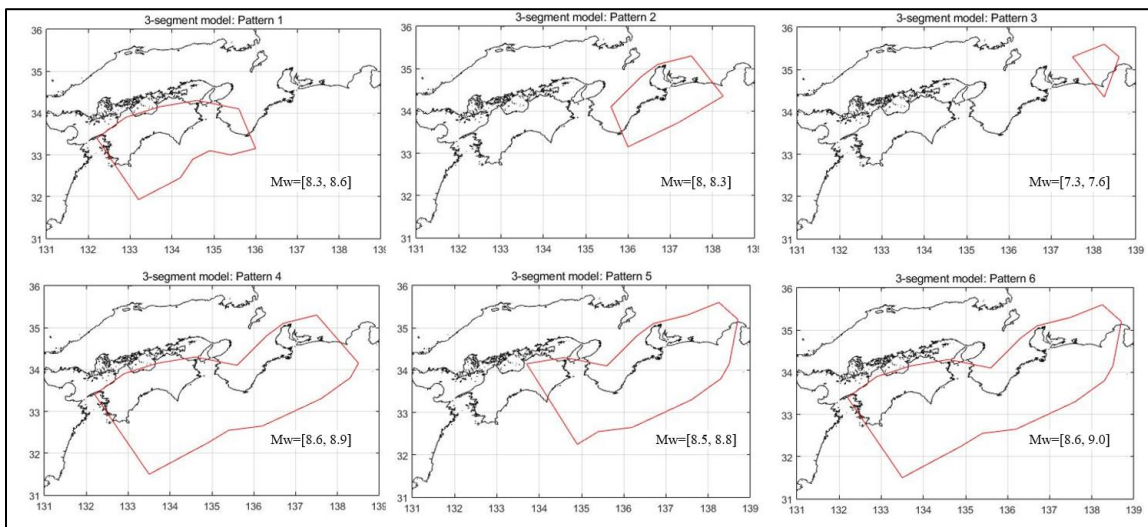


**Figure 4.2:** All six rupture scenarios corresponding to the 3-segment model. According to the rupture pattern and area derived from the referential CDMC2012 models, the moment magnitude can be estimated by using the empirical scaling law. In this figure, all possible rupture scenarios in the 3-segment model are plotted as combinations of different rupture segments. Patterns 1-3 represent the single-segment rupture that is restricted in the deeper region, while patterns 4-6 represent the synchronized multi-segment rupture that has a larger moment magnitude and can extend to top-edge depth of the fault plane.

From seismological research, the rupture area of less devastating earthquakes (e.g. 1946 Nankai earthquake) tends to occur in the deeper part (below 10-15 km isodepth contour) of the fault plane (Ando and Nakamura, 2013). The only exception is the 1605 Keicho earthquake, which was a tsunamigenic earthquake and ruptured at a depth shallower than 10 km (Garrett et al., 2016). In this thesis, rupture areas of less significant events (i.e. earthquakes with estimated representative magnitudes less than or equal to 8.6) are restricted to the deeper part between 5 km to 15 km of the fault plane, while the whole-region rupture is considered to extend to 1 km below the top-edge trench (5 km below the sea level) where depth is counted as 0 km of the fault plane. Figure 4.3 demonstrates the isodepth contours of 10 km (black line), 15 km (red line), and 20 km (blue line) depth below the sea level as obtained from the CDMC2012 models, respectively. Combining with the estimated magnitude range, Table 4.1 summarizes the specific information for generating stochastic slip models of each rupture scenario.

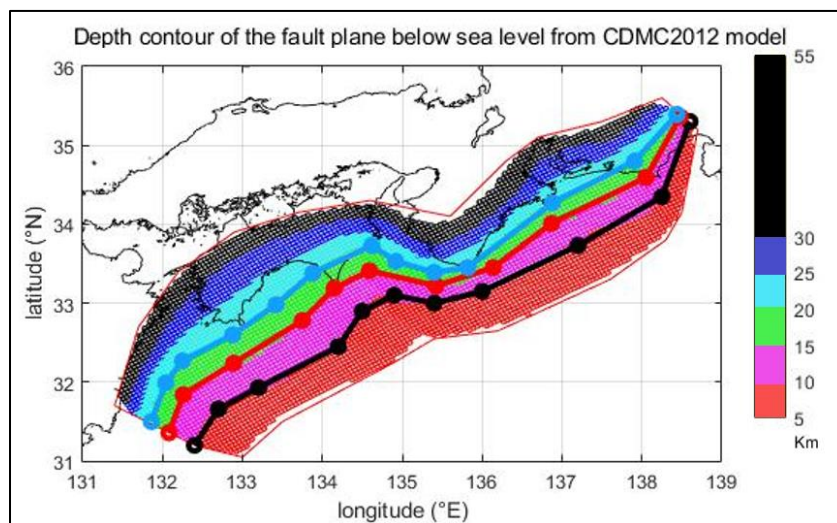


**Figure 4.3:** Isodepth contours of 10km, 15km and 20km of the Nankai-Tonankai Trough fault plane from the CDMC2012 model. The coloured region follows the depth distribution as in Figure 4.1 and indicates the region within the depth range from the sea level.



**Table 4.1:** Summary of estimated moment magnitude and asperity zone depth limit for rupture scenarios within the 3-segment and 6-segment models.

	Rupture pattern	Ruptured segments	Estimated moment magnitude		Asperity zone depth limit within fault plane (km)	
			Min	Max	Min	Max
<b>3-segment model</b>	1	1	8.3	8.6	5	15
	2	2	8	8.3	5	15
	3	3	7.3	7.6	5	15
	4	1+2	8.6	8.9	1	15
	5	2+3	8.5	8.8	1	15
	6	1+2+3	8.6	9	1	15
	Rupture pattern	Ruptured segments	Estimated moment magnitude		Asperity zone depth limit within fault plane (km)	
			Min	Max	Min	Max
<b>6-segment model</b>	1	1	7.5	8.2	5	15
	2	2	8	8.3	5	15
	3	3	7.8	8.1	5	15
	4	4	7.7	8	5	15
	5	5	7.7	8.1	5	15
	6	6	7.3	7.6	5	15
	7	1+2	8.3	8.6	5	15
	8	2+3	8.3	8.6	5	15
	9	3+4	8.1	8.4	5	15
	10	4+5	8	8.3	5	15
	11	5+6	7.9	8.2	5	15
	12	1+2+3	8.4	8.7	5	15
	13	2+3+4	8.4	8.7	5	15
	14	3+4+5	8.3	8.6	5	15
	15	4+5+6	8.1	8.4	5	15
	16	1+2+3+4	8.6	8.9	1	15
	17	2+3+4+5	8.6	8.9	1	15
	18	3+4+5+6	8.5	8.8	1	15
	19	1+2+3+4+5	8.7	9	1	15
	20	2+3+4+5+6	8.6	9	1	15
	21	1+2+3+4+5+6	8.7	9.1	1	15

## 4.2 Stochastic slip model simulations for Nankai-Tonankai Trough

For different rupture scenarios, the desired features of stochastic slip models can be achieved by employing expressly defined parameters, including 1) the stochastic synthesis parameters; 2) the target slip parameters; and 3) kinematic rupture parameters. In this thesis, the kinematic rupture parameters, rupture speed and rise time, are inconsequential to seismic hazard assessment (Chapter 5), since the calculation process of ground motion estimation only concerns about the synthesis and slip parameters. Therefore, kinematic rupture parameters are neglected in the discussion. As mentioned in Section 2.3.3, the slip distribution parameters and the stochastic synthesis parameters are the most important input parameters, including fault geometry length and width, maximum and average slip, Box-Cox power parameter, correlation length and width, and Hurst number. Among all parameters, the slip distribution parameters and the other stochastic synthesis parameters are evaluated according to the moment magnitude using empirical scaling relationships (Goda et al. (2016), from which the value of Hurst number and Box-Cox power parameter are also obtained.

The earthquake source parameters must account for uncertainties, and co-dependency resulted from the variability of stochastic synthesis parameters and slip parameters. Therefore, 500 slip models are generated for each scenario listed in Table 4.1. A representative averaged slip model is also plotted only for demonstrating and examine the characteristic slip distribution of the selected scenario. As the repeating simulation process is the same for both 3-segment and 6-segment models, the rupture pattern 1, i.e. Nankai-segment rupture, is selected for demonstrating the overall simulation procedures in the following.

To estimate the slip distribution and stochastic synthesis parameters, the moment magnitude of each slip model is first randomly estimated between the assigned minimum and maximum of 8.3 and 8.6, respectively, for the rupture pattern (Table 4.1). Furthermore, the uncertainties of constants derived by the regression are incorporated into individual parameters as the multivariate lognormally distributed random variables with linear correlations derived by Goda et al. (2016). Besides the input information that

dominates the overall geometry and slip distributions of stochastic slip models, the other constraints, such as asperity ratios, slip ratio of the major asperity area, and correlation length to fault length ratio, are used to control the minor characteristics of the generated slip models. The simulation only continues when all parameters fit into the empirically obtained constraints, or the simulation starts again from the random generation of the parameters.

With the estimated slip distribution and stochastic synthesis parameters, the size of the random field is first defined according to the fault length and width. Subsequently, the von Karman ACF is calculated as a function of the correlation length  $a_x$  and width  $a_z$ , Hurst number  $H_n$ , and wavenumber  $k$ , where  $k$  is evaluated by using  $a_x$ ,  $a_z$  and wavenumber in length and width directions as shown in Table 2.3. After incorporating the random phase matrix between 0 and  $2\pi$  into the power spectral density, the random slip distribution in the wavenumber domain is synthesized. The inverse Fourier transformation and Box-Cox transformation are then performed to convert the random slip distribution back to the spatial domain with the right-skewed distribution that is commonly observed during the actual earthquake. For each simulated slip distribution, the coordinates of the upper-left corner are assigned, and the generated 2D slip values are mapped onto the 3D fault plane. Furthermore, the taper functions are applied to the deep segments to allow the slip values to decrease gradually to their surrounding grids. The top edge area is also tapered when the slip stops before reaching the shallow area, thus the tapered slip does not extend to the ocean bottom. In the end, the standardized slip distribution is multiplied by the mean slip to obtain the realistic slip values over the fault plane.

After the generation of the stochastic slip model, the pre-set constraints are applied to confirm that the characteristic slip distribution possesses the desired features. The simulated slip distribution needs to have a rupture length longer than the minimum rupture length, which is half of the segment length for individual segment rupture and the length of the shortest segment for synchronized rupture. As discussed in Section 2.3.3, the constraints of the CDMC2012 model are also applied. More specifically, the ratio of large slip area to the total asperity region is constrained between 20% and 30%, and 60%

to 90% of the total slip falls within the major asperity zone. Furthermore, the stochastic slip distribution is only accepted when the target moment falls into the assigned magnitude range of each rupturing pattern to its corresponding magnitude scenario.

The models that satisfy all criteria are saved as heterogeneous slip models corresponding to the specific rupture scenario. For the Nankai-segment rupture case in the 3-segment model, Figure 4.4a illustrates the generated slip distribution variation in the 2D view (in terms of grid cells). The center of the main asperity zone located at the top edge of the 2D fault plane is characterized by a red colour, while the blue colour in the deeper part and around the asperity zone is generated due to the taper effect. The target moment magnitude, which is the same as the randomly generated magnitude since the start of the simulation, is compared with the moment magnitude of the simulated event. It can be observed that approximately 0.02 deviation in moment magnitude is produced and falls into the acceptable range of uncertainty. The slip distribution after Box-Cox transformation is illustrated in Figure 4.4b. The right-skewed slip distribution of a number of simulated slip values versus slip values is achieved, while the length, width and the average slip of the 2D slip distribution are indicated on the top of the figure. Finally, the slip distribution is mapped back to the fault plane, as shown in Figure 4.4c. The pink dash line characterizes the acceptable range of the slip model, and the simulated main asperity region lies within the acceptable area. As indicated at the top of the figure, the slip ratio of the simulated slip in the main asperity zone comprises 64% of the total slip value, and the maximum slip value reaches 20.8 m. Both results satisfy the constraints. Thus, the stochastic slip model is accepted as one successful case, and its parameters are stored in the slip model database of the Nankai-segment rupture in the 3-segment model.

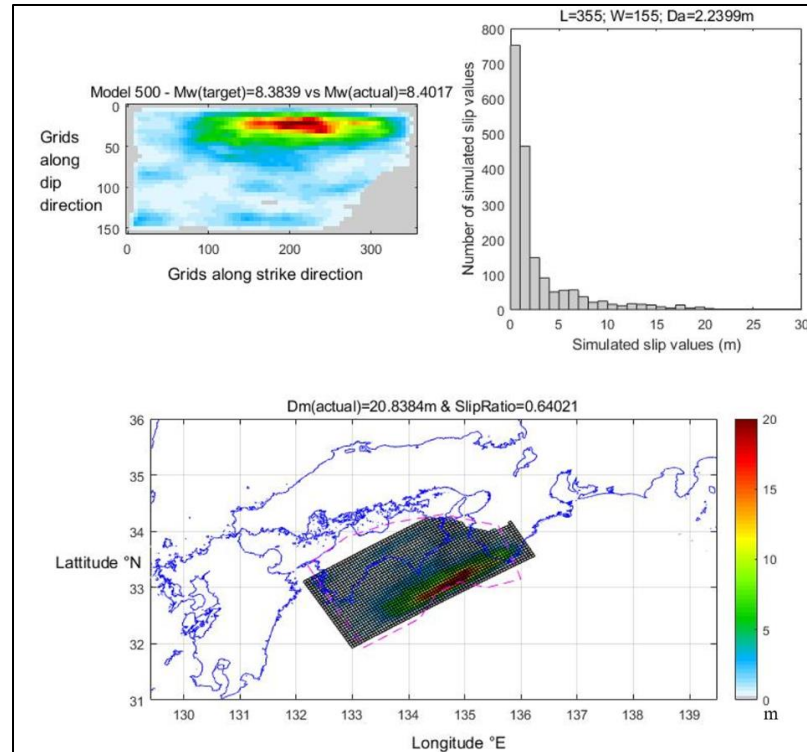


**Figure 4.4:** Example of a simulated slip model for the Nankai segment rupture case. a) Slip distribution in 2D view with the randomly generated moment magnitude (target moment magnitude) versus the approximated moment magnitude of the generated slip model (actual magnitude). b) Right-skewed slip distribution in the number of slips against slip values plot of the stochastic source model, while the fault geometry parameters and average slip are indicated on the top of the figure. c) Slip distribution mapped back to the fault plane view, where the pink dash line shows the area of the acceptable slip model.

Furthermore, the correlation between slip distribution parameters and stochastic synthesis parameters with moment magnitude is plotted to ensure no significant outlier is generated within 500 simulations following the global scaling model. For the Nankai segment rupture pattern, almost all parameters agree with the empirical scaling relations with the actual moment magnitude. As shown in Figure 4.5, each green point represents one simulated slip model, and most of the green points are located at the region between mean plus/minus one standard deviation of the scaling relationship. Both the Box-Cox

parameter and Hurst number are not dependent on the moment magnitude (Goda et al., 2016). Noticeably, the target moment magnitude shows an obvious positive correlation with the actual moment magnitude derived from simulated events. By shrinking the sampling range to a smaller interval, more data can be expected to be generated along the diagonal line, which characterizes the proportionality of simulated moment magnitude with the target moment magnitude. As all tests and results suggest the simulation has achieved the desired features under realistic constraints, all parameters of the 500 slip models are then saved for the rupture scenario.

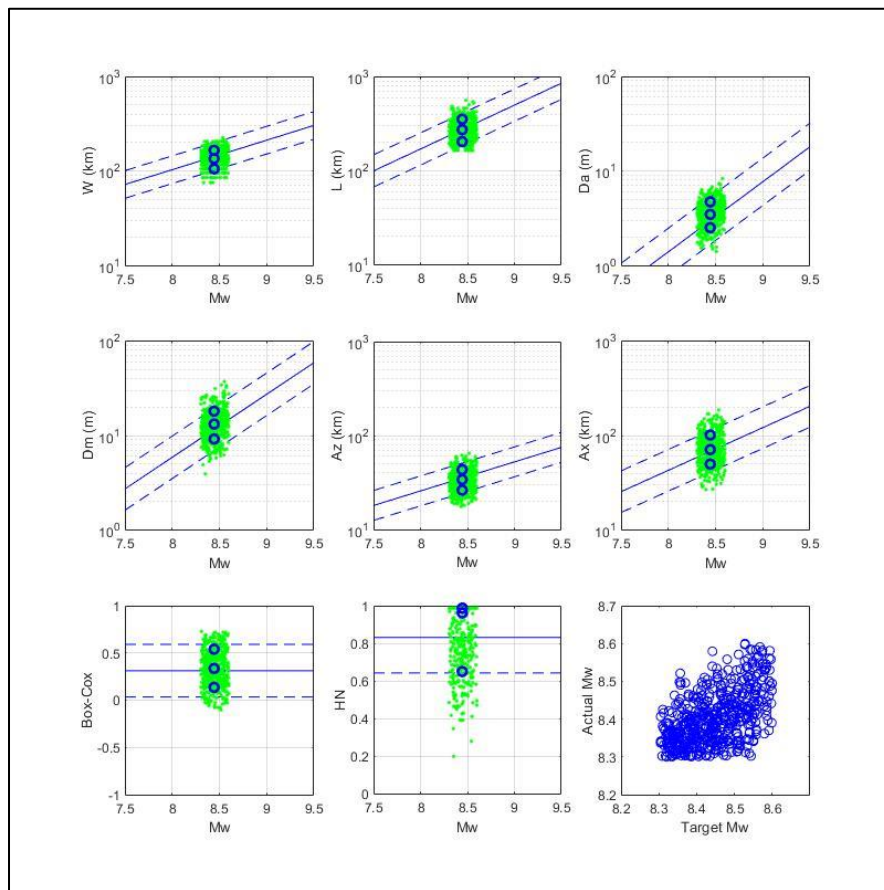


**Figure 4.5:** Correlation between slip distribution and stochastic synthesis parameters with moment magnitudes, and correlation between actual and target moment magnitude. Most slip distribution and stochastic synthesis parameters of generated slip models lie in the ranges estimated by using empirical scaling law, while Box-cox and Hurst numbers

are obtained from the empirical research and are not necessary to correlate with a moment magnitude. The target moment magnitude also shows a positive correlation with the actual moment magnitude of simulated slip models. By shrinking the moment magnitude range before simulation, more data are expected to locate on the diagonal where the target moment magnitude is the same as the actual moment magnitude. However, this will also cost more computational resources and time to achieve during processing.

After producing 500 slip models for the Nankai-segment rupture, the average of all slip models is calculated for the corresponding rupture pattern and is plotted in Figure 4.6. The main rupture area tends to be centered at the coastal area near Kii Peninsula and Kochi Prefecture, which belongs to the main rupture area of the Nankai segment. The central area typically has a slip around 10 m, while the slip decreases gradually to 0 m towards the surrounding areas. The same extent of slip is also observed in other rupture scenarios, as shown in Figure 4.7. Comparing with the CDMC2012 models which typically have a mean slip of 10m and a maximum slip between 50-60 m, the averaged stochastic slip models and the corresponding individual cases have a mean and a maximum slip twice to four times lower. The dominant factor of the discrepancy in slip values is due to the assigned moment magnitude range for the rupture pattern. According to equations 4.2 and 4.3, the decrease of 0.1 in moment magnitude leads to the decrease in the average slip by half, and thus reduces the possible generated maximum slip range while the fault geometry parameters remain constant. Therefore, the slip of all rupture scenarios is capable of capturing the slip distribution of the rupture pattern, as well as generating reasonable slip values according to the representative moment magnitude of the rupture scenario.

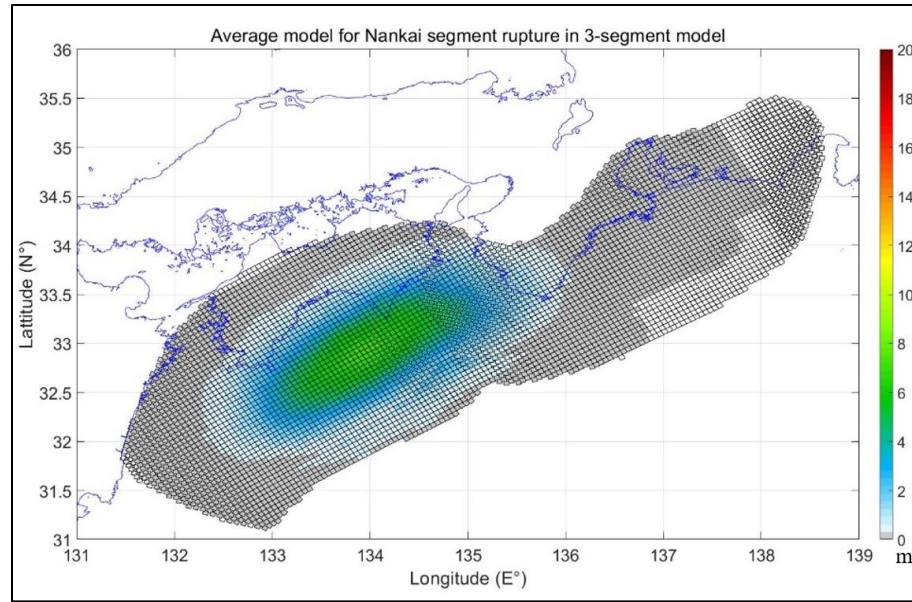


**Figure 4.6:** Average model of 500 simulation results for the Nankai-segment rupture pattern in the 3-segment model. The main asperity region is located off Shikoku, which agrees with the expected rupture area for Nankai-segment rupture and has a maximum averaged slip of about 6m.



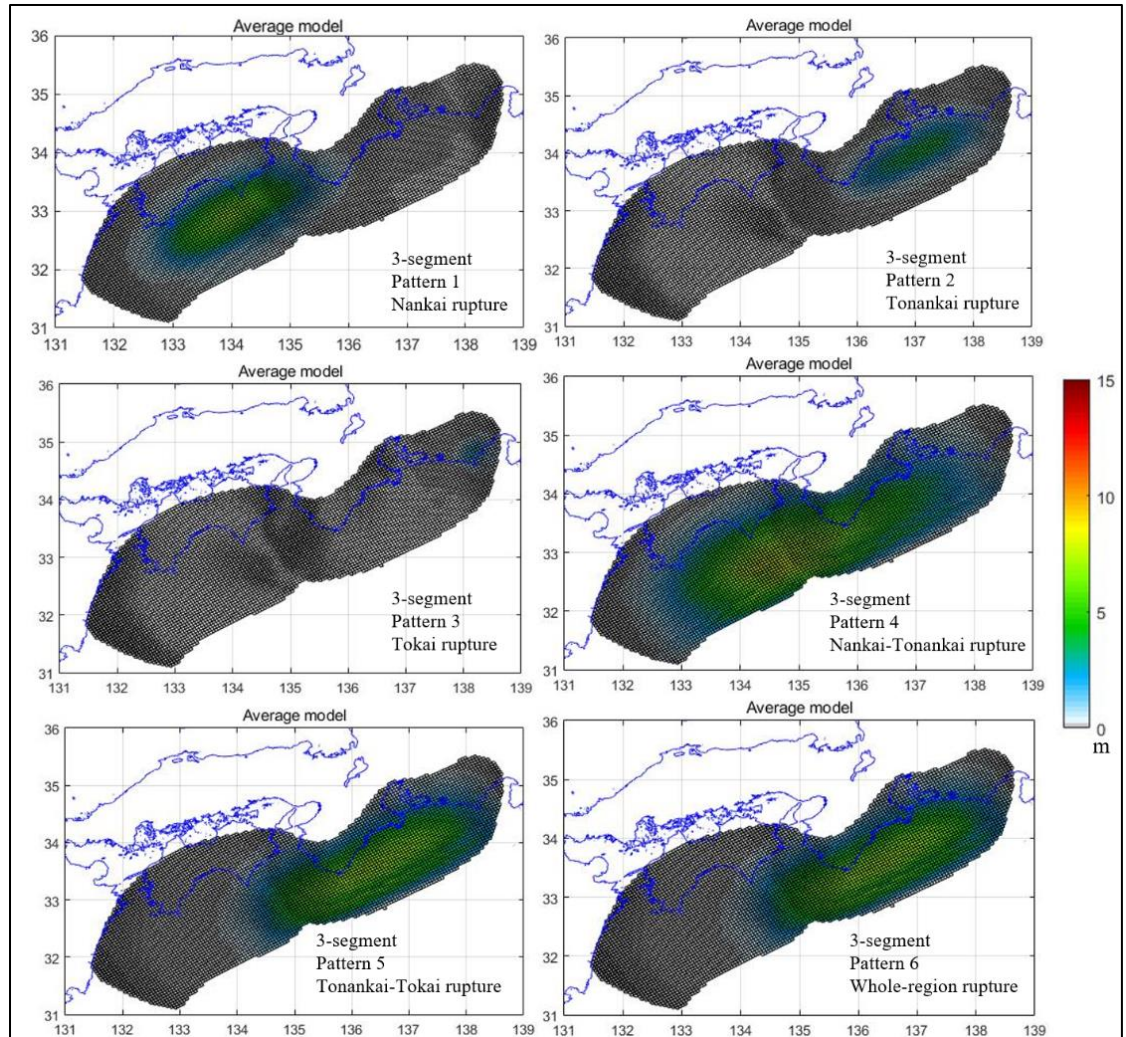


Figure 4.7: Average models of 500 stochastic slip models for the 1) Nankai segment, 2) Tonankai segment, 3) Tokai segment, 4) Nankai-Tonankai segment, 5) Tonankai-Tokai segment, and 6) Nankai-Tonankai-Tokai segment rupture patterns in the 3-segment model. The maximum slip of averaged models shows a positive correlation with the estimated rupture area, therefore, the range of possible moment magnitude for the corresponding rupture pattern. The distribution of main asperity zones for all averaged slip models also agrees with the expected rupture location. Thus, the individual slip model from the 500 slip models can characterize the random processes, while the iteratively sampled and averaged applications can reflect the overall seismic features of the corresponding rupture pattern.

### 4.3 Conclusions of stochastic slip models

The stochastic source modelling procedures are carried out for all scenarios of both 3-segment and 6-segment models. For each rupture scenario, 500 individual slip models are produced. Depending on the approximated rupture depth limit and the range of moment magnitude, the averaged slip models demonstrate the different extent of slip values as shown in Figure 4.7. For the 3-segment model, the averaged stochastic slip models produced for rupture scenarios with moment magnitudes less than 8.6 are located under a depth of 5 km within the fault plane as for patterns 1-3. The rupture scenarios with higher estimated magnitude ranges, corresponding to rupture patterns 4-6, tend to extend the rupture area to the area near the top edge of the fault plane. Moreover, the averaged slip values also correlate with the pre-assigned magnitude ranges. For instance, the Tokai region rupture, rupture pattern 3, has the least average slip values of 2-3m due to its much lower potential moment magnitude range ( $M_w 7.3-7.6$ ) comparing with other rupture scenarios. The whole-region rupture pattern 6, as spanning the areas containing Nankai, Tonankai and Tokai segments, has the largest potential moment magnitude range ( $M_w 8.6-9.0$ ) thus the average slip reaches up to 10m. The averaged slip models for rupture scenarios in 6-segment models, as attached in Appendix B, also show the same correlation with the assigned magnitude range and rupture depth.

As all average slip models are examined to have a realistic distribution and locate in the proper region the stochastic slip models are ready to combine with the earthquake simulation result as corresponding rupture information are produced for all rupture scenarios, including slip distributions, hypocenter locations, rupture area, and moment magnitudes. The conditional probability distribution of different seismic metrics can, therefore, be constructed for each rupture scenario. Furthermore, conditional probability can be combined according to the total probability theorem. This allows the exceedance probability to be captured as a sum of individual simulation and to link with the possible damage in seismic hazard estimation. Ultimately, the 20000 simulations from the multivariate-stochastic hybrid earthquake occurrence simulation can be directly linked with ground motion calculation, which employs empirical ground motion models of

Japanese subduction earthquakes by using the moment magnitude and source-to-site distances of individual earthquake simulation results.

## Chapter 5

### 5 Ground motion estimation using multivariate-stochastic hybrid earthquake occurrence modelling method for Nankai-Tonankai Trough

The multivariate-stochastic hybrid earthquake occurrence modelling method from Chapters 3 and 4 produces multi-segmented earthquake occurrences for near-future Nankai-Tonankai megathrust earthquakes. In each simulation, the rupture condition is represented as synchronized or individual-segment rupture along the fault (Chapter 3). All simulated ruptures are then linked with heterogeneous slip models generated using the stochastic method (Chapter 4) to include realistic slip information for all rupture scenarios. To examine the validity of the hybrid earthquake occurrence modelling method, the predicted earthquake occurrences and rupture models are employed in estimating ground motion in Japan. To avoid the unwarranted extrapolation of the empirical ground motion models (GMMs) in the large magnitude range, the selection of GMMs from the literature should consider the inclusion of the Mw9.0 seismic records. For this purpose, a GMM developed after incorporating the seismic records of the 2011 Mw9.0 Tohoku earthquake (Morikawa and Fujiwara, 2013) is integrated with the hybrid occurrence model. In this thesis, the conditional hazard map is generated concentrating in the estimation of crustal earthquakes in the shallow region. In North America, the hazard map is usually plotted as exceeding different PGV values at a certain probability threshold. However, the hazard map can be plotted as different probabilities exceeding certain PGVs in Japan, which is also the method of demonstration used in this thesis.

As 20,000 simulations are conducted with a duration of 50 years according to earthquake occurrence modelling, the ground motions are repeatedly calculated for estimating the probability of exceeding a certain threshold. Referring to the modified Mercalli scales, the level of PGV levels is setting for characterizing different intensities of potential damage and shaking at a site. By mapping the exceedance probabilities at all sites throughout Japan, a visual representation of the probability of ground motion exceedance facilitates the visual interpretation of potentially risky areas due to future events. Thus, the spatial distribution of exceedance probability aims to reflect the potential of an area to

experience different levels of seismic hazards. Furthermore, by setting the exceedance probability calculated using BPT-distribution simulation results of the base catalogue of 6-segment model as the standard result. The deviations in exceedance probability calculated from different rupture simulation results using other types of settings help to investigate the variations resulted from employing different interarrival time distributions, segmentation models, and earthquake occurrence catalogues.

## 5.1 Empirical ground motion model in Japan

When an earthquake of a certain size occurs, the intensity of ground shaking at locations can be estimated using empirical relationships that describe the ground motion scaling and attenuation as a function of earthquake magnitude, site-to-source distance, and local site condition. A GMM can be expressed in a general form:

$$\log_{10}Y = f_{\text{source}} + f_{\text{path}} + f_{\text{site}} + \sigma\epsilon \quad (5.1),$$

while this can be expanded to a more detailed expression:

$$\log_{10}Y = a + bM + c \ln R + dR + f_{\text{site}} + f_{\text{fm}} + \sigma\epsilon \quad (5.2),$$

where  $Y$  is the ground motion parameter, such as peak ground peak acceleration (PGA), peak ground velocity (PGV), and spectral acceleration (SA),  $M$  is the earthquake moment magnitude,  $R$  is the site-to-source distance,  $f_{\text{site}}$  is the site condition term,  $f_{\text{fm}}$  is the faulting mechanism term, and  $\sigma\epsilon$  is the prediction error term.

Ground motion parameters reflect different characteristics of the ground motion. PGA is the maximum absolute amplitude of the acceleration recorded during an earthquake at a location. In earthquake engineering, PGA is commonly employed in studying the extent of shaking of stiff structures. The spectral acceleration, SA, also describes the maximum acceleration experienced by a building during an earthquake. The structural resonance effect is captured in SA after accounting for the natural vibration period and the damping ratio. Thus, SA plays an important role in estimating a dynamic load on the structure and

carrying out probabilistic seismic hazard assessment. In this thesis, the potential damage caused by future Nankai-Tonankai earthquakes is of interest. PGV, which is the maximum absolute velocity during an earthquake and is correlated well with seismic damage (Goda and De Risi, 2018), is therefore adopted as the main ground motion parameter.

In Japan, the Mw 9 Tohoku earthquake that occurred on March 11<sup>th</sup>, 2011, enriched strong motion data for very large magnitude ranges. Subsequently, various updates of the empirical GMMs were performed by incorporating strong ground data from the 2011 Tohoku earthquake and their aftershocks (Morikawa and Fujiwara, 2013; Ghofrani and Atkinson, 2014; Zhao et al., 2016; Abrahamson et al., 2016). The GMM developed by Morikawa and Fujiwara (2013), which utilizes strong-motion records of events with Mw greater than 5.5 and closest rupture distances less than 200 km, is considered as an adequate GMM in evaluating ground motions caused by the Nankai-Tonankai megathrust earthquakes in this thesis. The Morikawa-Fujiwara model was developed by adding strong-motion records at the end of 2011 to the strong motion database of Kanno et al. (2006). Morikawa and Fujiwara (2013) presented the comparison of PGV estimations of their GMMs with the earlier version of GMMs from Si and Morikawa (1999) and Kanno et al. (2006), which is shown in Figure 5.1.

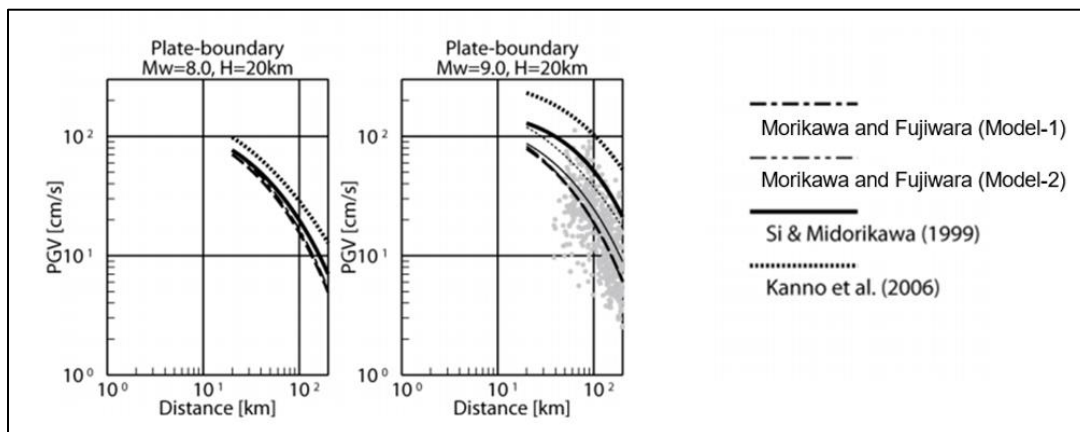


**Figure 5.1:** Comparison between PGV estimated from GMMs of plate-boundary earthquakes before and after taking account of the 2011 Mw9.0 Tohoku earthquake

(figure adopted from Morikawa and Fujiwara,2013).  $H$  is the focal depth, and  $M_w$  is the moment magnitude assigned for the earthquake. The grey dots are PGV data obtained during the 2011  $M_w$ 9.0 Tohoku earthquake. In the right panel, an additional thin dash line in the middle of the five curves characterizing the PGV calculated using Kanno et al. (2006)'s GMM under  $M_w$  8.2 demonstrates the effect of the magnitude saturation, that the ground motion is overestimated and is similar to the data collected in an  $M_w$ 9.0 event.

While the site-to-source distance remains unchanged, the GMM of Kanno et al. (2006) is stretched to estimate the ground motion in an  $M_w$ 9.0 earthquake. The PGV values are then observed much higher than the strong motion data collected during the 2011 Tohoku earthquake, shown as grey dots in the right panel. Two versions of updated GMM in Morikawa and Fujiwara (2013), which treats the magnitude term quadratically (model 1) or linearly (model 2) for expressing the magnitude saturation, are also plotted on the same graph. In this thesis, both models are treated equally, and model 1 is intuitively employed for calculating the ground motion parameters. According to the empirical relationships, the logarithm of ground motion parameter  $\log_{10}Y$  is directly related to the moment magnitude  $M$  as shown in Equation 5.1. However, the magnitude saturation effect is observed at a very high magnitude due to the delay of seismic wave arrivals resulted from the large rupture area in practical situations. To demonstrate the uncertainties resulted from extrapolation for GMMs, the estimated PGV for an  $M_w$ 8.2 event is also plotted on the same graph as the thin dash line. The result shows the magnitude saturation effect at high magnitude (i.e.  $M_w$ 8.2) can lead to an overestimation of the ground motion than the actually observed ground motion records. Thus, the extrapolation of a GMM to a large magnitude can potentially generate significant bias. The increasing rate of PGV at larger magnitudes thus becomes slower. Furthermore, overestimation is also applicable to other ground motion parameters, such as SA, PGA, and JMA seismic intensity. As a major update, the incorporation of the seismic recordings from the Tohoku earthquake by adopting Morikawa and Fujiwara's (2013) GMM eliminates the possible overestimation due to the magnitude saturation effect in

comparison with the older versions. Therefore, the uncertainty related to the saturation at very large magnitudes (e.g. Mw9.0) is significantly reduced within the updated GMM.

The coefficients for the Morikawa-Fujiwara GMM were obtained for three types of earthquakes: crustal, subduction plate-boundary, and subduction intra-plate. In regression, greater weights were assigned to ground motion records at short distances, thus emphasizing the near-source data. The derived functional form of this model is expressed as:

$$\log_{10}(\text{GMP}) = a * (\min(\text{Mw}, \text{Mw}_{01}) - \text{Mw}_1)^2 + b * x + c - \log_{10}(x + d * 10^{e * \min(\text{Mw}, \text{Mw}_{01})}) \pm \sigma \quad (5.3),$$

where GMP corresponds to ground motion parameters PGV, PGA or SA; constants a, b, c, d, and e are the coefficients obtained from regression; x is the shortest rupture distance;  $\text{Mw}_{01}$  is the saturation moment magnitude;  $\text{Mw}_1$  is a constant; and  $\sigma$  is the standard deviation. Furthermore, additional correction terms are added to account for the effect of amplification due to shallow soft soil and deep sedimentary layers. In the end, this model is expressed in its fully functional form as follows:

$$\log_{10}(\text{GMP}) = -0.0325(\min(\text{Mw}, 8.2) - 16)^2 - 0.002408x + 5.6026 - \log_{10}(x + 0.002266 * 10^{0.5 * \min(\text{Mw}, 8.2)}) + 0.2317 * \log_{10}\left(\frac{\max(60, D1400)}{250}\right) - 0.5546 * \log_{10}\left(\frac{\min(1100, \text{Vs30})}{350}\right) + 0.262807(\epsilon) \quad (5.4),$$

where GMP is PGV, PGA, or SA; D1400 and Vs30 are the site parameters;  $\epsilon$  is the multivariate normally distributed error term with linear correlation derived using the average spatial correlation model (Goda and Atkinson, 2010). For the Nankai-Tonankai case, the representative shear-wave velocity in the uppermost 30 m (Vs30) is taken as 400 m/s, which is adequate for water-rich sediments in Japan (Schumann et al., 2014) and corresponding to the relatively stiff soil condition. The depth to the shear-wave velocity of 1400 m/s, D1400, is set to 250 m, according to Morikawa and Fujiwara (2013).



## 5.2 The application of earthquake simulations and stochastic slip models to ground motion estimation

For calculating the ground motions using Morikawa-Fujiwara GMM, the locations of the sites are set with an equal interval of 0.1 degrees in longitude and latitude, which is about 11.1 km in the distance, throughout Japan. According to the sub-fault planes defined in the stochastic slip models, the distance from all sites to all sub-faults can be evaluated. Furthermore, the internal site-to-site distance and spatial correlations between all sites are estimated to describe the correlated seismic effects. The shortest rupture distance can then be calculated in 3D with sufficient accuracy via the Pythagorean theorem using the surficial distance and total depth of the sub-fault. After storing all site to sub-fault distances, the moment magnitude and hypocenter location of each simulated earthquake occurrence also need to be defined for ground motion calculation. The earthquake occurrences, as generated from the 20,000 simulations, are individually assigned with a randomly chosen stochastic slip model from the 500 slip models generated for the same rupture scenario. Under the total probability theorem, the conditional probability estimated from mutually exclusive rupture patterns can be combined. The probability of exceeding certain levels of PGV at each site is, therefore, calculated using the assigned rupture information by dividing the number of cases that exceed a certain ground motion threshold over 50 years by the total simulation number 20000. A generalized procedure of carrying out ground motion estimation from earthquake simulation is illustrated as a flowchart in Figure 5.2.

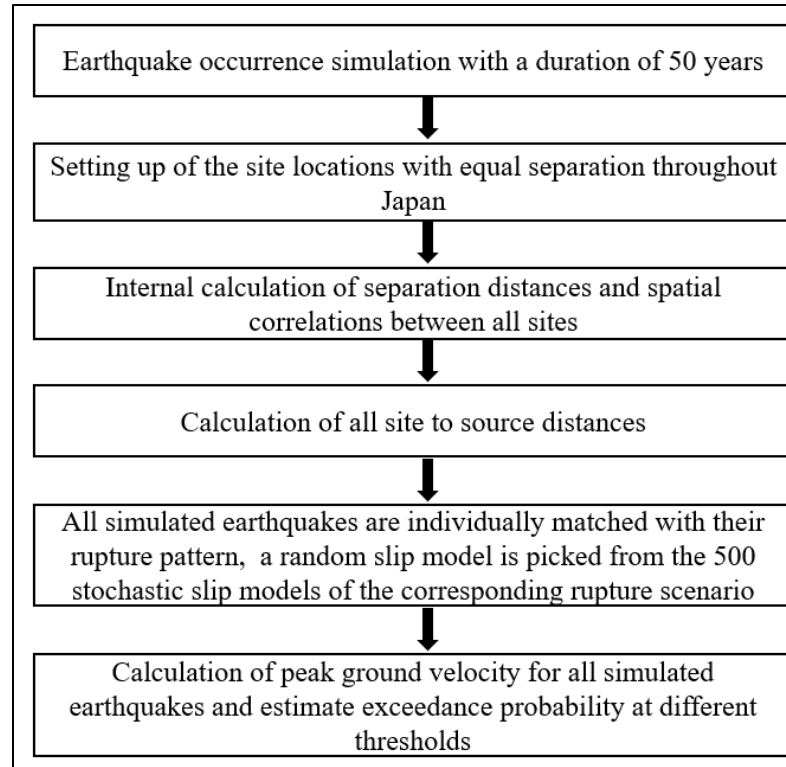


**Figure 5.2:** Flowchart of ground motion simulation using simulated earthquakes with stochastic slip models. The site locations are first set with equal separation distance throughout Japan, then internal site-to-site distance and spatial correlations between all sites can be estimated. Furthermore, all site-to-source distances are also estimated using the 3-D grid setting in the fault plane from the CDMC2012 model. After running the multivariate Bernoulli method, simulated earthquake occurrences are individually matched with a randomly picked slip model from the 500 models of the corresponding rupture pattern. In the end, ground motion parameters are estimated, and exceedance probability at all sites are calculated by counting the number of exceeding certain threshold at each site and divide by the total number of simulated earthquakes.

Furthermore, the annual rate of exceedance at a high magnitude of simulated earthquake occurrence is compared with the frequency-magnitude relation derived using a national earthquake catalogue maintained by the JMA. For demonstration, the exceedance rate of earthquake occurrence simulated using the 6-segment model is plotted as red squares in

Figure 5.3. As interpreted from the plot, the annual number of earthquakes exceeding Mw7.5 is 0.15 for the BPT, exponential and lognormal distributions, and 0.12 for the Weibull distribution. The discrepancy between annual exceeding rates by employing different distributions is predominantly controlled by the hazard rate of specific distribution, which is resulted from the difference between the number of simulated ruptures using different distributions as shown in Table 3.6. As compared with the magnitude-frequency relation of the JMA catalogue shown in the blue circles, the deviation from simulated events to the realistic earthquakes is large at Mw7.5 with about 14%-16% of annual occurrence rate lower but still likely falls in the range of uncertainty of the empirical frequency-magnitude relation. It can be observed that the annual exceedance rate tends to show better agreement at a magnitude higher than Mw8. The main reason is that the rupture scenarios within both segment models commonly have a representative magnitude equal to or greater than Mw8. Thus, the annual exceedance rate of simulated earthquakes at the moment magnitude range between 7.5 and 8.0 shows less agreement with the frequency-magnitude relation derived from the JMA catalogue. Furthermore, the classification of events within the JMA catalogue is not carried, and in-slab events still remain in the catalogue. Thus, the major uncertainty lies in both the simulation and data sides. The same phenomenon is also observed for the frequency-magnitude relation of other simulation results, while the annual exceedance rate between 7.5 and 8.0 can be even lower, corresponding to the variation in total rupture probability as shown in Table 3.6 and Table 3.7.

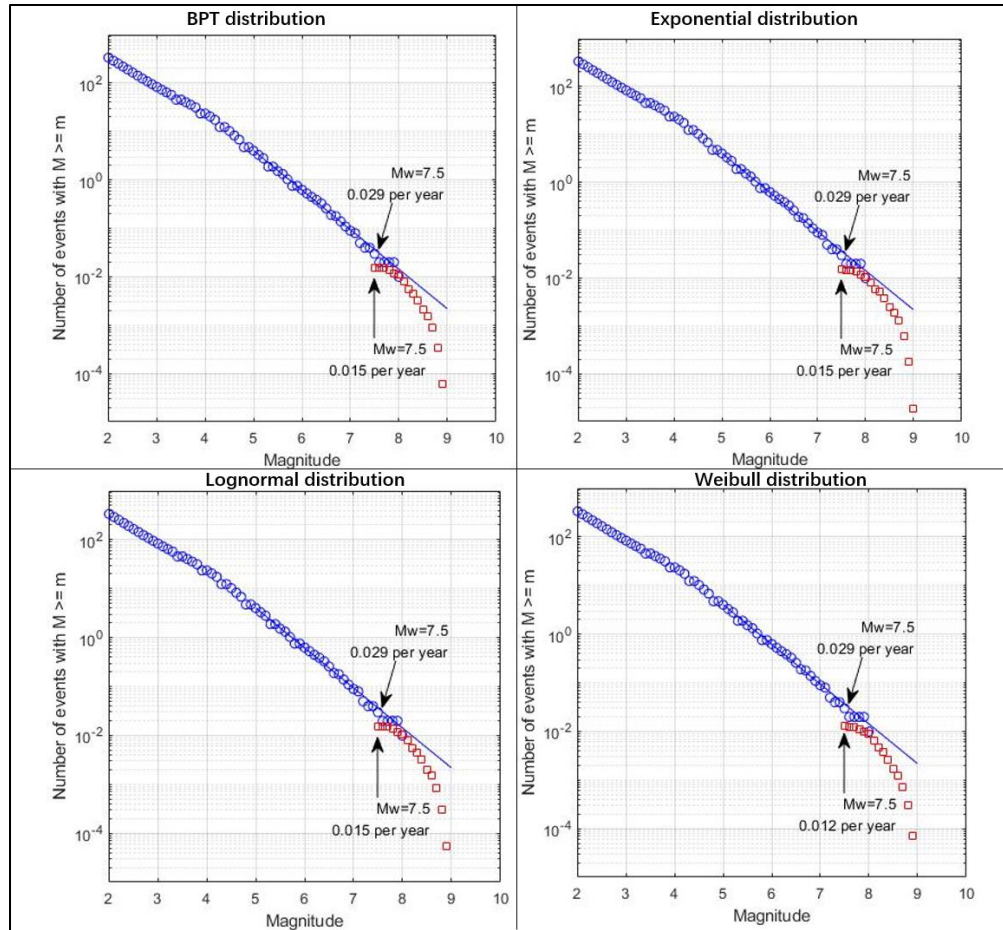


**Figure 5.3:** Magnitude-frequency relation of earthquake simulation derived from the 6-segment model using the base catalogue. The blue circles represent the national earthquake catalogue maintained by the Japan Meteorological Agency (JMA) and the red squares are the magnitude-frequency relation of the simulated earthquakes. At Mw7.5, all simulated earthquakes are having about 14%-16% of annual occurrence rate lower than that estimated from the JMA catalogue. At a higher moment magnitude (greater than Mw8.0), the magnitude-frequency relation tends to show better agreement. The dominant reasons are: 1) the rupture scenarios within both segment models commonly have a representative magnitude equal to or greater than Mw8 when setting up the simulation, so a smaller number of events with smaller moment magnitude are generated. 2) in-slab events still remain in the JMA catalogue while the simulation result focuses on the megathrust earthquakes only.

### 5.3 Nankai-Tonankai Trough ground motion estimation

With the other constant parameters obtained from the Morikawa-Fujiwara GMM, PGV is calculated and utilized for estimating the probability of PGV exceeding 16 cm/s, 31 cm/s, 60 cm/s, and 116cm/s, respectively. Based on Modified Mercalli intensity (Wood and Neumann, 1931), a building with PGV exceeding the above thresholds tends to experience moderate (VII), moderate/heavy (VIII), heavy (IX), and very heavy (X+) shaking and damage, respectively. For each site, the ground motions of all simulated earthquakes are calculated and compared with the four thresholds. After counting the number of PGV exceeding each of the thresholds, the probability of exceeding is able to be computed and plotted at all sites. Figure 5.4 illustrates the 6-segment simulation results with the same scalebar using the BPT interarrival time distribution and base catalogue in Table 3.6. As shown in the map, the high probability of exceeding all PGV levels tends to concentrate at the Nankai-Tonankai region, while the probability of exceedance decreases when the threshold increases. Compared with the historical seismicity dominant in Nankai-Tonankai segments, the regional distribution with high probability overlaps approximately the same area of the historically damaged region. The maximum probability of PGV exceeding 16 cm/s in the next 50 years reaches 53% at Tokai region, 50% at Tonankai region, 40% at Nankai region and 20% at Hyuga-nada segment, while the simulated ground motion exceeding 116 cm/s has a probability of 5% only and mainly concentrates at Nankai-Tonankai segments. The results indicate a large potential that all sites near coastal regions would at least undergo moderate damage, while a much lower probability that severe damage would occur at sites in Nankai and Tonankai coastal areas in the next 50 years. Furthermore, the distribution of areas with different levels of exceedance probability also agrees with the seismic hazard map in Japan Seismic Hazard Information (J-SHIS). Thus, the exceedance probability estimated from the 6-segment model using based catalogue and BPT distribution is considered effective and used as the standard when comparing with exceedance probability calculated using other simulation results.

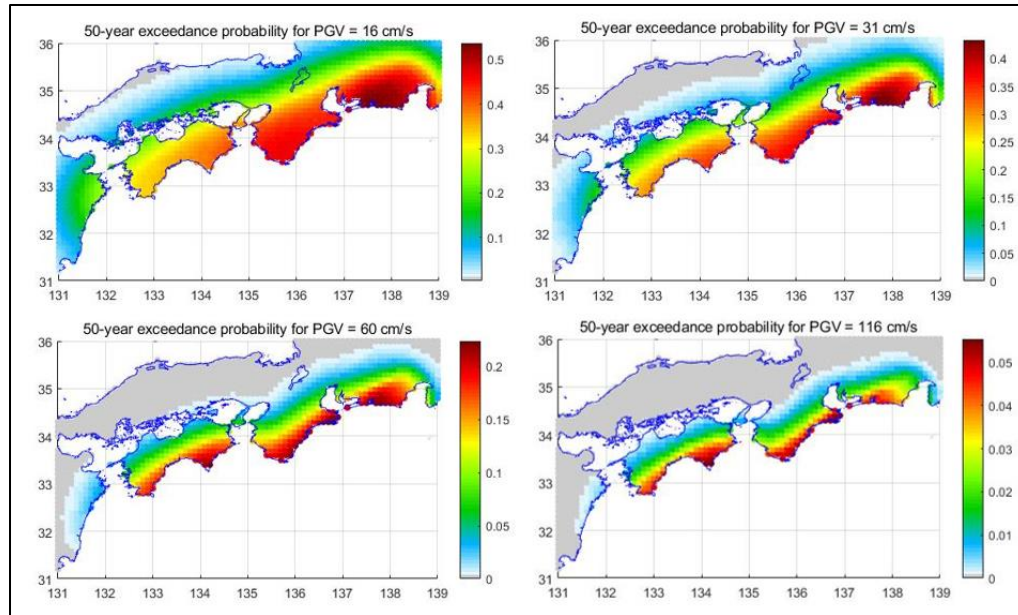


**Figure 5.4:** Probability of exceeding different levels of PGVs for occurrence modelling results of the 6-segment model based on the base catalogue with the BPT inter-arrival time distribution. The regions of high exceedance probability tend to locate in the coastal area near Nankai, Tonankai and Tokai segments, which agrees with the historical seismicity. The exceedance probability also decreases as the PGV threshold rises from 40%-50% for  $PGV > 16 \text{ cm/s}$  to a 4%-6% chance of  $PGV > 116 \text{ cm/s}$ .

To provide better comparisons, all plots are adjusted with the same scale in Figure 5.5. The map of probability of exceeding 16 cm/s and 31 cm/s shows relatively high to the moderate potential that Nankai-Tonankai Trough will cause seismic hazard centering at the coastal area around the Kii Peninsula and Shikoku. Most importantly, almost the entire southwest Japan has above 10% chance to experience very strong shaking and moderate damage in the next 50 years, according to the model. The probabilities of exceeding 60 cm/s are moderate, and 116 cm/s are relatively low, as shown in the lower panels of Figure 5.5 and Figure 5.4. In general, the large difference can be explained by a far higher occurrence rate of a single rupture pattern than a synchronized rupture. The Tokai region, as having a long elapsed time since the last rupture, is considered to have a large potential to rupture again by the time-dependent interarrival distributions. Thus, the estimated exceedance

probability at the Tokai region is higher than the Hyuga-nada segment, and similar to Nankai and Tonankai segments.

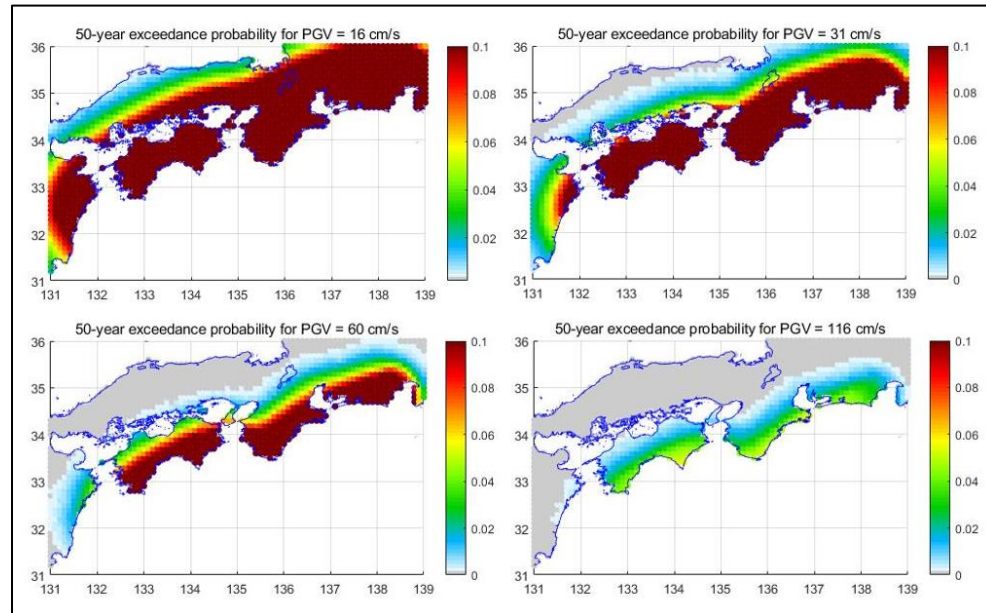


**Figure 5.5:** Probability of exceeding the different levels of PGVs with the same colour scale for occurrence modelling results of the 6-segment model based on the base catalogue with the BPT interarrival time distribution. Southwest Japan is predicted to have an above 10% chance of  $PGV > 16 \text{ cm/s}$  and to experience very strong shaking and moderate damage, while there is a much lower probability and a smaller area near Nankai, Tonankai and Tokai segments would experience  $PGV > 116 \text{ cm/s}$  in the next 50 years.

Moreover, the earthquake occurrences simulated by assuming different interarrival time distributions also show discrepancies in the regional distribution of a high probability of exceedance of the PGV thresholds. Because the lognormal distribution produces approximately the same rupture occurrence as the BPT distribution, the differences of exceedance probability from the BPT distribution to Weibull and exponential distribution results are plotted in Figure 5.6 and Figure 5.7, respectively. Due to both excess and

deficiency can occur when comparing two simulation results, large uncertainties can be induced when computing the differences in percentages. The dominant reason is that the exceedance probabilities can be extremely small in certain site locations but having a very large discrepancy between the two simulation results. Thus, the differences in exceedance probability are directly illustrated to demonstrate the effect of selection in probabilistic distribution, segmentation model and historical earthquake catalogue. For the Weibull distribution, the geographical distribution of the high-probability region agrees with that generated using the BPT distribution. However, the level of probability of exceedance is significantly lower than that of the BPT distribution. The predicted exceedance probability using Weibull distribution is 4% to 8% lower in Nankai-Tonankai-Tokai segments for  $PGV > 16\text{cm/s}$ , and the deficiency gradually decays as the PGV threshold rises. According to Table 3.6, it can be noticed that the number of simulated ruptures for the Weibull distribution in each segment is less than the simulation from the BPT distribution except for the Hyuga-nada segment. From the hazard functions of Weibull and BPT distribution (Figure 2.5), the reason can be obtained that BPT distribution assumes a higher rate of failure in the second 50% of the period from initial time to the mean interarrival time. As Nankai-Tonankai-Tokai segments have elapsed times greater than half of the mean interarrival time, the temporal dependency described by the hazard functions affects the predicted probability of earthquake occurrence.



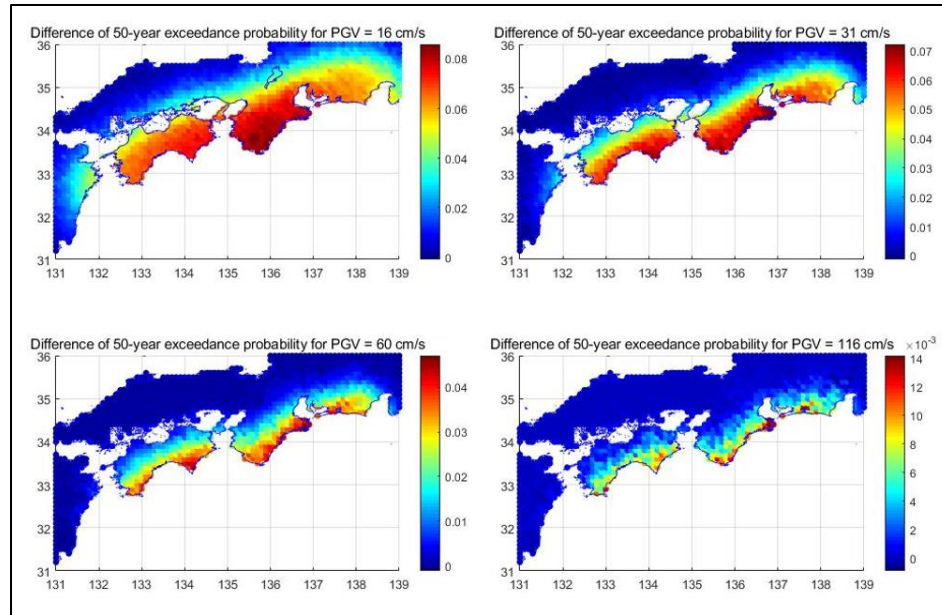


**Figure 5.6:** Difference in the probability of exceeding different levels of PGV for occurrence modelling results of the 6-segment model based on the base catalogue with the BPT interarrival time distribution to the Weibull distribution. A major excess occurs in coastal areas near Nankai-Tonankai-Tokai segments and indicates that the Weibull distribution predicts a lower exceedance probability in these regions comparing with the BPT distribution. The dominant reason is considered as the difference in the behaviour of hazard functions at different time stages of certain probabilistic distributions.

Comparing with the plot of exceedance probability at all levels of PGV for the BPT distribution simulations, the exponential distribution generated similar exceedance probabilities in areas near the Nankai and Tonankai segments. However, unlike the central areas, the Tokai region tends to have less probability of exceeding different levels of PGV, while the areas near the Hyuga-nada segment tend to have a higher level of exceedance probabilities based on the exponential distribution. As presented in Table 3.6, the difference in the number of simulated earthquakes at individual segments is the main reason for the discrepancy in the estimated probability of exceedance in areas near different segments. The reason for these differences is that exponential distribution is not able to capture the elapsed time effect and always assumes a constant hazard rate through

time. Thus, exponential distribution predicts a higher exceedance probability in Hyuganada which ruptured most recently, and a lower exceedance probability in the Tokai segment, which has the longest elapsed time than BPT distribution. In a short conclusion, the selection of interarrival time distribution function during occurrence modelling thus can affect the ground motion estimation in different areas.

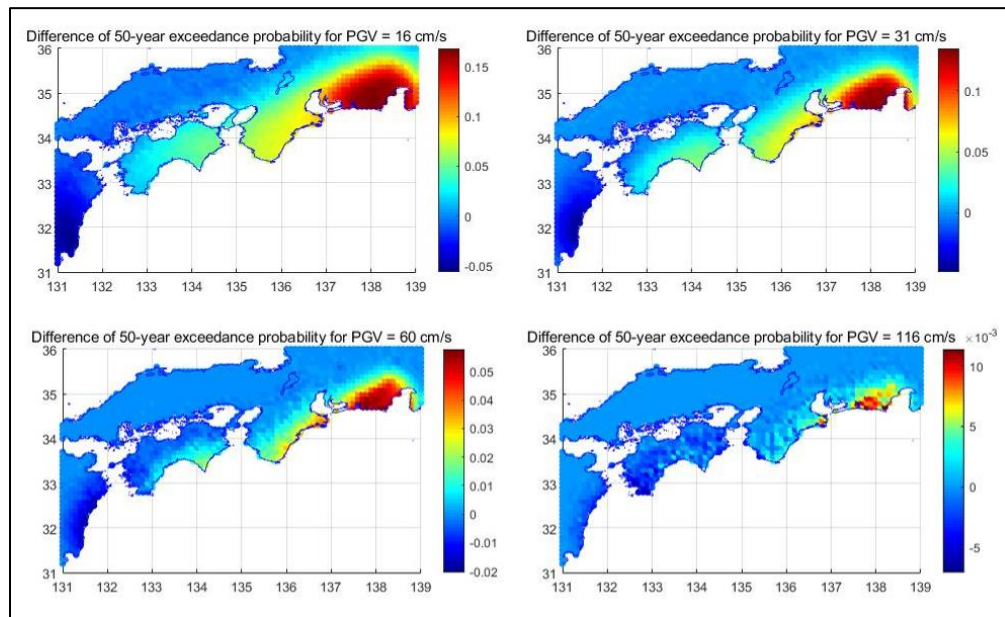


**Figure 5.7:** Difference in the probability of exceeding different levels of PGV for occurrence modelling results of the 6-segment model based on the base catalogue with the BPT interarrival time distribution to the exponential distribution. A major excess occurs in coastal areas near the Tokai segment and indicates that the exponential distribution predicts a lower exceedance probability in these regions comparing with the BPT distribution. Meanwhile, a major deficiency occurs in coastal areas near the Hyuganada segment.

As discussed in Chapter 3, the selection of the type of segment model is an important factor that affects the total moment release of possible rupture patterns and the total probability of rupture occurrence. The 3-segment model tends to reduce the overall

rupture probability due to the absence of the Hyuga-nada segment and the difference in the spatial correlation assigned between segments. In the parameter estimation stage, a higher spatial correlation is assigned between Tonankai and Tokai segments. Furthermore, the Nankai or Tonankai segment rupture in the 3-segment model corresponds to the two-segment rupture pattern in the 6-segment model, and automatically assumes the spatial correlation is 1 within Nankai (A and B) or Tonankai (C and D) segments; Thus, the estimated ground motions for the 3-segment model simulation, using the same base catalogue and BPT interarrival time distribution, tend to concentrate in the Nankai-Tonankai segment region with a higher exceedance probability than the 6-segment model, as shown in Figure 5.8. The other areas, the Tokai segment and Hyuga-nada segment, have a lower probability of exceeding all PGV levels, and the decaying trend agrees with the variation of simulated earthquakes in Table 3.4.

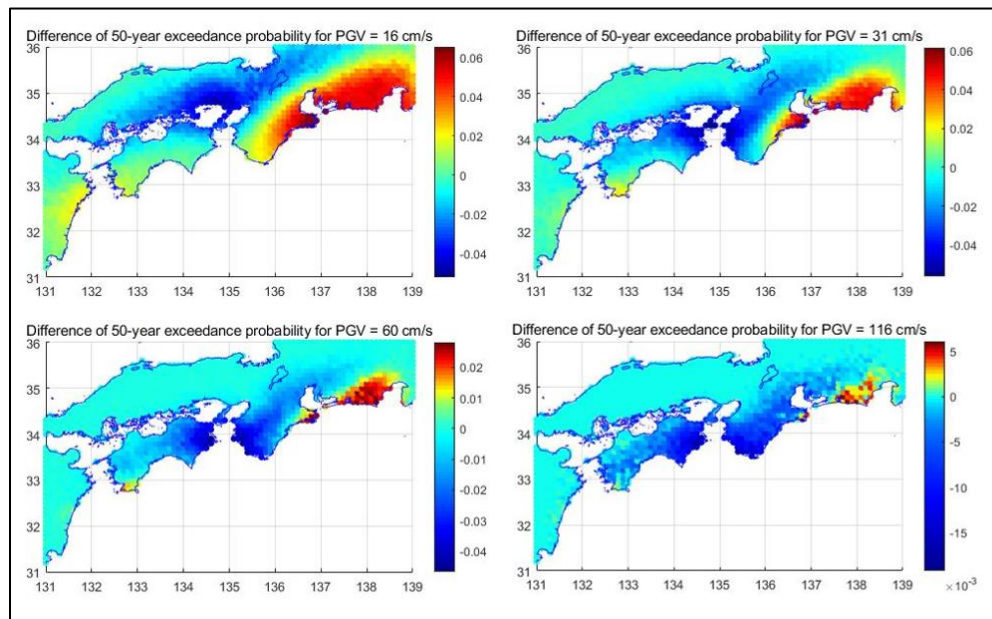


**Figure 5.8:** Difference in the probability of exceeding different levels of PGV for occurrence modelling results of the 6-segment model based on the base catalogue with the BPT interarrival time distribution to the 3-segment model with the BPT distribution. A major excess occurs in coastal areas near the boundary between Tonankai and Tokai segments and a small excess near the Hyuga-nada segment at lower PGV thresholds. The

observation indicates that the exponential distribution predicts a lower exceedance probability in these regions comparing with the 6-segment model. Meanwhile, a major deficiency occurs in coastal areas near the boundary between Tonankai and Nankai segments.

The concentration of the high-probability region in the Nankai-Tonankai segment also occurs in the 3-segment model with other interarrival time distributions, such as exponential distribution. Moreover, Figure 5.9 illustrates the difference of the exceedance probability estimated from the simulation results of the 3-segment model using the exponential distribution and base catalogue. The exceedance probabilities of all Nankai, Tonankai, and Tokai segments are decreased due to the replacement of the BPT distribution with the exponential distribution (Figure 5.8). Furthermore, the exceedance probability in the Nankai-Tonankai region caused by the segment division pattern can still be recognized when compared to the 6-segment model result with the same distribution.

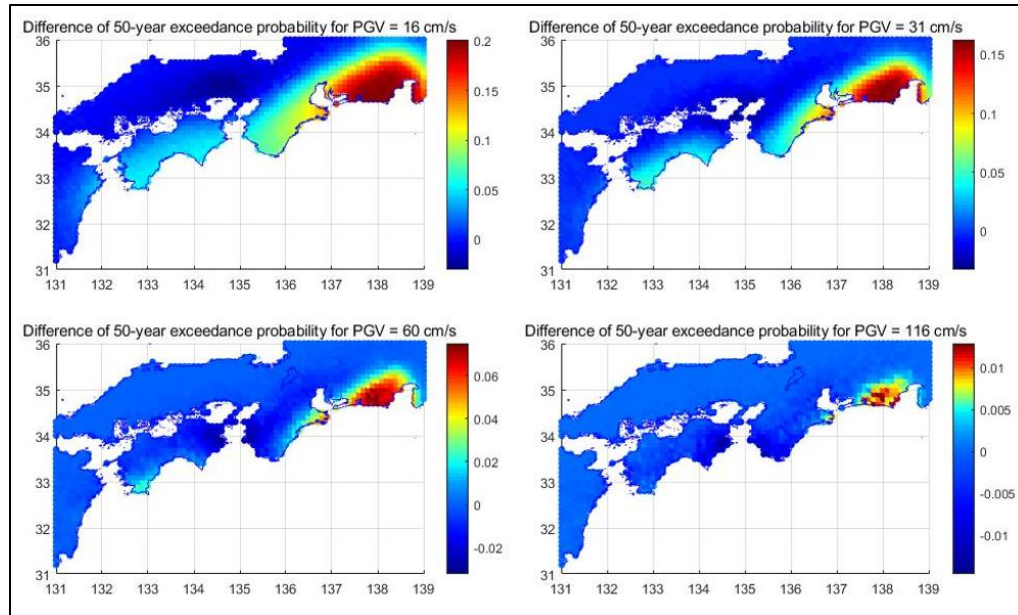


**Figure 5.9:** Difference in the probability of exceeding different levels of PGV for occurrence modelling results of the 6-segment model based on the base catalogue with the BPT interarrival time distribution to the 3-segment model with the exponential distribution. A major excess occurs in coastal areas near the Tokai segment and indicates that the 3-segment model with exponential distribution predicts a lower exceedance probability in these regions comparing with the 6-segment model. Meanwhile, a small deficiency occurs in coastal areas near the boundary between Tonankai and Nankai segments.

The last potential factor to the ground motion estimation is the earthquake catalogue incorporating different historical earthquake rupture information. While the occurrence modelling employs different types of catalogues, the rupture probability and the interarrival time remain unchanged for both models, as discussed in Chapter 3. However, the simulated earthquake occurrences for each segment vary vastly when different catalogues are incorporated into the simulation. The probability of exceedance of ruptures simulated using the 1605 catalogue, which assumes the 1605 earthquake ruptured the Nankai segments only. Figure 5.10 demonstrates the differences in exceedance probability of ruptures simulated using the 1605 catalogue with the BPT distribution for

the 6-segment model. Compared to their corresponding simulated results using the base catalogue, the region of high exceedance probability tends to shift to areas around the Nankai segments, while reducing the exceedance probability in the Tokai region. Thus, removal or addition of the historical rupture patterns would exhibit a strong effect in estimated ground motion in certain regions depending on the variation in the catalogue.

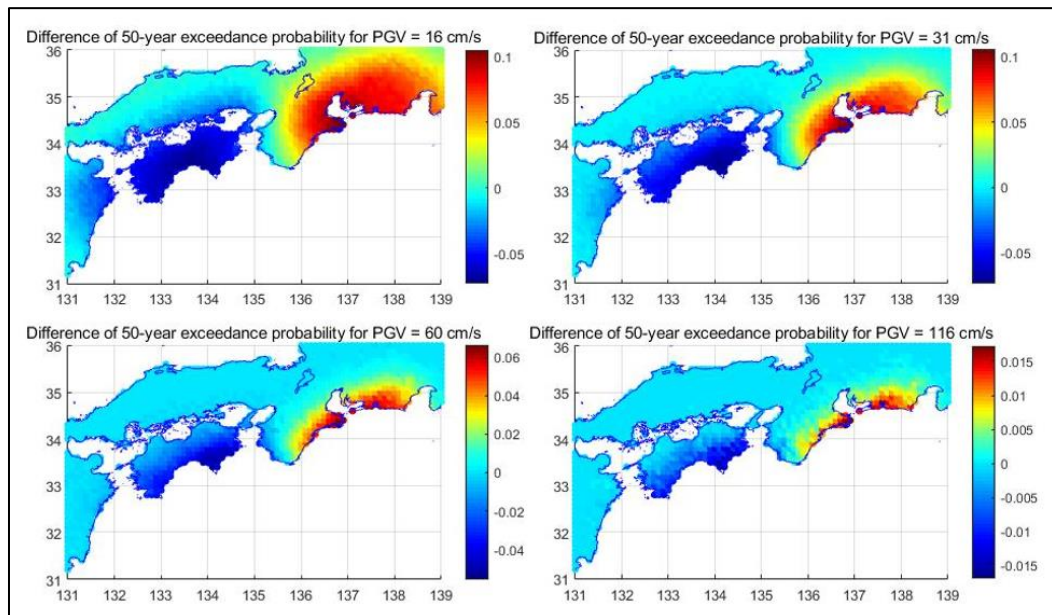


**Figure 5.10:** Difference in the probability of exceeding different levels of PGV for occurrence modelling results of the 6-segment model based on the base catalogue with the BPT interarrival time distribution to the 6-segment model based on the 1605 catalogue with the same distribution. A major excess occurs in coastal areas near the Tokai segment and indicates that the 1605 catalogue predicts a lower exceedance probability in these regions comparing with the base catalogue. Meanwhile, a major deficiency occurs in coastal areas near the Tonankai and Nankai segments as indicated by the dark blue colour.

## 5.4 Conclusions of Nankai-Tonankai Trough ground motion estimation

Values of peak ground velocity, as estimated based on stochastically generated heterogeneous slip models, are calculated for all simulated earthquake occurrences by using the Morikawa-Fujiwara GMM. By setting up four PGV thresholds that represent moderate, moderate/heavy, heavy, and very heavy damage, the regional distribution of exceedance probability implies the potential high-risk areas of Japan in the next 50 years. As suggested by all models, the multivariate-stochastic hybrid earthquake modelling method generated a realistic ground motion estimation that agrees with the historical Nankai-Tonankai seismicity. The coastal region near the Nankai and Tonankai region has a high probability of 40%-50% to experience moderate damage and very strong shaking. Models using the time-dependent distributions indicate that the Tokai region has the highest probability of rupture and inducing moderate damage and very strong shaking, while the model using the time-independent exponential distribution tends to estimate a much lower exceedance probability in the Tokai region. For exceedance probability of  $PGV > 116$  cm/s, which corresponds to potential violent shaking and heavy damage in MMI scale, a probability between 4%-6% is obtained by using different models for regions near the Nankai, Tonankai, and Tokai regions. Furthermore, the variation and shift of the spatial distribution of exceedance probability are also influenced by the segmentation and historical earthquake occurrence pattern.

After applying variation in the input setting, all models are still able to capture the features of main seismically active regions. However, the selection of segmentation model, interarrival time distribution, and the uncertainty within the earthquake occurrence catalogue would potentially affect the level of probability of exceedance in certain areas. Thus, it is vital to compare the existing research and professional opinions to determine the selection on segment model and interarrival time distribution. A credible occurrence modelling will require the most appropriate selection of data and the stable earthquake occurrence catalogue, both of which can be achieved after incorporating further supporting evidence from relevant research.

## Chapter 6

### 6 Conclusions

In this thesis, a multivariate-stochastic hybrid earthquake occurrence modelling method is developed by focusing on the segmented rupture simulation of the potential near-future Nankai-Tonankai megathrust earthquakes. The current work also represents the first case study of earthquake simulation by applying the segmented spatial-temporal dependent earthquake simulation method with stochastic heterogeneous slips in Nankai-Tonankai Trough. As stated in Chapter 1, the main objective is to combine the multivariate Bernoulli earthquake simulation method with the stochastic heterogeneous slip models and focus on the segmented rupture scenarios in Nankai-Tonankai megathrust earthquakes which is likely to occur in the next 50 years.

From the literature review (Chapter 2), evidence of the historical rupture pattern of all historical megathrust earthquakes is summarized as the fundamental input information for earthquake occurrence simulation. The historical rupture conditions at individual segments allow carrying out earthquake occurrence simulation by considering both spatial and temporal dependency. As a result, the major tendency of Nankai and Tonankai segments rupturing is captured by the simulation. Furthermore, the possible variation in input information and simulation setting (i.e. earthquake catalogue, interarrival distribution and segmentation pattern) are examined to have obvious effects on the simulated rupture behaviour of individual segments. By assigning the moment magnitude and asperity zone to all potential rupture patterns, the heterogeneous slip models are stochastically generated for each rupture scenario under realistic constraints and linked to the earthquake occurrence simulation results. The application of the hybrid simulation method in ground motion estimation is further proposed for checking the effectiveness of the earthquake simulation method. According to the setting of PGV thresholds, which directly correlates with the potential damage and shaking that a site would experience, the interpretation of possible future damage is feasible and intuitive. In a map view, the major seismicity pattern in the Nankai-Tonankai region is captured, while the influential factors such as elapsed time and historical rupture conditions are



found affecting the level of exceedance probability at specific segments and the spatial distribution of high-risk areas as in earthquake occurrence simulations.

## 6.1 Summary of Nankai-Tonankai Trough earthquake simulation and ground motion estimation using the multivariate-stochastic hybrid method

The earthquake simulation is first modified by the multivariate Bernoulli model, which incorporates both spatial and temporal distribution of individual segments into rupture simulation. To set up the segmentation pattern of the whole rupture region, two types of models are developed by considering the seismicity and spatial correlation between segments. The 3-segment model divides the Nankai-Tonankai Trough into the Nankai, Tonankai and Tokai segments, respectively. The Nankai and Tonankai segments, which are both composed of two smaller segments, are each combined into a larger segment due to their high correlation to rupture together in history. On the other hand, the 6-segment model treats the Nankai, Tonankai and Tokai segments as five individual segments, while adding the Hyuga-nada segment. The input information, historical earthquake occurrence catalogues, is gathered according to historical, geological, and geophysical evidence to possibly eliminate the uncertainty resulting from the obscure and fictitious records. Furthermore, two more catalogues are set up by incorporating different hypotheses regarding the rupture condition for the certain earthquake to examine the effect of variation in earthquake occurrence catalogue on earthquake occurrence simulation. The impact of taking different interarrival time distributions that are employed for characterizing the temporal dependency of the individual segment is also tested. After simulation and comparison, the major seismicity at Nankai and Tonakai segments is captured by the multivariate Bernoulli model. However, all three factors, i.e. earthquake catalogue, interarrival time distribution and segmentation model, are also found influencing the simulated earthquake occurrences both in overall rupture probability and the number of simulated ruptures in particular segments.

To generate more realistic heterogeneous slips for the earthquake occurrences, the stochastic slip modelling method is utilized for producing slip models corresponding to different rupture scenarios, which are set based on empirical scaling laws and the optimal source model developed by Central Disaster Management Council. 500 slip models are generated for each scenario to account for the variability of stochastic synthesis parameters and slip parameters. The earthquake occurrences, as iteratively simulated 20,000 times, are then able to be individually assigned with one randomly selected slip model for the same rupture scenario.

In the end, ground motion estimation is carried out to examine the validity of the hybrid earthquake occurrence modelling method. By setting up the sites with an equal interval of  $0.1^\circ$  throughout Japan, the peak ground velocity is calculated and linked with potential damage and shaking based on the exceedance probability of different thresholds. As suggested by the exceedance rate from all types of rupture simulation results, there is a 40%-50% chance that Japan will experience moderate damage and very strong shaking (VII in Modified Mercalli Intensity scale) due to megathrust earthquakes in the next 50 years. The coastal areas of Nankai, Tonankai and Tokai segments can experience potential violent shaking and heavy damage (X+ in Modified Mercalli Intensity scale) with a probability between 4%-6%. Furthermore, the effect of variation earthquake catalogue, interarrival time distribution and segment model on earthquake occurrence simulation is found to be propagated to the ground motion estimation by changing the estimated exceedance probability of certain regions. When considering the elapsed time of individual segments, the Tokai region is also marked as a high-risk area with a lower potential of exceeding very high PGV than the Nankai-Tonankai segments. In contrast, the exceedance probability in the Tokai region significantly decreases when employing the time-independent interarrival distribution (i.e. exponential distribution), and the Hyuga-nada segment is considered to have a larger probability of rupturing over 50 years, which leads to higher exceedance probability estimates. The addition and exclusion of certain rupture conditions and segments would also cause a major impact on the simulated rupture behaviour of corresponding segments.

## 6.2 Limitation of multivariate-stochastic earthquake occurrence modelling

As discussed in the above section, the variation in earthquake catalogue, interarrival time distribution, and segment model can lead to different seismic features in certain segments and variation in the overall rupture probability of simulated earthquakes. The precise earthquake catalogue is difficult to build and to obtain supporting evidence for earthquakes with relatively long recurrence periods and occurred a long time earlier than modern digital seismogram data. To complement the obscure and missing/fictitious record, one efficient solution is to find supporting evidence from other domains, such as geology and geophysics, which requires significant time for carrying out research. The segmentation pattern also plays an important role in controlling the estimated moment releasing of the simulated earthquakes. The effect further extends to the setting of constraints of stochastic slip model generation. Thus, the fault segmentation pattern needs to be as accurate as possible to avoid large uncertainties associated with the simulated earthquake occurrence. The last factor, interarrival time distributions, is difficult to select which one best represents the interarrival occurrence time. The G-R relationship, as shown in Figure 5.3, is able to act as an empirical reference for selecting the distribution that helps to simulate earthquakes with an adequate annual exceedance rate of events with a magnitude greater than  $M_w 7.5$  by taking the historical earthquake catalogue as the reference. However, comparisons in other seismic genres are also needed to support the argument.

## 6.3 Future works

The multivariate-stochastic hybrid earthquake occurrence modelling method is able to be improved by building a more precise earthquake catalogue, setting the optimal interarrival distribution and determining the most characteristic segmentation pattern as aforementioned. To make the most probable decision, supporting evidence is needed to be gathered from multiple domains of empirical research, including history, statistics, geology and geophysics. Furthermore, the other case studies would also provide direction

for making segmentation division, selecting the interarrival distribution and establishing earthquake catalogues. For instance, the hybrid earthquake occurrence simulation method can be applied in other segmented areas, such as the coastal area of Lima, Peru, to examine the best selection of interarrival distribution that simulates earthquake occurrences highly fitting to the empirical frequency-magnitude relations.

The application of the hybrid earthquake occurrence modelling method can further extend to the tsunami hazard assessment. The stochastic slip models, as modelled from the random field generation method, are capable of generating the kinetic rupture parameters, including rupture propagation speed and rise time too (Goda et al., 2020). For Japan, the potential tsunami hazard caused by the megathrust earthquake in the near future is also essential in making decisions on risk mitigation and damage estimation.

Moreover, the multi-hazard risk assessment can be conducted by incorporating the hybrid earthquake occurrence. As demonstrated in Chapter 5, the exceedance probability of PGVs directly correlates to the potential shaking and damage that a site would experience. For making the risk assessment, the probability for an event to occur at a particular magnitude plays an important role in assessing the vulnerability in areas for primary and induced hazards.

## References

- Abrahamson, N., Gregor, N., & Addo, K. (2016). *BC Hydro Ground Motion Prediction Equations for Subduction Earthquakes*. *Earthquake Spectra*, 32: 23-44.
- Aida, I. (1981). *Numerical experiments for the tsunami generated off the coast of the Nankaido district*. *Bulletin of the Earthquake Research Institute*, 56: 731–740(in Japanese)
- Ammon, C.J., Lay, T., Kanamori, H. et al. (2011). *A rupture model of the 2011 off the Pacific coast of Tohoku Earthquake*. *Earth, Planets and Space*, 63(7): 693–696.
- Andô, M. (1975). *Source mechanisms and tectonic significance of historical earthquakes along the nankai trough, Japan*. *Tectonophysics*, 27: 119-140.
- Andô, M. (1982). *A fault model of the 1946 Nankaido earthquake derived from tsunami data*. *Physics of the Earth and Planetary Interiors*, 28: 320-336.
- Andô, M., & Nakamura, M. (2013). *Seismological evidence for a tsunami earthquake recorded four centuries ago on historical documents*. *Geophysical Journal International*, 195: 1088-1101.
- Andrews, D. (1980). *A stochastic fault model: 1. Static case*. *Journal of Geophysical Research*, 85: 3867-3877.
- Baba, T., Y. Tanioka, P., Cummins, R., & Uhira, K. (2002). *The slip distribution of the 1946 Nankai earthquake estimated from tsunami inversion using a new plate model*. *Physics of the Earth and Planetary Interiors*, 132 (1-3): 59-73.
- Barbot, S., Lapusta, N., & Avouac, J. (2012). *Under the Hood of the Earthquake Machine: Toward Predictive Modeling of the Seismic Cycle*. *Science*, 336: 707-710.
- Bak, P., & Tang, C. (1989). *Earthquakes as a self-organized critical phenomenon*. *Journal of Geophysical Research*, 94: 15635-15637.

- Ben-Zion, Y., & Lyakhovsky, V. (2002). *Accelerated seismic release and related aspects of seismicity patterns on earthquake faults*. *Pure Applied Geophysics* 159: 2385–2412
- Beroza, G., & Spudich, P. (1988). *Linearized inversion for fault rupture behavior: Application to the 1984 Morgan Hill, California, earthquake*. *Journal of Geophysical Research*, 93: 6275-6296.
- Ceferino, L., Galvez, P., Ampuero, J., Kiremidjian, A., Grégory, Deierlein, & Villegas-Lanza, J.C. (2019). *Bayesian parameter estimation for space and time interacting earthquake rupture model using historical and physics-based simulated earthquake catalogs*. *Bulletin of the Seismological Society of America*, Conference article.
- Ceferino, L., Kiremidjian, A., & Deierlein, G. (2020). *Probabilistic Space- and Time-Interaction Modeling of Mainshock Earthquake Rupture Occurrence*. *Bulletin of the Seismological Society of America*. 10 (5): 2498–2518.
- Console, R & Murru, M. & Falcone, G. (2017). *Earthquake Occurrence: Short- and Long-term Models and their Validation*. Wiley-ISTE published, 1st edition
- Davis, E., Becker, K., Wang, K., Obara, K., Ito, Y., & Kinoshita, M. (2006). *A discrete episode of seismic and aseismic deformation of the Nankai trough subduction zone accretionary prism and incoming Philippine Sea plate*. *Earth and Planetary Science Letter* 242:73–78
- Fitch, T., & Scholz, C. (1971). *Mechanism of underthrusting in southwest Japan: A model of convergent plate interactions*. *Journal of Geophysical Research*, 76: 7260-7292.
- Fujiwara, O., Aoshima, A., Irizuki, T., Ono, E., Obrochta, S., Sampei, Y., Sato, Y., & Takahashi, A. (2020). *Tsunami deposits refine great earthquake rupture extent and recurrence over the past 1300 years along the Nankai and Tokai fault segments of the Nankai Trough, Japan*. *Quaternary Science Reviews*, 227: 105999.

- Furumura, T., Imai, K., & Maeda, T. (2011). *A revised tsunami source model for the 1707 Hoei earthquake and simulation of tsunami inundation of Ryujin Lake, Kyushu, Japan*. *Journal of Geophysical Research*, 116: B2
- Fujiwara, H., Morikawa, N., Okumura, T., Ishikawa, Y., & Nojima, N. (2012). *Revision of Probabilistic Seismic Hazard Assessment for Japan after the 2011 Tohoku-oki Mega-thrust Earthquake (M9.0)*. 15th World Conference on. Earthquake Engineering 2012, (15WCEE). Lisbon, Portugal. 24-28 September 2012, 4571-4580.
- Garrett, E., Fujiwara, O., Garrett, P., Heyvaert, V.M., Shishikura, M., Yokoyama, Y., Hubert-Ferrari, A., Brückner, H., Nakamura, A., & Batist, M. (2016). *A systematic review of geological evidence for Holocene earthquakes and tsunamis along the Nankai-Suruga Trough, Japan*. *Earth-Science Reviews*, 159: 337-357.
- Ghofrani, H., & Atkinson, G. (2013). *Ground-motion prediction equations for interface earthquakes of M7 to M9 based on empirical data from Japan*. *Bulletin of Earthquake Engineering*, 12: 549-571.
- Goda, K., & Atkinson, G. (2010). *Intraevent spatial correlation of ground-motion parameters using SK-net data*. *Bulletin of the Seismological Society of America*, 100: 3055-3067.
- Goda, K., Yasuda, T., Mori, N., & Maruyama, T. (2016). *New scaling relationships of earthquake source parameters for stochastic tsunami simulation*. *Coastal Engineering Journal*, 58: 1650010-1 - 1650010-40.
- Goda, K., Yasuda, T., Mori, N., Muhammad, A., Risi, R., & Luca, F.D. (2020). *Uncertainty quantification of tsunami inundation in Kuroshio, Kochi Prefecture, Japan, using the Nankai–Tonankai megathrust rupture scenarios*. *Natural Hazards and Earth System Sciences*, 20: 3039-3056.
- Guatteri, M., Mai, P.M., Beroza, G., & Boatwright, J. (2003). *Strong ground-motion prediction from stochastic-dynamic source models*. *Bulletin of the Seismological Society of America*, 93: 301-313.

- Gusev, A. (1992). *On relations between earthquake population and asperity population on a fault*. Tectonophysics, 211: 85-98.
- Gutenberg, B., & Richter, C. (1956). *Magnitude and energy of earthquakes*. Annals of Geophysics, 9: 1-15.
- Griffith, A. (1924). *The theory of rupture*. In: Proc., Ist., Int., Congr., Appl., Mech. Biereno, C.B. Burgers, J.M(eds). Delft: Tech. Boekhandel en Drukkerij. J. Waltman Jr., 54-63.
- Hagiwara, Y. (1974). *Probability of earthquake occurrence as obtained from a Weibull distribution analysis of crustal strain*. Tectonophysics, 23: 313-318.
- Herrero, A., & Bernard, P. (1994). *A kinematic self-similar rupture process for earthquakes*. Bulletin of the Seismological Society of America, 84: 1216-1228.
- Hirshorn, B., & Weinstein, S. (2009). *Earthquake Source Parameters*. NOAA/NWS/Pacific Tsunami Warning Center, Ewa Beach, USA
- Ichinose, G.A., Thio, H.K., Somerville, P.G., Sato, T., & Ishii, T. (2003). *Rupture process of the 1944 Tonankai earthquake (M-s 8.1) from the inversion of teleseismic and regional seismograms*. Journal of Geophysical Research, 108 (B10): B2497.
- Iryu, Y., Maemoku, H., Yamada, T., & Maeda, Y. (2009). *Limestones as a paleobathymeter for reconstructing past seismic activities: Muroto-misaki, Shikoku, southwestern Japan*. Global and Planetary Change, 66: 52-64.
- Ishibashi, K. (1981). *Specification of a Soon-to-Occur Seismic Faulting in the Tokai District, Central Japan, Based Upon Seismotectonics*. In Earthquake Prediction (eds D.W. Simpson and P.G. Richards).
- Ishibashi, K. (2004). *Status of historical seismology in Japan*. Annals of Geophysics, 47(2): 10.4401/ag-3305.



- Ishibashi, K. (2016). *Possibility that the 1099 Jotoku (Kowa) Nankai earthquake is unreal and the 1096 Kaho (Eicho) earthquake was an “Entire-Nankai Trough” earthquake: examination of Kansenji-an, a historical document describing an earthquake in Shikoku*. *Hist. Earthquakes*, 31: 81-88.
- Olami, Z., Feder, H. J., & Christensen, K. (1992), *Self-organized criticality in a continuous, nonconservative cellular automaton modeling earthquakes*. *Physical Review Letters*, 68(8): 1244-1247
- Kagan, Y.Y., & Knopoff, L. (1987). *Random stress and earthquake statistics: spatial dependence*. *Geophysical Journal International*, 88(3): 723–731.
- Kanamori, H. (1972). *Tectonic implications of the 1944 Tonankai and the 1946 Nankaido earthquakes*. *Physics of the Earth and Planetary Interiors*, 5: 129-139.
- Kano, M., & Kato, A. (2020). *Detailed spatial slip distribution for short-term slow slip events along the Nankai subduction zone, southwest Japan*. *Journal of Geophysical Research*, 125.
- Kato, T., & Ando, M. (1997). *Source mechanisms of the 1944 Tonankai and 1946 Nankaido earthquakes: Spatial heterogeneity of rise times*. *Geophysical Research Letters* 24(16): 2055-2058.
- Kikuchi, M., Nakamura, M., & Yoshikawa, K. (2003). *Source rupture processes of the 1944 Tonankai earthquake and the 1945 Mikawa earthquake derived from low-gain seismograms*. *Earth Planets and Space* 55(4): 159-172.
- Kimura, H., Tadokoro, K., & Ito, T. (2019). *Interplate coupling distribution along the Nankai Trough in southwest Japan Estimated from the block motion model based on onshore GNSS and seafloor GNSS/A observations*. *Journal of Geophysical Research*, 124: 6140-6164.

- Kodaira, S., Takahashi, N., Park, J., Mochizuki, K., Shinohara, M., & Kimura, S. (2000). *Western Nankai Trough seismogenic zone: Results from a wide-angle ocean bottom seismic survey*. *Journal of Geophysical Research*, 105: 5887-5905.
- Kodaira, S., Hori, T., Ito, A., Miura, S., Fujie, G., Park, J., Baba, T., Sakaguchi, H., & Kaneda, Y. (2006). *A cause of rupture segmentation and synchronization in the Nankai trough revealed by seismic imaging and numerical simulation*. *Journal of Geophysical Research*, 111: B7.
- Lavallée, D., Liu, P., & Archuleta, R. (2006). *Stochastic model of heterogeneity in earthquake slip spatial distributions*. *Geophysical Journal International*, 165: 622-640.
- Liu, X., Zhao, D., & Li, S. (2014). *Seismic attenuation tomography of the Northeast Japan arc: Insight into the 2011 Tohoku earthquake (Mw 9.0) and subduction dynamics*. *Journal of Geophysical Research*, 119: 1094-1118.
- Lotto, G., Jeppson, T., & Dunham, E. (2018). *Fully coupled simulations of megathrust earthquakes and tsunamis in the Japan Trench, Nankai Trough, and Cascadia subduction zone*. *Pure and Applied Geophysics*, 1-33.
- Mai, P.M., & Beroza, G. (2002). *A spatial random field model to characterize complexity in earthquake slip*. *Journal of Geophysical Research*, 107: 2308.
- Matthews, M., Ellsworth, W., & Reasenber, P. (2002). *A Brownian model for recurrent earthquakes*. *Bulletin of the Seismological Society of America*, 92: 2233-2250.
- Meyers, R. (2011). *Extreme Environmental Events. Complexity in Forecasting and Early Warning*, New York, NY. ISBN 1441976949
- Mitsui, N., & Hirahara, K. (2004). *Simple spring-mass model simulation of earthquake cycle along the Nankai Trough in southwest Japan*. *Pure and Applied Geophysics*, 161: 2433-2450.
- Mochiduki, K., & Obana, K. (2003). *Seismic Activities along the Nankai Trough*. *Bulletin of the Earthquake Research Institute*, 78: 185-195

- Morikawa, N., & Fujiwara, H. (2013). *A new ground motion prediction equation for Japan applicable up to M9 mega-earthquake*. *Journal of Disaster Research*, 8: 878-888.
- Nanjo, K., & Yoshida, A. (2018). *A b map implying the first eastern rupture of the Nankai Trough earthquakes*. *Nature Communications*, 9: 1117.
- Nishenko, S., & Buland, R. (1987). *A generic recurrence interval distribution for earthquake forecasting*. *Bulletin of the Seismological Society of America*, 77(4): 1382-1399.
- Niu, X., Zhao, D., Isozaki, Y., Nishizono, Y., & Inakura, H. (2020). *Structural heterogeneity and megathrust earthquakes in Southwest Japan*. *Physics of the Earth and Planetary Interiors*, 298: 106347.
- Obana, K., Kodaira, S., Kaneda, Y., Mochizuki, K., Shinohara, M., & Suyehiro, K. (2003). *Microseismicity at the seaward updip limit of the western Nankai Trough seismogenic zone*. *Journal of Geophysical Research*, 108: 2459.
- Okamura, M., & Matsuoka, H. (2012). *Recurrence of Nankai earthquake based on the tsunami deposit*. *Kagaku*. 82: 182-191.
- Operto, S., Virieux, J., Dessa, J., & Pascal, G. (2006). *Crustal seismic imaging from multifold on bottom seismometer data by frequency domain full waveform tomography: Application to the eastern Nankai Trough*. *Journal of Geophysical Research*, 111: B09306.
- Park, J., Fujie, G., Wijerathne, L., Hori, T., Kodaira, S., Fukao, Y., Moore, G., Bangs, N., Kuramoto, S., & Taira, A. (2010). *A low-velocity zone with weak reflectivity along the Nankai subduction zone*. *Geology*, 38: 283-286.
- Power, W., Tullis, T., Brown, S.R., Boitnott, G., & Scholz, C. (1987). *Roughness of natural fault surfaces*. *Geophysical Research Letters*, 14: 29-32.

- Reid, H.F. (1910). *Mechanics of the earthquake, the California Earthquake of April 18, 1906*. Report of the State Investigation Commission, Carnegie Institution of Washington, Washington DC.
- Rikitake, T. (1974). *Probability of earthquake occurrence as estimated from crustal strain*. *Tectonophysics*, 23:299–312.
- Rivera, L., & Kanamori, H. (2001). *Spatial heterogeneity of tectonic stress and friction in the crust*. *Geophysical Research Letters*, 29: 12-1-12-4.
- Ruiz, S., & Madariaga, R. (2018). *Historical and recent large megathrust earthquakes in Chile*. *Tectonophysics*, 733:37-56.
- Sangawa, A. (2001). *Recent results of paleoseismological study based on earthquake traces excavated at archeological sites*. *Annual Report on Active Fault and Paleoequake Researches* 1:287–300 (in Japanese)
- Satake, K. (1993). *Depth distribution of coseismic slip along the Nankai Trough, Japan, from joint inversion of geodetic and tsunami data*. *Journal of Geophysical Research*, 98: 4553-4565.
- Schumann, K., Stipp, M., Behrmann, J., Klaeschen, D., & Schulte-Kortnack, D. (2014). *P and S wave velocity measurements of water-rich sediments from the Nankai Trough, Japan*. *Journal of Geophysical Research*, 119: 787-805.
- Shishikura, M., Echigo, T., Maemoku, H., & Ishiyama, T. (2008). *Height and ages of uplifted sessile assemblage distributed along the southern coast of the Kii Peninsula, south-central Japan - Reconstruction of multi-segment earthquake history along the Nankai Trough*. *Geological Survey of Japan*, 8: 267-280.
- Si, H., & Midorikawa, S. (1999). *New attenuation relationships for peak ground acceleration and velocity considering effects of fault type and site condition*. *Journal of Structural and Construction Engineering*. 523: 63–70 (in Japanese with English abstract)

- Stein, S., Wyssession, M., & Stein, S. (Ed.) (2003). *Introduction to Seismology, Earthquakes, and Earth Structure*. Blackwell Published.
- Tanioka, Y., & Satake, K. (2001). *Coseismic slip distribution of the 1946 Nankai earthquake and aseismic slips caused by the earthquake*. *Earth Planets and Space* 53(4): 235-241.
- Thingbaijam, K.S., Mai, P.M., & Goda, K. (2017). *New Empirical Earthquake Source-Scaling Laws*. *Bulletin of the Seismological Society of America*, 107: 2225-2246.
- Weibull, W. (1939). *A statistical theory of the strength of materials*. Ingvetensk Akad Handlno151.
- Wood, H. O., & Neumann, F. (1931). *Modified Mercalli Intensity Scale of 1931*. *Seismological Society of America Bulletin*, 21(4): 277-283.
- Yamamoto, Y., Obana, K., Kodaira, S., Hino, R., & Shinohara, M. (2014). *Structural heterogeneities around the megathrust zone of the 2011 Tohoku earthquake from tomographic inversion of onshore and offshore seismic observations*. *Journal of Geophysical Research*, 119: 1165-1180.
- Zang, S., & Ning, J. (2002). *Interaction between the Philip-pine Sea plate and the Eurasia plate and its influence on the tectonics of eastern Asia*. *Chinese Journal of Geophysics*, 45(2):184-194.
- Zhao, J.X., Liang, X., Jiang, F., Xing, H., Zhu, M., Hou, R., Zhang, Y., Lan, X., Rhoades, D., Irikura, K., Fukushima, Y., & Somerville, P. (2016). *Ground-Motion Prediction Equations for Subduction Slab Earthquakes in Japan Using Site Class and Simple Geometric Attenuation Functions*. *Bulletin of the Seismological Society of America*, 106: 1518-1534.

## Appendices

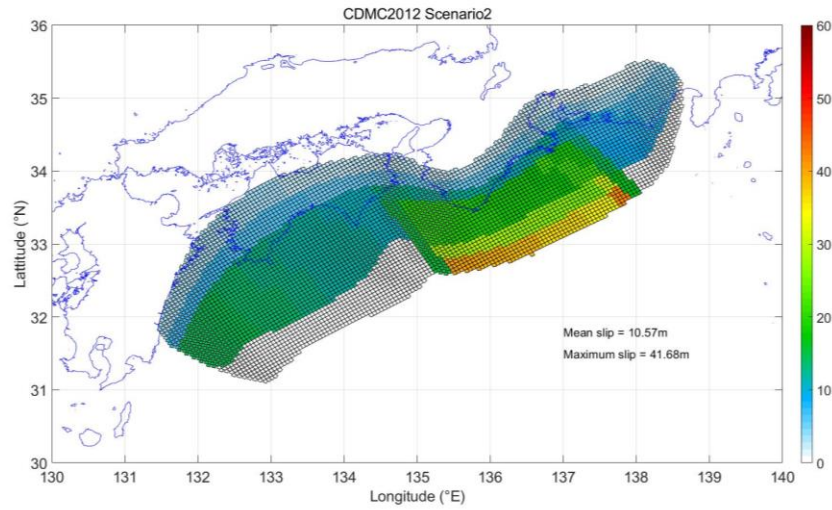


**Figure A1:** CDMC2012 heterogenous fault slip model of scenario 2 that corresponds to the single asperity region located off Kii Peninsula.

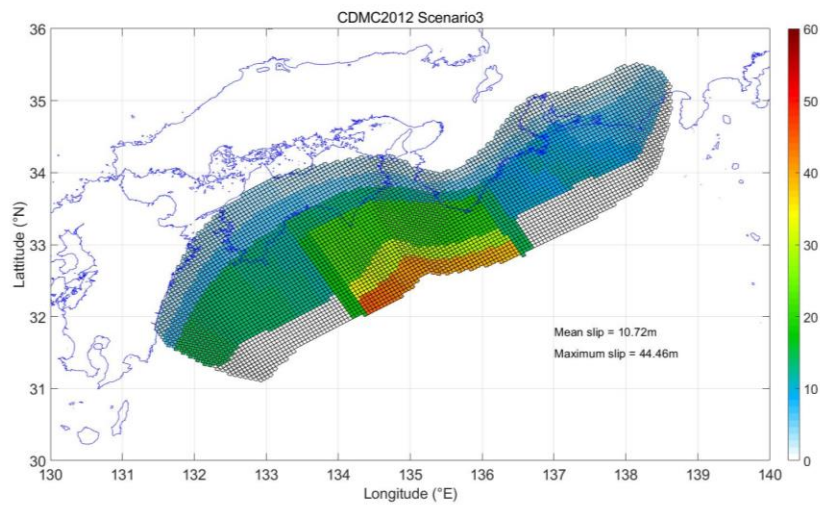


**Figure A2:** CDMC2012 heterogenous fault slip model of scenario 3 that corresponds to the single asperity region located off Kii Peninsula to Shikoku.

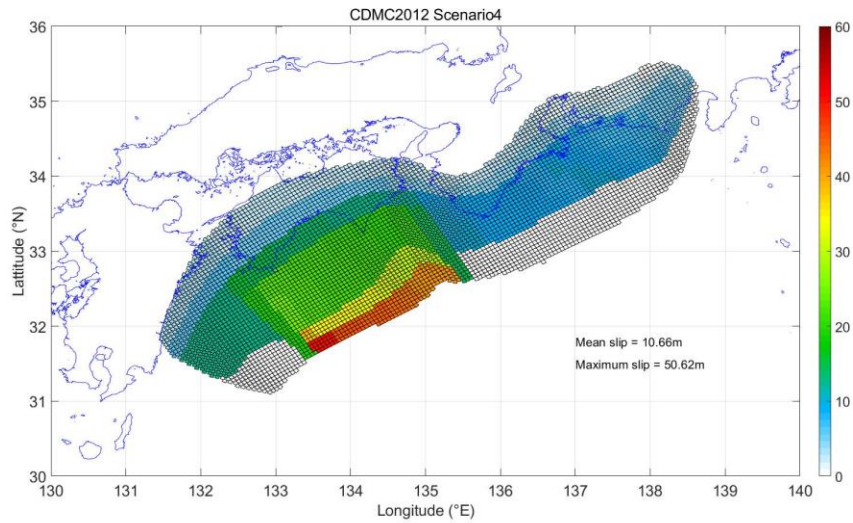


**Figure A3:** CDMC2012 heterogeneous fault slip model of scenario 4 that corresponds to the single asperity region located off Shikoku.

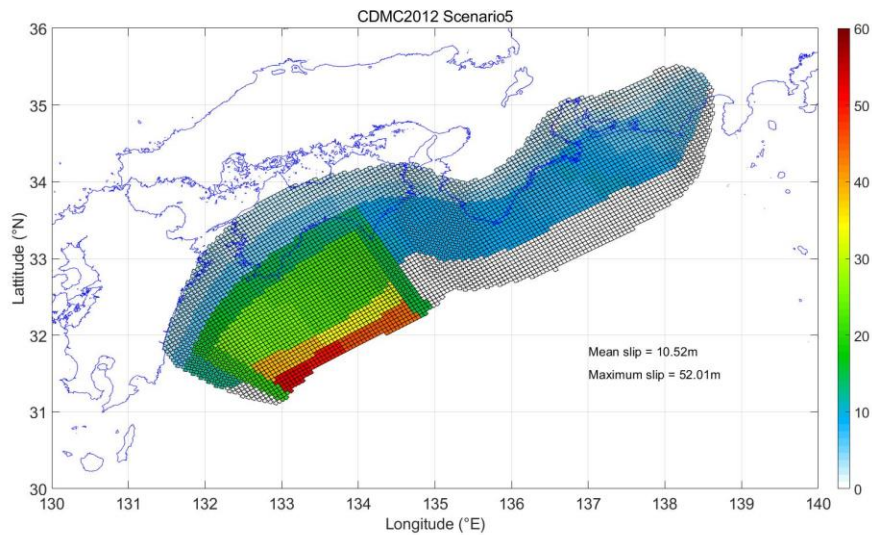


**Figure A4:** CDMC2012 heterogeneous fault slip model of scenario 5 that corresponds to the single asperity region located off Shikoku to Kyushu.

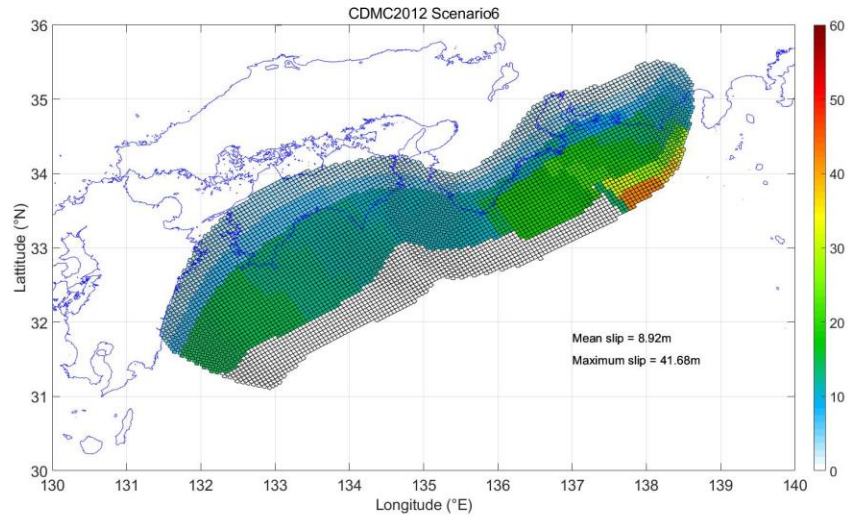


**Figure A5:** CDMC2012 heterogeneous fault slip model of scenario 6 that corresponds to the single asperity region located off Kii Peninsula while taking into account Kumano splay fault.

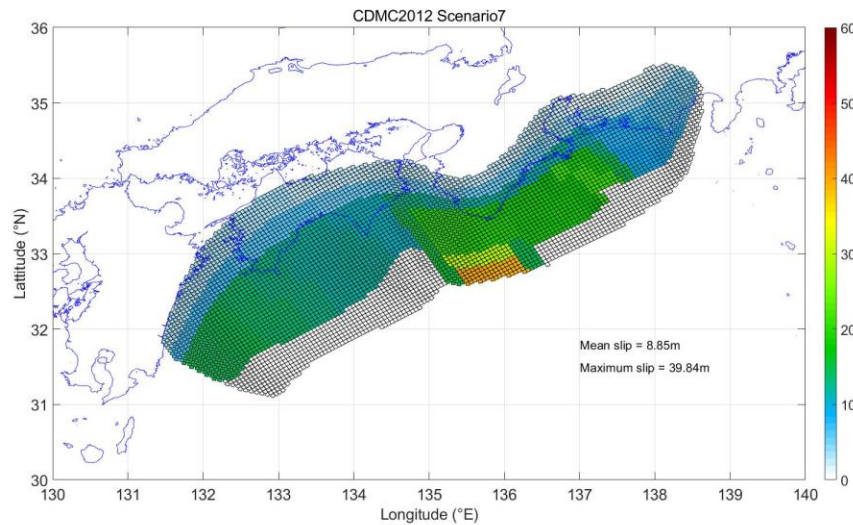


**Figure A6:** CDMC2012 heterogeneous fault slip model of scenario 7 that corresponds to the single asperity region located off Kii Peninsula while taking into account Kumano splay fault.



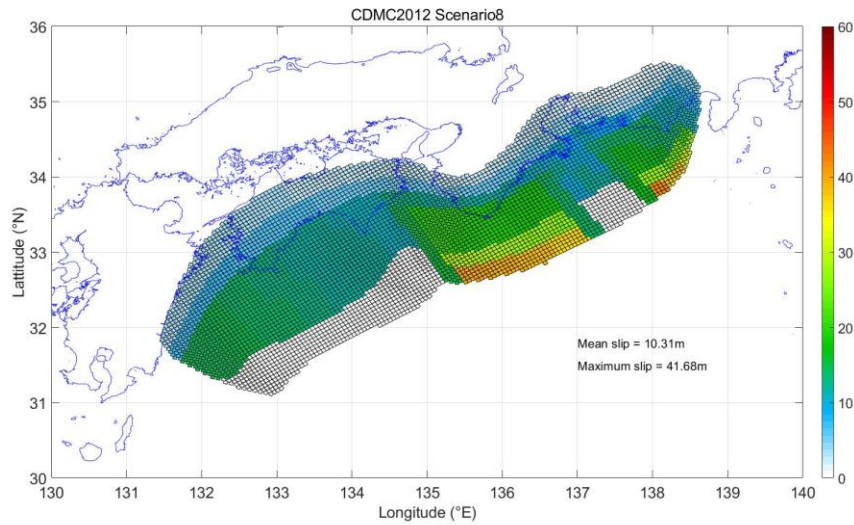


**Figure A7:** CDMC2012 heterogeneous fault slip model of scenario 8 that corresponds to the two asperity regions located off Suruga Bay to Kii Peninsula and Kii Peninsula to Shikoku, respectively.

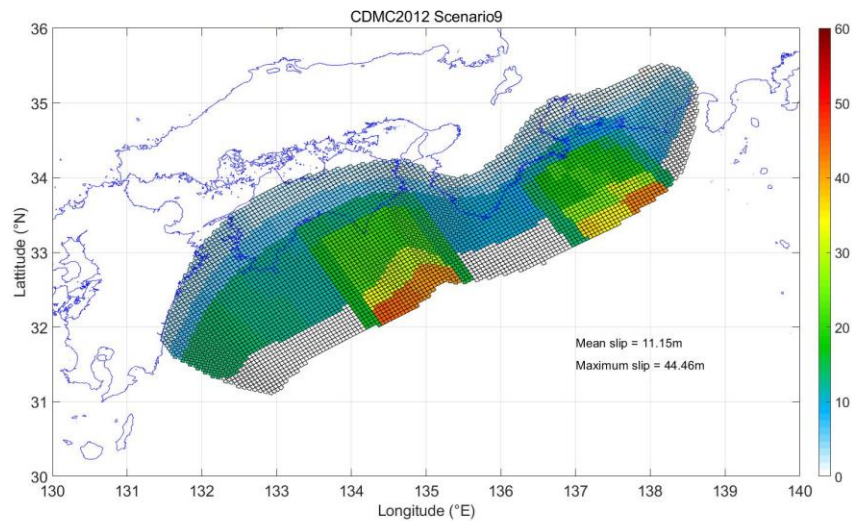


**Figure A8:** CDMC2012 heterogeneous fault slip model of scenario 9 that corresponds to the two asperity regions located off Suruga Bay to Kii Peninsula and Shikoku, respectively

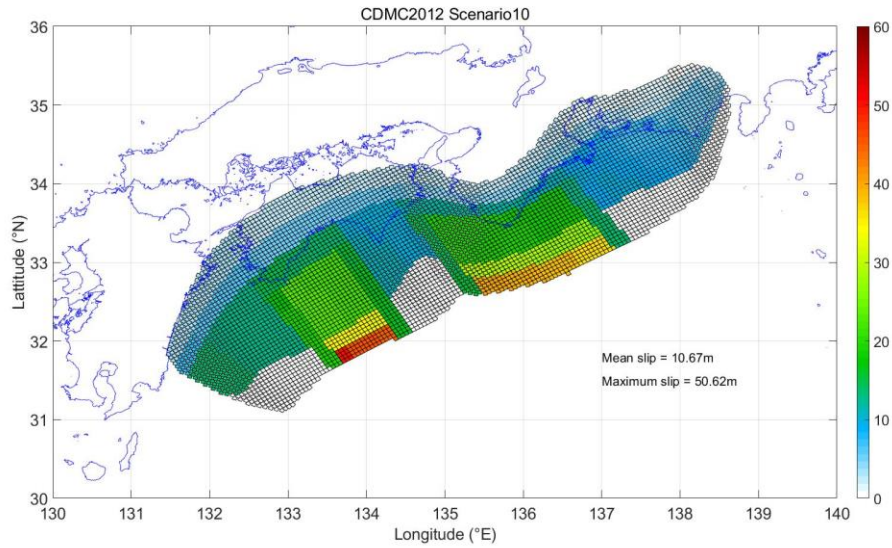


**Figure A9:** CDMC2012 heterogenous fault slip model of scenario 10 that corresponds to the two asperity regions located off Kii Peninsula to Shikoku and Shikoku to Kyushu, respectively.

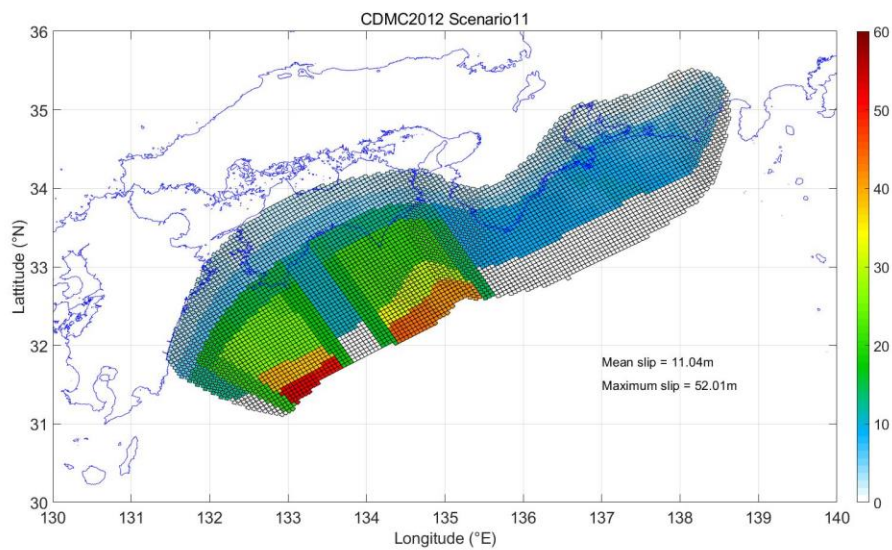


**Figure A10:** CDMC2012 heterogenous fault slip model of scenario 11 that corresponds to the two asperity regions located off Kyushu to Shikoku and Shikoku.

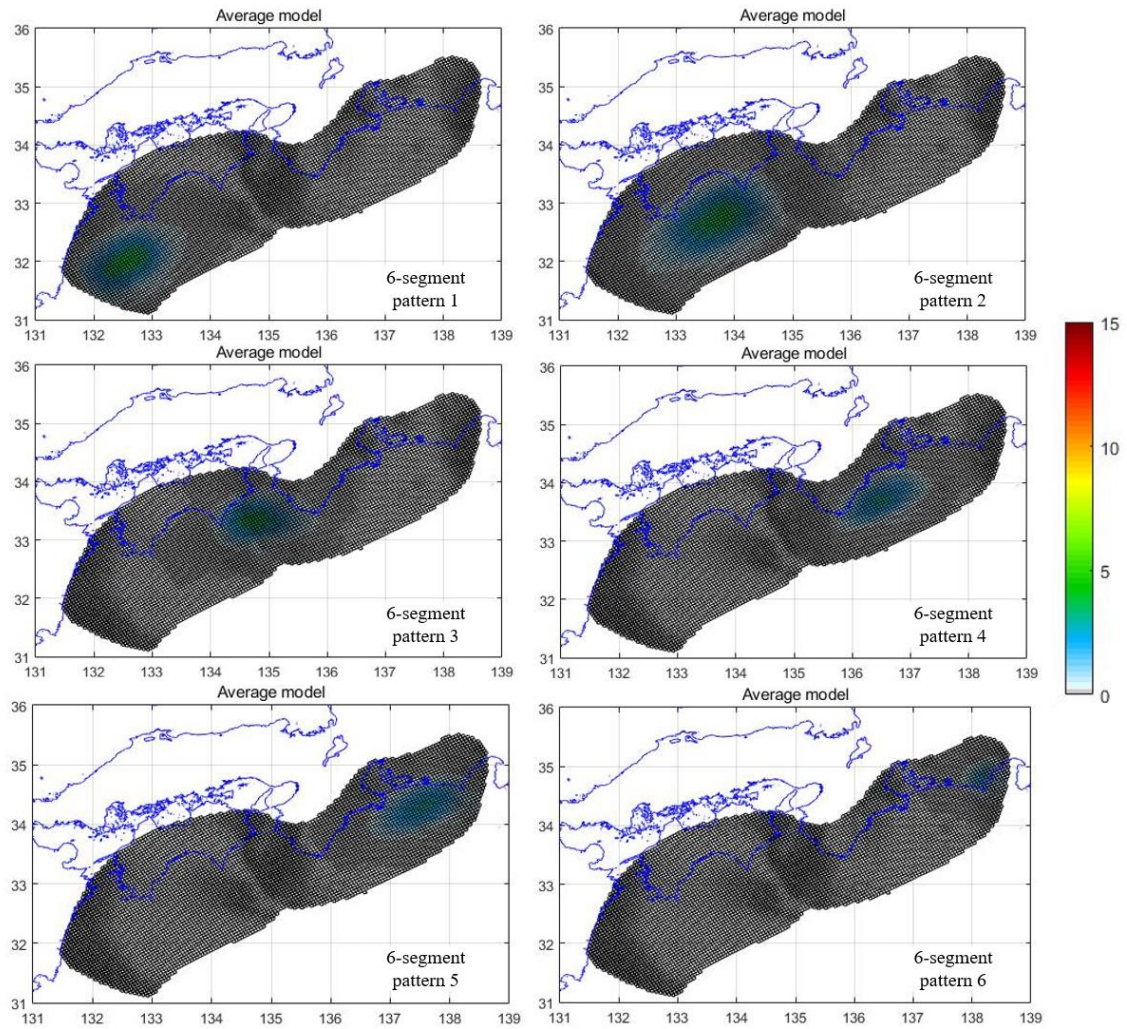


**Figure B1:** Average models of 500 stochastic slip models for the 1) Hyuga segment, 2) Nankai (Tosa) segment, 3) Nankai (Muroto) segment, 4) Tonankai (Kumano) segment, 5) Tonankai (Enshu) segment and 6) Tokai segment rupture patterns in the 6-segment model.

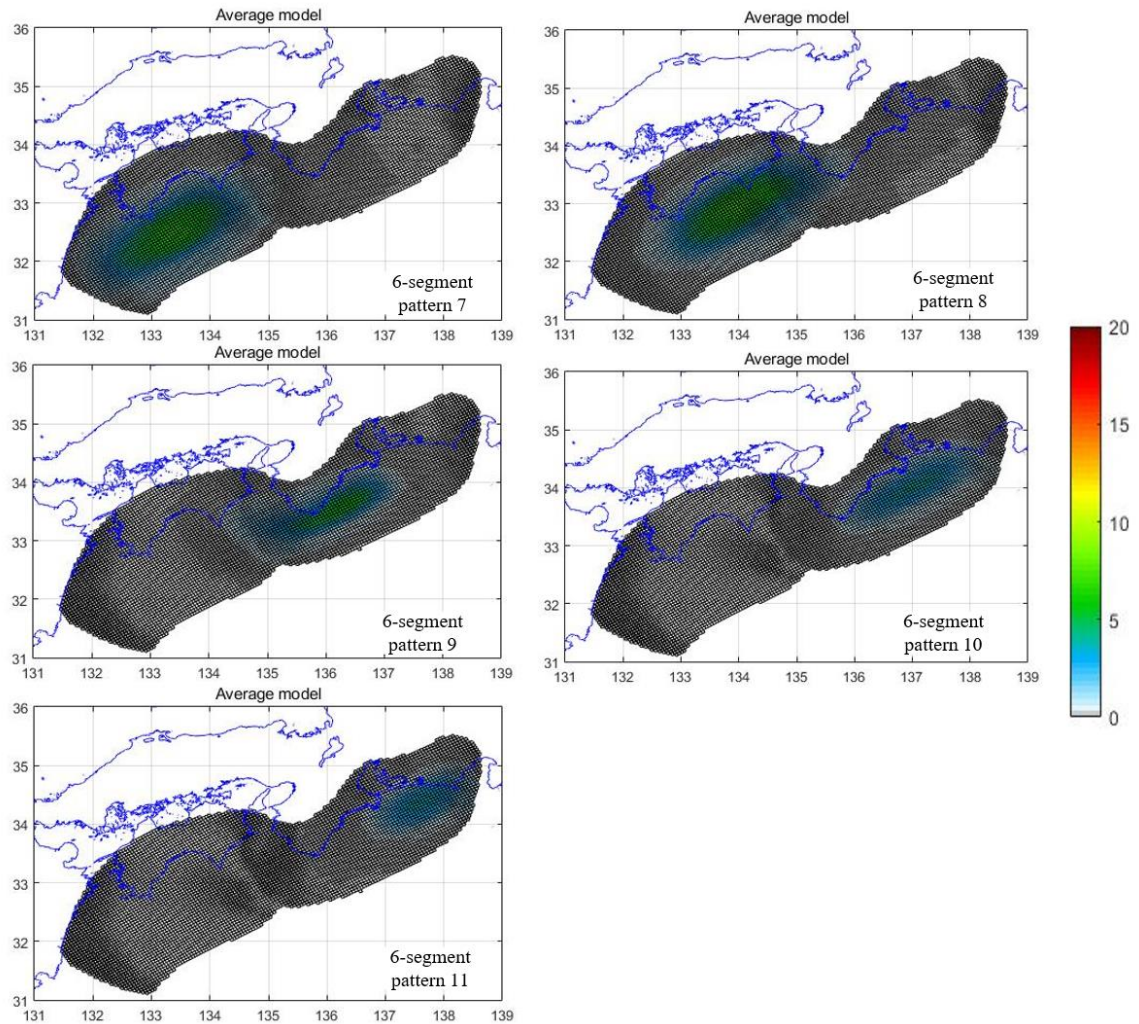


**Figure B2:** Average models of 500 stochastic slip models for the 1) Hyuga - Nankai (Tosa) segments, 2) Nankai (Tosa) - Nankai (Muroto) segments, 3) Nankai (Muroto) - Tonankai (Kumano) segments, 4) Tonankai (Kumano) - Tonankai (Enshu) segments and 5) Tonankai (Enshu) - Tokai segments rupture patterns in the 6-segment model.

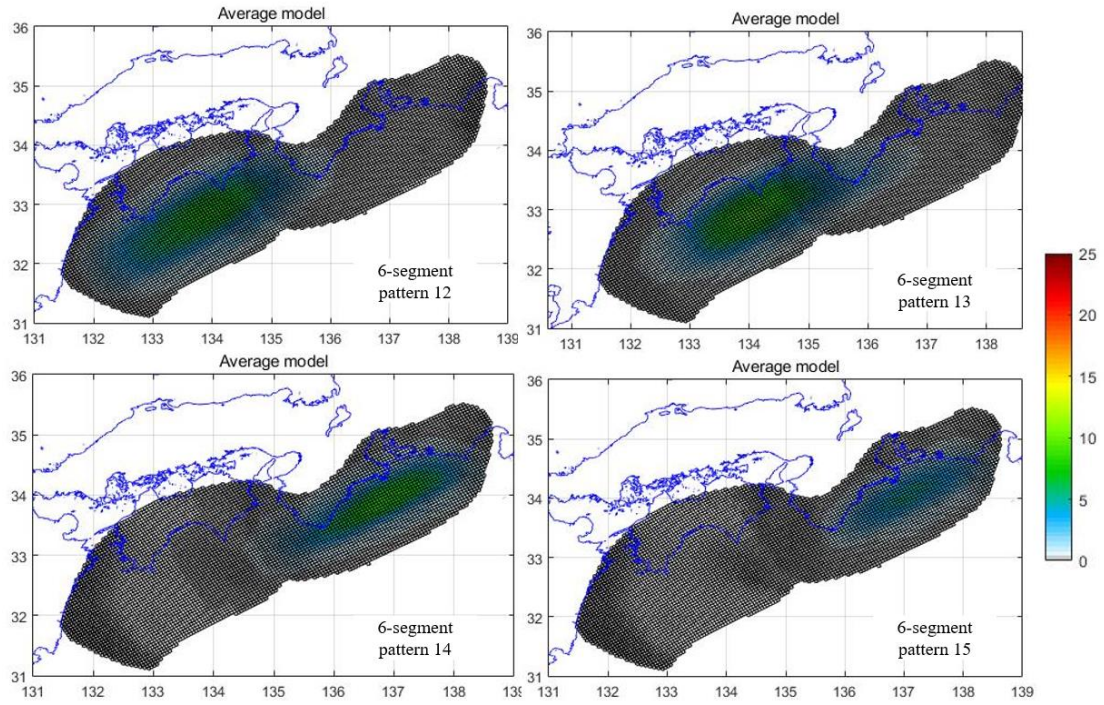


**Figure B3:** Average models of 500 stochastic slip models for the 1) Hyuga - Nankai (Tosa) - Nankai (Muroto) segments, 2) Nankai (Tosa) - Nankai (Muroto) - Tonankai (Kumano) segments, 3) Nankai (Muroto) - Tonankai (Kumano) - Tonankai (Enshu) segments and 4) Tonankai (Kumano) - Tonankai (Enshu) - Tokai segments rupture patterns in the 6-segment model.

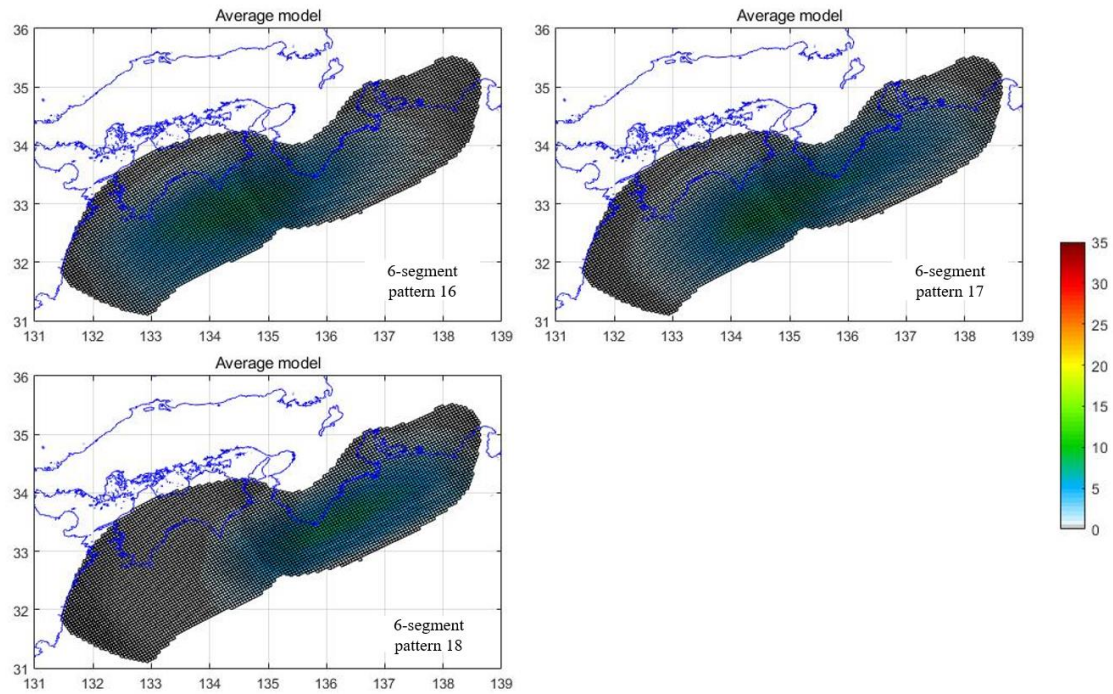


**Figure B4:** Average models of 500 stochastic slip models for the 1) Hyuga - Nankai (Tosa) - Nankai (Muroto) - Tonankai (Kumano) segments, 2) Nankai (Tosa) - Nankai (Muroto) - Tonankai (Kumano) - Tonankai (Enshu) segments and 3) Nankai (Muroto) - Tonankai (Kumano) - Tonankai (Enshu) - Tokai segments rupture patterns in the 6-segment model.

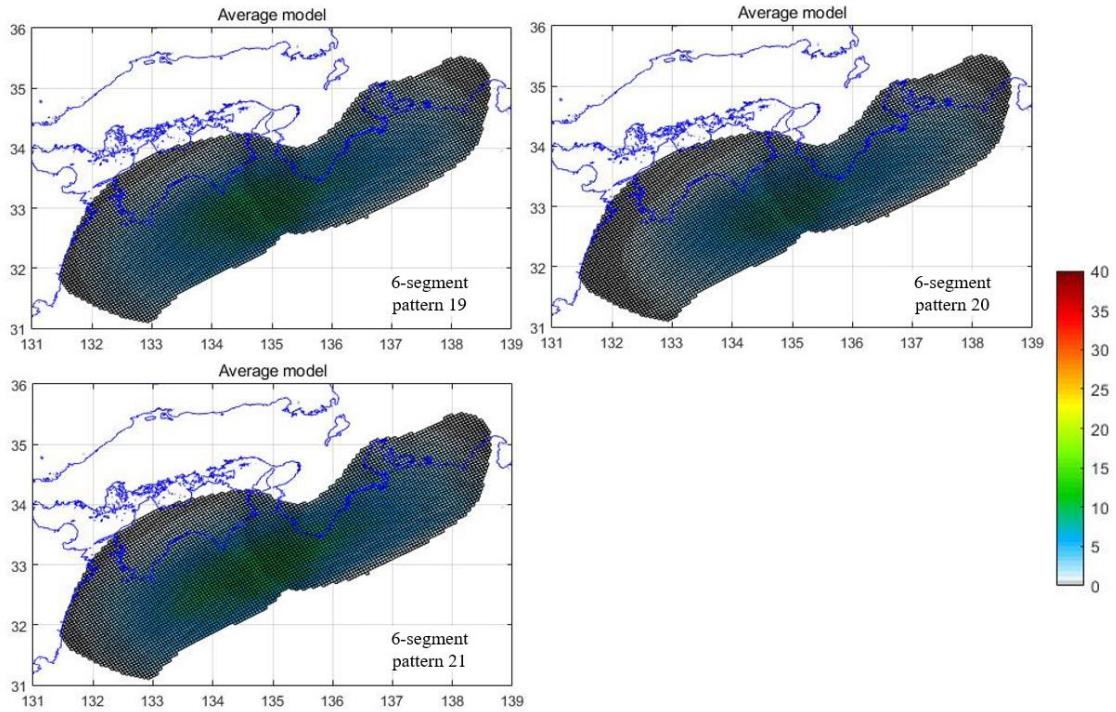


**Figure B5:** Average models of 500 stochastic slip models for the 1) Hyuga - Nankai (Tosa) - Nankai (Muroto) - Tonankai (Kumano) - Tonankai (Enshu) segments, 2) Nankai (Tosa) - Nankai (Muroto) - Tonankai (Kumano) - Tonankai (Enshu) - Tokai segments and 3) whole-region rupture patterns in the 6-segment model.

## Curriculum Vitae

**Name:** Yusong Yang

**Post-secondary Education and Degrees:** University of Alberta  
Edmonton, Alberta, Canada  
2014-2018 B.A.

University of Western Ontario  
London, Ontario, Canada  
2018-2019 M.A.

**Honours and Awards:** University of Alberta Academic Excellence Scholarship  
2014-2015

University of Alberta The JA Jacobs Scholarship in Geophysics  
2018

**Related Work Experience** Teaching Assistant  
The University of Western Ontario  
2019-2021